Analysis of Catenary Shaped Timber Structures

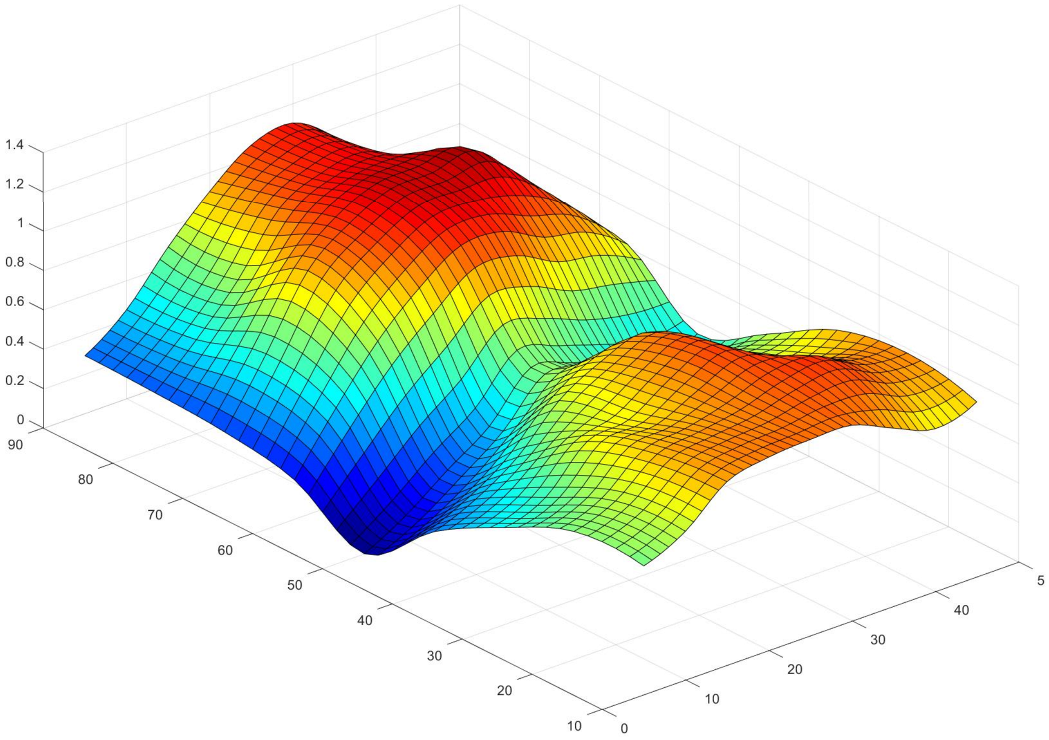

Kristoffer Persson

Division of Structural Engineering
Faculty of Engineering, LTH
Lund University, 2017

LUNDS UNIVERSITET

Avdelningen för Konstruktionsteknik
Lunds Tekniska Högskola
221 00 LUND

Department of Structural Engineering
Faculty of Engineering LTH
Box 118
S-221 00 LUND
Sweden

Analysis of catenary timber structures

Analys av hängkonstruktioner i trä

Master's thesis by
Kristoffer Persson
2017

supervised by

Roberto Crocetti
Professor at Division of Structural Engineering
Lund University

Christoffer Norberg
Professor at Department of Energy Sciences
Lund University

Rapport TVBK-5262
ISSN 0349-4969
ISRN: LUTVDG/TVBK-17/5262+(pp129)

Acknowledgements

This master thesis work was carried out at the Faculty of Engineering LTH for the Division of Structural Engineering.

The original idea for this project was developed by professor Roberto Crocetti to demonstrate the potential in tensile timber structures. This thesis is also a continuation of Samuel Hofvergbergs master thesis *Long-span tensile timber roof structures* that clearly shows the material efficiency of this stress ribbon concept. To further investigate the concept it was decided to study the effect of wind as this was seen as a potential problem area for the design.

Firstly I would like to thank Roberto Crocetti at the division of Structural Engineering, who was my supervisor during this master thesis. He have come with many ideas that have taken the project forward.

I would also like to thank Christoffer Norberg at the Division of Energy Sciences who with his expertise in aerodynamics was a great help in developing the method used in the laboration.

Finally I would like to thank David Gustavsson and Martin Ingvarsson who also have investigated the concept of a timber stress ribbon structure but from a different viewpoint. This provided possibilities for some collaboration and comparison that have further improved the this thesis work.

Abstract

In the design of a building there are many parameters that effect the material efficiency. The choice of structural solution and material are two of the parameters that will be investigated further in this rapport. Suspension structures is one type of structural solution that has high material efficiency, here the bending stiff properties of timber could also be utilized in order to increase the stiffness of the structure. The use of suspension principle on roof structures is however not frequently used as it can give rise to unfavourable load cases which of course causes increased uncertainties. Some reference building has in spite of this been identified and increased understanding about how suspension structures in timber could function and what possible weaknesses this type of structure can have.

With some ideas of how a suspension structure in timber could be designed, different load cases were studied, especially those that were expected to be important for design. Here the uneven snow load, wind uplift and dynamic instability from wind can be highlighted as potential problem areas. In order to get a better understanding of the snow drift on a suspension roof, a scale experiment was performed that showed that most of the snow drift is produced with wind oncoming perpendicular to the roofs parabolic shape and in proximity to the separation zones. The test also showed that a double-sided roof slope resulted in a less unfavourable snow load and that approximating the snow load with an butterfly roofs can give an approximation on the unsafe side.

When the loads on the structure were determined, three different factors that affected the load carrying cross section was evaluated. Firstly the support stiffness was studied, here a lower support stiffness meant bigger displacements and bending moments, while its impact on the normal force were negligible. Secondly the member shape was investigated, the conclusion from this test was that a small catenary shape corresponded to an increase in normal force but at the same time resulted in less deflection, bending moment and increased eigenfrequency. Here the result was calculated with both computer aided FE analysis and analytical expressions. A comparison between the result of FE- and analytical calculations, showed a good agreement for calculations of normal force, while the displacement and bending moment showed larger differences between the different calculation methods. Thirdly the effect of slenderness for the cross-section was examined. In this test a slender cross-section means a high bending stiffness which resulted in that a bigger part of the load was resisted through bending.

Finally a preliminary design on the catenary "timber-cable" was performed, where the information from the investigations could be applied. Biggest difference compared with the reference building was a reduction of catenary shape, which decreased the deformations and made it possible to utilize both the normal force- and bending moment capacity efficiently. The designed building take advantage of a green roof in order to counteract the large suction forces that can occur for this roof shape. In this way, the green roof result in a more slender load carrying cross-section in combination with having several other benefits. With a span of 70 m the final cross-section was designed with a glulam beam with the dimensions of 250 x 300 mm, with a center to center distance of 800 mm. In the load carrying structure two layers of plywood was also used which mostly contribute to the stability of the building. To be able to compare the the material efficiency of the timbercables, the height of the load carrying elements instead would have used a a truss design. With a truss design the hight of the load carrying element would require several meters which clearly shows the advantage of timber cable concept.

Sammanfattning

När en byggnad projekteras så är det många parametrar som påverkar materialets effektivitet. Valet av konstruktionslösning och material är två av parametrarna som kommer undersökas vidare i denna rapport. Hängkonstruktioner är en typ av konstruktionslösning som har hög material effektivitet, här kan förutom träets högra draghållfasthet även träets böjstyvhet utnyttjas för att öka styvheten i konstruktionen. Användandet av hängtak är däremot inte lika vanligt eftersom det kan leda till ofördelaktiga laster och är dessutom inte en historiskt testad lösning, vilket ger upphov till större osäkerheter. Några referensbyggnader har dock kunnat identifierades vilket gav förståelse över hur en hängtakskonstruktion i trä kan fungera och vilka svagheter denna typ av konstruktion kan ha.

Med ideer om hur en hängkonstruktion i trä kan utformas så utredds det vilka sorters laster som kan förväntas vara dimensionerande, där ojämn snölast, vindupplyft och dynamisk instabilitet från vind kan lyftas fram som potentiella problemområden. För att få en bättre förståelse över snödriften på ett hängtak, genomfördes ett skalförsök som visade att de största rörelserna erhålls när vinden inkommer vinkelrätt mot takets parabelform och i närheten av avskiljningszoner. Försöket visade också att en dubbelsidig taklutning resulterade i en mindre ofördelaktig snödrift och att snödrift enligt motfallstak kan ge en approximation på den osäkra sidan.

När lasterna på byggnaden var bestämda, undersöktes tre olika faktorer som påverkade det lastbärande tvärsnittet. Först så utredds vilken påverkan styvheten i upplagen hade för kraftfördelningen. Test med varierade styvhet i upplagen visade att en lägre styvhet gav större förskjutningar och böjmoment, medan påverkan på normalkraften var försumbar. I andra undersökningen testades formens betydelse, slutsatserna från detta försök är att en liten hängform motsvarade en ökad normalkraft men samtidigt minskad förskjutning, böjmoment och ökad egenfrekvens. Här beräknades resultatet både med datorbaserad FE modelering och med hjälp av analytiska uttryck. Denna jämförelse mellan FE- och analytiska beräkningar visade god överensstämmels vid beräkning av normalkraften medan förskjutningarna och böjmomenten visade större skillnader. I tredje utredningen undersöktes påverkan av tvärsnittets slankhet. I detta testet betydde ett slankt tvärsnitt en hög böjstyvhet vilket resulterade i större böjmoment vilket resulterade i att en större del av lasten hölls emot med böjning.

Sist gjordes en preliminär dimensionering av den hängande "trä-kablen", där information ifrån utredningarna kunde tillämpas. Största förändringen som gjordes i jämförelse med referensbyggnaden var en minskning av hängformen, vilket minskade deformationerna och möjliggjorde så att både normalkrafts- och böjmomentskapaciteten kunde utnyttjas mer effektivt. Den designade byggnaden använder sig också av grönt tak vilket tillför tyngd till taket och kan därför effektivt motverka den stora lyftkraften som kan uppstå på denna takform. Det gröna taket gav utöver fördelen att ge ett slankare lastbärande tvärsnitt även en fördröjning av vattenavrinning. Med ett span på 70 m resulterade dimensioneringen av det bärande limträbalken på 250 x 300 mm, med ett cc avstånd på 800 mm. Utöver limträ balkar användes även två lager plywood vilket främst bidrog till byggnadens stabilitet. För att kunna jämföra material effektiviteten av att använda träkablar kan den höjden på det last bärande elementen istället skulle designats som fackverk. Med en fackver design hade de bärande elementen krävt en höjd på flera meter vilket tydligen visar fördelen med träkabel konceptet.

Contents

Notation

Upper-case letters

A	Cross section area [m^2]
I	Second moment of inertia [m^4]
E	Modulus of elasticity [Pa]
E_d	Design value of modulus of elasticity
E_{mean}	Mean value of modulus of elasticity
$E_{mean,fin}$	Final mean value of modulus of elasticity
C_p	Pressure coefficient [-]
V	Wind velocity [m/s]
H	Horizontal force [N]
Re	Reynolds number [-]
St	Strouhals number [-]
D	Characteristic dimension for cross section [m]

Lower-case letters

k	Spring stiffness [kN/m]
m	Mass of object [kg]
E_g	Self weight per unit length [kN/m]
q	Live load per unit length [kN/m]
f	Distance between a horizontal line and a catenary curve (sag) [m]

l	Horizontal span length [m]
P_s	Static pressure [Pa]
n_s	Vortex-shedding induced frequency [Hz]
k_{def}	Factor for evaluation of creep [-]
h	heigh of cross-section [m]
w	width of cross-section [m]

Greek letters

f_n	natural frequency [Hz]
ρ	Density [kg/m^3]
μ	Friction coefficient [-]
ν	Dynamic viscocity of fluid [m^3/kg]

Abbreviations

CEN	European Committee for Standardization
CCE	Canadian Consulting Engineer
AWC	American Wood Council
Glulam	Glued laminated timber
SLS	Serviceability limit state
ULS	Ultimate limit state
T	Tension
C	Compression
FE	Finite element
CU	Capacity utilization
SR	Stress ribbon

Chapter 1

Introduction

1.1 Background

Cable structures like suspension bridges, cable roofs and stress ribbon bridges have typically been built in steel and concrete.The reason behind this is that there is a strong tradition for this reliable materials and for there specific properties. Concrete has for ex. the advantage of being weather resistant but at the same time being sensitive to tensile forces. Steel can however resist large tensile forces which a cable design try to utilize. Steel cables can actually only carry in tension which mean that if a load changes, the cable system changes it shape in order to yet again resist the load in pure tension. For a uniformly distributed load, a parabolic shaped structure will result pure tension which lead to a high utilization of the material. An efficient utilization of the material is increasingly important for structures with growing spans as self-weight (uniformly distributed load) contributes to a greater proportion of the total load. This explains why the world's longest spanning structures are suspension bridges that use this principle with parabolic shaped cables. The problems with these structures instead lie in that they are optimized for evenly distributed loads and have the drawback that asymmetric loads generally produce large deformations on this type of structure. Bending stiffness in the cable can be one solution in order to limit these deflections.

Timber as a material has interesting properties from a structural point of view and also has inherent bending stiffness. When the ratio between material strength and weight for example is compared in the fiber direction it can be concluded that timber has a greater ratio than both steel and concrete. The drawback with timber lies in its low strength perpendicular to the fiber direction and in the design of tensile connections. This increases the importance for smart structural solutions that can make use of timbers optimal characteristics that the following building concept is aimed for. It is also worth noting that timber is the only commercially available renewable building material that has a drastically reduced environmental impact compared to the traditional materials, steel and concrete. In consideration to this, timber form an alternative that reduces the buildings carbon dioxide emissions, which will become even more important in the future in order to achieve sustainable building.

1.2 Aim

This master thesis aims at improving the structural understanding of the catenary timber concept. To achieve this, different parameters that affect the force distribution in the stress ribbon element will be studied and a preliminary design of a stress ribbon element with a span of 70 m will be presented in order to apply the understanding. The preliminary design can also show the possibility of the stress ribbon concept.

1.3 Limitations

The analysis will primary investigate the statical equilibrium of the stress ribbon element even if there will be some discussion on the dynamic stability as well. To simplify the problem and try to get a general understandings of this type of structure, only a 2D case of the stress ribbon elements and its support conditions have been considered.

1.4 Statement of problems

In order to get a better understanding of the stress ribbon element, the following research questions were stated:

- What loads can be expected for this type of structure and in what respect do they impact the deign?
- What types of wind induced instabilities are possible and how does this compare to similar structures?
- How do support stiffness, the sag of the structure and slenderness of cross-section affect the force distribution?
- How large must the load carrying cross-section be in order to have a span of 70 m ?

Chapter 2

Theory: Internal forces

This chapter will discuss the internal forces that would develop in a catenary timber structure. As this continues from Samuel Hofverbergs master thesis *Long-span tensile timber roof structures* the concept of the structure is shown in fig. 2.1.

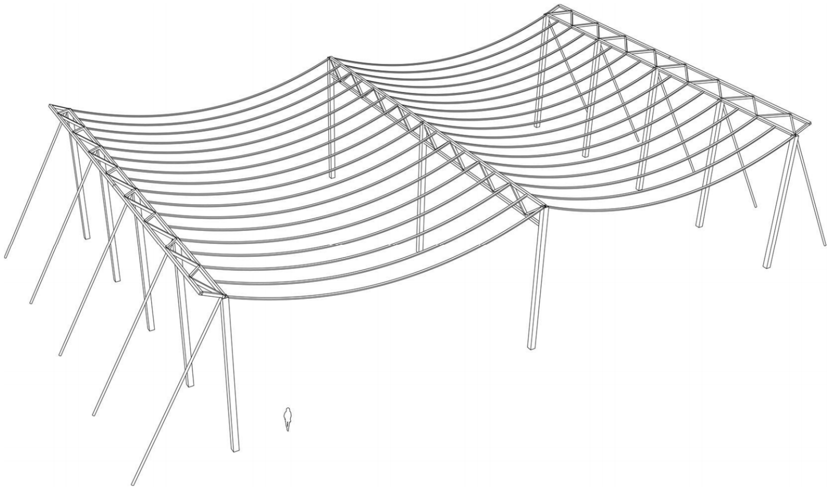

Figure 2.1: Initial structural idea for the catenary roof structure by Samuel Hofverberg
Source: Hofverberg, 2016

With a structural solution shown in fig. 2.1, there are several factors that impact the internal force distribution. Therefore the following factors will be discussed:

- Material efficiency in the structural solution, to demonstrate some of the benefits with this design.
- How structural- and bending stiffness affect the design. This also explain some of the drawbacks with catenary structres and some possible solutions for these drawbacks.
- Timber as a material and a reference building using timber cables.

2.1 Material efficiency of arches and cables

From fig. 2.2 a) it can be seen that the maximum stresses only occur at mid-span section and only in the top and bottom fibres. It is evident that a beam has a significant amount of dead mass and that the element could be further optimized. From the beam a suspension cable or arch can be derived where the horizontal force is taken up at foundations as seen in fig. 2.2 b) and c).

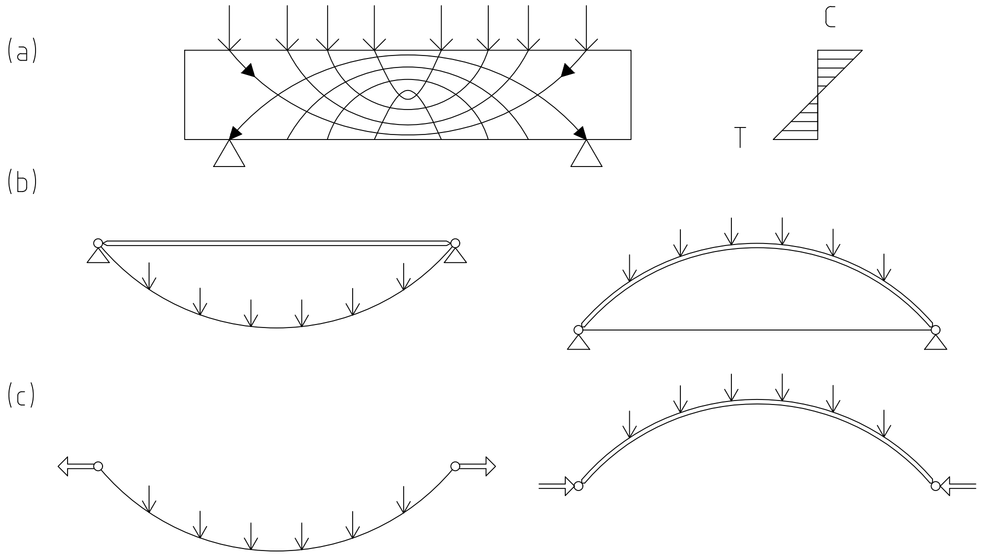

Figure 2.2: Principle force distribution in a beam and the derived arch and cable shape. Note that figure a) shows theoretical compressive- and tensile lines but that all load will eventually be transported to the supports

The arch and the cables efficiency originate from their shape, as a uniformly distributed load on this type of structure would only result in axial forces. Cables have here the advantage to be able to change their shape according to the load which means that similar to a perfect arch it will only be stressed in normal force, but in this case tension. This produces even normal stress over the cross-section which causes equal utilization of all the fibres.

These cable and arch shapes are very efficient for an evenly distributed load, as an example a concrete arch could in theory span several kilometres and a suspension cable could be designed for even longer spans. But in practical cases there will always be some sort of uneven loading as well as demand on economic sag that will restrict the structures shape so that the maximum span becomes well below the above mentioned theoretical limit. With the above mentioned benefits of cable structures it should come to no surprise that the current worlds longest spanning structure is a suspension bridge called Akashi Kaikyo, which have a main span of 1991 m (Chen and Lui, 2005).

2.2 Stiffness for cable supported structures

To define stiffness, lets look at the simple case with a rod with a linear material properties. For this rod the stiffness k can be described with the following equation:

$$k = \frac{AE}{L} \tag{2.1}$$

where

A	Area [m^2]
E	Young's modulus [N/m^2]
L	Rod length [m]

From eq. (2.1), the stiffness k can be seen as a measurement of the rods resistance to deformation and is also the definition that is referred in this chapter.

From the sections above it is evident that the cable can be structural efficient but the change of shape that gives the cable its efficiently can also cause problems with deflection, which occurs when the load is asymmetric. To solve this problem there are three different stiffening method as shown in fig. 2.3 (Strasky, 2005).

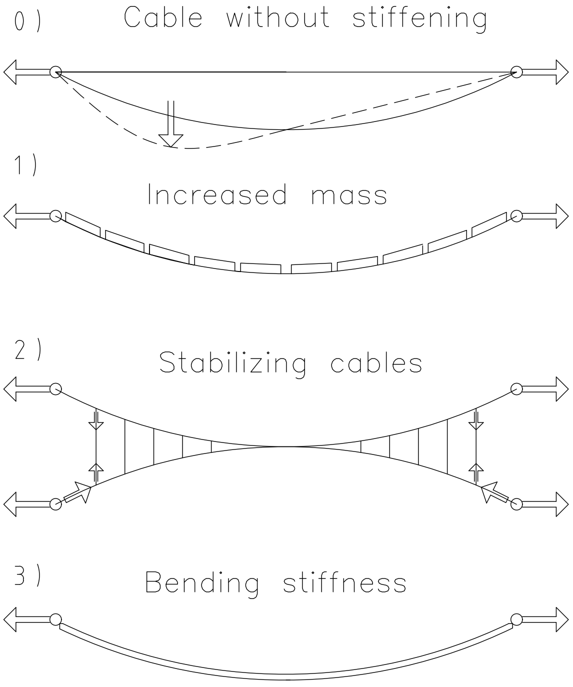

Figure 2.3: Different stiffening principle for cable structures

In both alternative 1) and 2) (fig. 2.3), two different methods of pre-stressing are applied to the main cable which increases the horizontal force and results in a higher stiffness. The third alternative 3) instead uses bending stiffness to increase the structural stiffness in the cable.

The third concept of integrating a degree of bending stiffness in a cable is called stress ribbon and with the use of timber as cable material the cable will naturally inherit some bending stiffness. This is in contrast to using steel cables when concrete is used in order to give the cable its bending stiffness (Strasky, 2005). In this way the timber cable could use the positive properties from the cable behaviour with it's efficient loading, while at the sane time making use of the bending stiffness.

The shape of the stress ribbon follows a catenary curve similar to a cable subjected to an evenly distributed load. Using this principle the stress ribbon elements can be formed after its self-weight and therefore, first develop bending moment after the SR element deform away from the catenary curve. With this assumption the horizontal force for a simply supported stress ribbon element subjected only to it's self-weight can be approximated with the familiar equation eq. (2.2) (Marti, 2013).

$$H = \frac{qL^2}{8f} \tag{2.2}$$

where

H	Horizontal force [N]
q	Evenly distributed load [N/m]
L	Span length [m]
f	Sag at midspan [m]

Parameters from eq. (2.2) are also seen in fig. 2.4

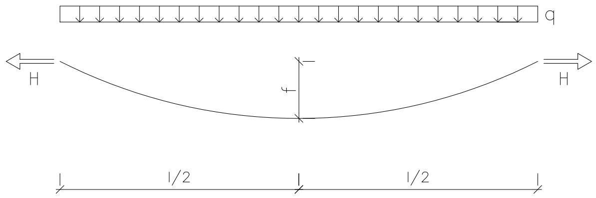

Figure 2.4: Cable subjected to uniformly distributed load

2.3 Parameters impacting the structural frequency

2.3.1 Frequencies induced by wind

The stiffness as mentioned above has also an impact on the buildings natural frequency. In general terms the stiffness and the natural frequency can be seen as connected, as an increase of stiffness generally leads to a higher natural frequency (Mercier et al., 2012). For structural design against wind it is generally good to have a high natural frequency as the main frequency induced by wind on structures is between 0.005-10 Hz as seen in figure fig. 2.5 (Holmes, 2015). But as shown in fig. 2.5 the opposite can be the case for earthquake loads. From the figure it can also be seen that wind instability is generally relevant for tall buildings or long span bridges. This can be explained with that these type of building have lower eigenfrequencies and therefore are more susceptible to resonance caused by wind, compared with low rise buildings.

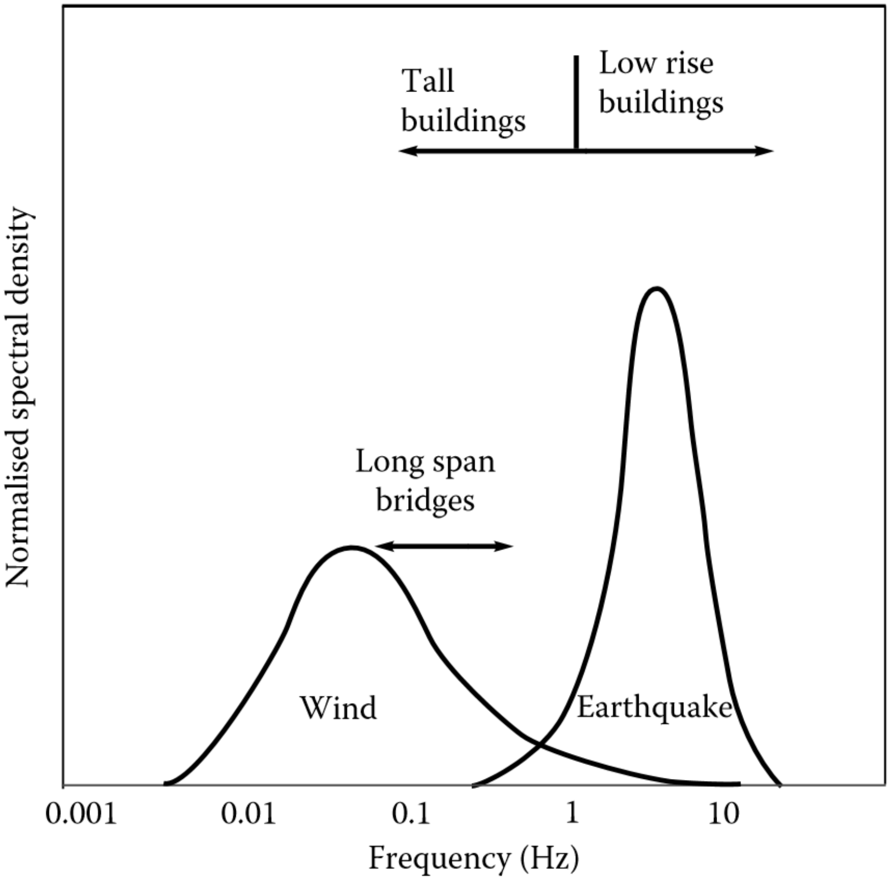

Figure 2.5: Dynamic excitation frequencies of structures by wind and earthquake.
Inspired by: Holmes, 2015

2.3.2 Natural frequency for a simple spring

To get a feeling of the influence of stiffness on the structures natural frequency, let's consider a building vibrating similar to a single spring (often a good approximation, Mercier et al., 2012). If the spring is fixed at one end and has a mass attached at the other end, the response amplitude will oscillate at specific load frequencies. This spring is a a single degree oscillator and can therefore be described by eq. (2.3) (if damping is neglected) (Chopra et al., 1995).

$$f_n = (2\pi)^{-1}\sqrt{\frac{k}{m}} \tag{2.3}$$

where

f_n	natural frequency [Hz]
k	Spring stiffness [N/m]
m	Weight of attached mass [kg]

From eq. (2.3) it is clear that a stiffer spring results in a higher natural frequency. This relation is also true for structures such as buildings and bridges (Holmes, 2015), and shows how alternative 3 in fig. 2.3 increases the natural frequency of the cable.

2.3.3 Natural frequency for a cable

As a comparison to the spring system a similar expression can be derived for a perfectly flexible cable with the mass m uniformly distributed along the horizontal projection, shown in eq. (2.4) (Ghiocel and Lungu, 1972).

$$\omega_n = \frac{n\pi}{l}\sqrt{\frac{H}{m}} \tag{2.4}$$

From eq. (2.4) it is clear that a higher horizontal force also results in a higher fundamental frequency, which is the same principle for stiffening the cable seen in fig. 2.3. If the only force that produces tension H in the cable is assumed to be a dead load, this results in: $m = \frac{q}{g}$ and $H = ql^2/8f$ and eq. (2.4) becomes:

$$\omega_n = n\pi\sqrt{\frac{g}{8f}} \tag{2.5}$$

where g is the dead load [N/m] and the other parameters are explained in eq. (2.2) and eq. (2.3).

From eq. (2.4) it can also be seen that the first stiffening method with increased mass in fig. 2.3 leads to a higher natural frequency. Here a potential problem with the lightness of timber material is evident as the low self-weight leads to a low natural frequency. One alternative to improve this aspect would be to install a green roof that would also have positive effect on stormwater runoff (Soulis et al., 2017).

2.3.4 Natural frequency for reference buildings

To compare the theory of springs and cables to real suspension structures, three reference examples are presented, Nagano Olympic arena, Vranov Lake bridge and Willamette River bridge.

For the Nagano Olympic arena seen in fig. 2.6, a very light roof was used and as the span was 80 m, it was felt necessary to ensure stability for both static and dynamic wind loads. (Suzuki et al., 1997). The load carrying section consist, of a composite member of two curved glulam beams sandwiching a steel plate according to fig. 2.7, with a sag of 5 m.

Figure 2.6: Nagano Olypic arena, showing the visitors experience of a catenary shaped roof
Image source: Maclourin, (2017)

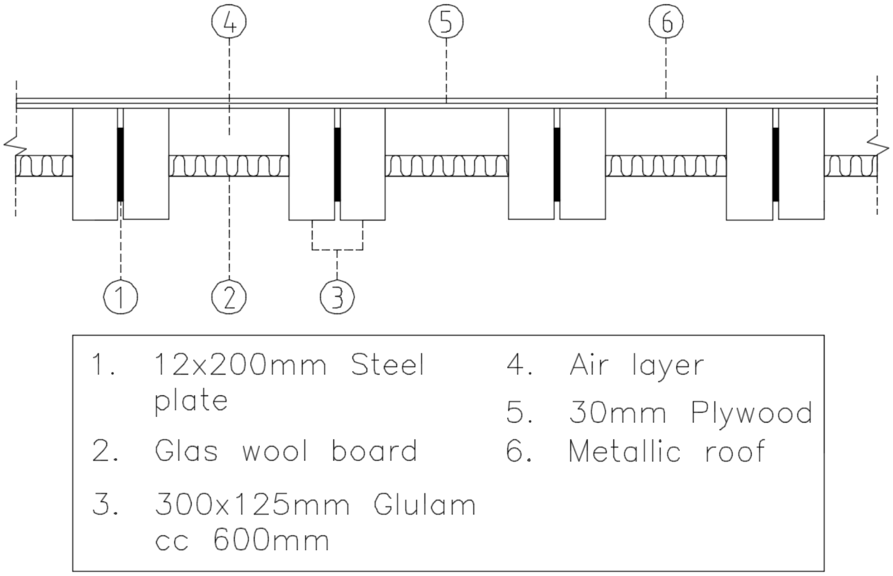

Figure 2.7: Load carrying cross-section for Nagano Olympic arena
Inspired by: Suzuki et al., 1997

The first mode shape of the roof was asymmetric with a frequency of 0.32 Hz (0.65 Hz with structure own dead load) while second mode shape was symmetric with a natural frequency of 0.68 Hz (0.98 with dead load). With the difference in mode shape it was possible to identify that it was primarily the lower asymmetric mode that was excited from the 100-yr-return-period wind velocity. This model was then controlled with both FE simulations and wind tunnel testing and the conclusions were that the roof was stable for both the static- and the dynamic wind loads.

It can also be interesting to compare these eigenfrequencies against pedestrian bridges often designed quite slender, even if the biggest problems for these pedestrian bridges usually are the response from pedestrians (Mercier et al., 2012). For the suspension bridges, Vranov Lake bridge and Willamette River bridge the first and second mode shapes followed the same pattern as Nagano Olympic arena. The first two eigenfrequencies for Vranov Lake bridge were measured to 0.298 and 0.431 Hz while the corresponding frequencies for Willamette River bridge were 0.541 and 0.613 Hz respectively. Similar to Nagano Olympic arena both these bridges were analysed in dynamic- and wind tunnel tests that could ensure their structural stability (Strasky, 2005).

2.4 Impact of sag/length of a cable

The ratio between sag and span for stress ribbon footbridges has a great influence on its structural performance, including horizontal reactions, pre-stressing force, vibration characteristics and serviceability of pedestrians (Han et al., 2016). At low sag-to-span the horizontal forces are increased according to eq. (2.2), this in turn requires more extensive abutments which can make the structure less economical (Kalafatic et al., 2006).

When the sag-to-span increases, the dynamic response for a stress ribbon footbridge tends to get better as the antisymmetric mode becomes the lowest mode and the natural frequency increases and avoids the range of 1.5 Hz to 2.3 Hz which is the design criteria for pedestrian bridges (Han et al., 2016). The high sag to span ratio also decreases the horizontal force making the design possible to be both economically and structurally efficient.

The drawback with increase of sag/span ratio for pedestrian bridges lies in the serviceability for the pedestrians as a high sag/span ratio results in a steeper inclination. As the roof structure doesn't have this restriction more sag can be accepted even if too much sag could result in low horizontal force H. The low H could be problematic as it would give the structure a low natural frequency (according to the cable analogy in eq. (2.4)), as well as bad utilization of the inside space. To determine a suitable sag for the catenary timber roof, different already existing stress-ribbon structures were therefore investigated as shown in table 2.2.

Table 2.1: Investigation of sag to span ratio for different stress ribbon structures

Reference structure	Load carrying material	sag f [m]	span L [m]	sag/span
Grandview Heights Aquatic Center(1)	"timber cables"	6.096	50	0.122
Stuttgart Exhibition Hall(2)	steel cables	6.35	56.5	0.112
Nagano Olympic Arena(3)	steel and timber composite	5	80	0.0625
Brno-Bystrc Bridge(4)	steel cables and concrete	1.2	63	0.019

Sources for information: 1) Gonchar, (2014), 2) Ludescher et al., (2007)
3) Ban et al., (1998), 4) Strasky, (2005)

2.5 Impact of bending stiffness

With bending stiffness its the resistant to bending that is referred, similar to the deninition of stiffness in section 2.2. This resistance can be measured with the second moment of intertia (I) which is also a property that differentiates the stress ribbon system versus a pure cable type response. How bending stiffness effects the force distribution in a stress ribbon (SR) structure has been studied by (Strasky, 2005) and can be visualised according to fig. 2.9.

In Straskys study a SR cable with varying bending stiffness was loaded with an asymmetric- and temperature load respectively. In fig. 2.8a, a live load of $q = 20$ kN/m was placed on left half of the span, while in fig. 2.8b a temperature load of $\Delta T = -20°C$ (equivalent to dead load), was placed uniformly over the span. In both the load cases the stress ribbons self-weight was also added as this load will always be present. The starting cross-section for the SR cable was a concrete band with a width of 5 m a depth of 0.25 m and a modulus of elasticity of $E_c = 36$ GPa. These conditions result in a second modulus of inertia of: $I_c = \frac{1}{12}bh^3 = \frac{1}{12}5.00 \cdot 0.25^3 = 0.00651\,m^4$. The cross section area was then kept constant while the bending stiffness was increased according to:

$$\begin{aligned}
I_c(1) &= 6.51 \cdot 10^{-3}\,m^4 & I_c(6) &= 1\,m^4 \\
I_c(2) &= 1 \cdot 10^{-2}\,m^4 & I_c(7) &= 5\,m^4 \\
I_c(3) &= 5 \cdot 10^{-2}\,m^4 & I_c(8) &= 1 \cdot 10^{1}\,m^4 \\
I_c(4) &= 1 \cdot 10^{-1}\,m^4 & I_c(9) &= 5 \cdot 10^{1}\,m^4 \\
I_c(5) &= 5 \cdot 10^{-1}\,m^4 & I_c(10) &= 1 \cdot 10^{2}\,m^4
\end{aligned}$$

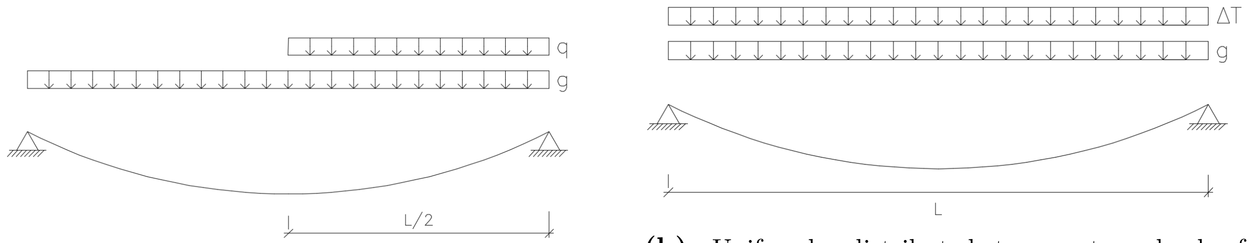

(a) Live load q=20kN/m on right part of the span

(b) Uniformly distributed temperature load of ΔT=-20C°

Figure 2.8: Load cases in the study of bending stiffness influence

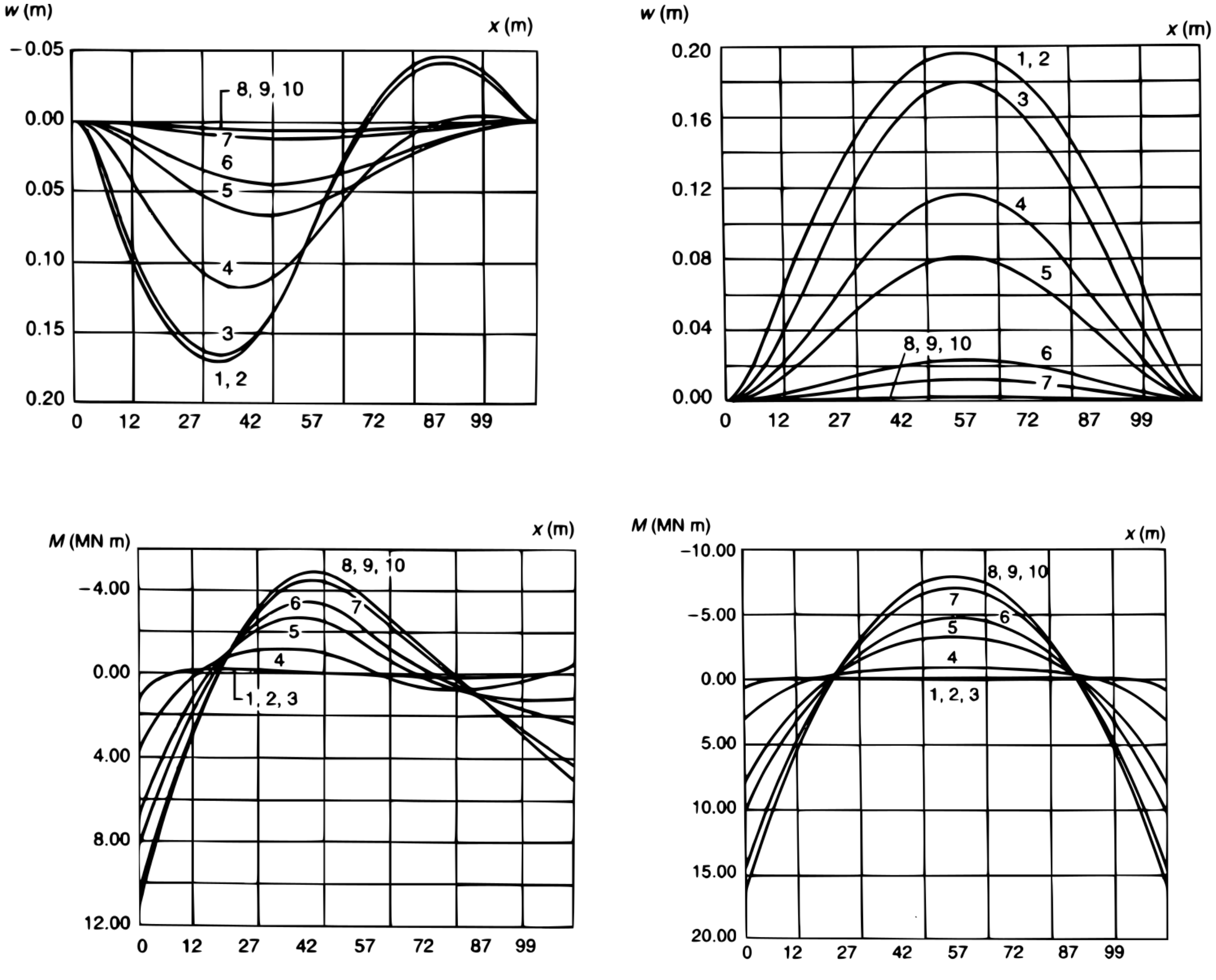

Figure 2.9: Plots displaying the influence of bending stiffness on deformation- and moment distribution. Left plotts show the SR structure loaded asymmetrical according to fig. 2.8a, while right plots show the SR structure loaded symmetrical accoding to fig. 2.8b
Inspired from: Strasky, 2005

From fig. 2.9 it can be seen that the deformation (w) and bending moment (M) depend on the stiffness of the concrete slab. A interesting observation is that with low bending stiffness ($I_c(1) - I_c(3)$), the deformation and moment is nearly the same as for a pure cable. In this range the cable resists the load in tension with negligible bending. It can also be seen that the positive effect of increased bending stiffness is a decreased deflection while this at the same time results in a higher bending moment. Therefore it is important to find the balance between having a high enough I to have a reasonable deflection in the SLS state while at the same time having a low enough I in order to not obtain large bending moments.

2.6 Impact of the order of theory

Using analytical calculation simultaneous as FE calculation can be good way to achieve a realistic FE model (Crocetti, 2016a). As the FE calculations easily can use higher order of theory compared with hand calculations, it can be interesting to understand the differences between the different theories (Runesson et al., 1992).

2.6.1 First order theory

In first order theory it is assumed that the structural element and the material are linear elastic and that the deformations are small. The original geometry can be used to form the equilibrium equations. It is also assumed that the deflection and section forces are directly proportional causing the superposition principle to be valid, where the effect of different types of loads can be calculated separately and summarised to form a result.

2.6.2 Second order theory

For some structures considerable deflections can arise in which it is not longer sufficient to calculate from the structures original geometry. A typical example of this are frames or suspended roofs, see fig. 2.10, which are exposed to large vertical forces in combination with horizontal forces. This load case causes horizontal deflections which in turn lead to eccentricity for the vertical forces. If the deflections for the structure are still small but are considered in the formulation of the equilibrium equations, the calculations are of second order. The relation between load and deflections are in this theory no longer linear even if a linear elastic material is assumed. The superposition principle is no longer true.

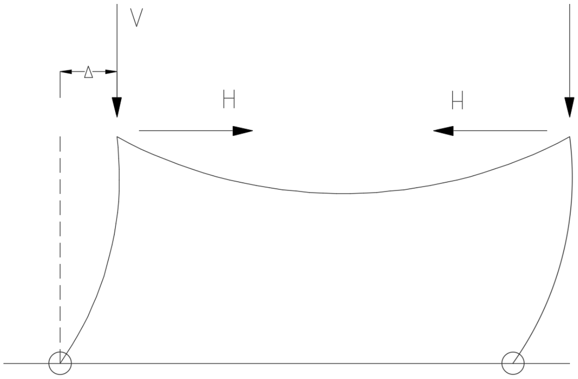

Figure 2.10: Initial horizontal deflection from horizontal forces that is taken in consideration when calculating according to second order theory

2.6.3 Third order theory

If the deformation can not be considered small and the real geometry is used to form the equilibrium equations, then the calculations are considered to be of third order. This causes the relationship between load and displacements to be non-linear and with the same reason as for the second order theory the superposition principle is therefore not valid in this theory either.

2.7 Material efficiency of timber

In this context the material efficiency is referred to the ratio between the capacity divided by the mass of the load bearing element. This was studied by Crocetti, 2016c, this investigation uses a cross-section with area A and length L. This element was then studied for compression, tension and bending with the purpose of maximizing its structural efficiency and was later compared between different material, as seen in table 2.2.

Table 2.2: A comparison of some structural materials' abilities to resist tension, buckling and bending. The higher the the given ratio, the more efficient the material can be considered (Crocetti, 2016c).

Material	Strength f [MPa]	Density ρ [kg/m^3]	Young's modul E [GPa]	Tension/compression effciency ratio$^{(1)}$ f/ρ	Bending efficiency ratio $f^{(2),(3)}/\rho$	Deflection and buckling efficiency ratio $\sqrt{E}/\rho$
Softwood	20 - 30	350 - 450	11 - 13	44 - 85	16-28	7 - 10
Carbon steel	235 - 355	7800	210	30 - 45	5 - 7	2
Concrete	30 - 50	2500	30	1 - 2$^{(2)}$	-	2
CRFP (carbon fibers)	500 - 1400	1600	70 - 300	300 - 900$^{(3)}$	39 - 78	5 - 11

(1) In case of compression, the values are usable only for members restrained against buckling
(2) Applies only for members in compression
(3) Applies only for members in tension

From table 2.2 it is possible to see that the material efficiency ratio is higher for timeber and CRFP, compared to both steel and concrete. This shows the benifits of having a low material density coupled a high capacity which enable that more of the material can be used to carry load instead of carrying its own self-weight.

2.8 Properties of timber and glulam

2.8.1 Manufacturing of Glulam

The raw material for glulam is strength graded timber bords, typically spruce. The timber is then glued together under strict conditions, with high pressure and controlled moisture levels which result in a reduced risk for cracking and twisting (Johansson and Lidelöw, 2015, chap 2). This manufacturing gives good flexibility on both shape and element size as the size is determined by varying the number and width of glued timber boards while the shape can be altered during the hardening of glue.

2.8.2 Capacity of glulam and sawn timber

As the raw material for glulam is timber the material strength compared with regular sawn timber is the same for small knot-free samples. But as glulam beams are built up by smaller elements of sawn timber the probability for a big weakness in a specific section decreases. This in turn results in a less variable material strength and as the lower 5% percentile is used in design, this means that the capacity in glulam is higher than in the sawn timber (ibid., chap 2).

2.8.3 Influence of grain direction

An important property of wood is the grain direction, which has a big impact on the woods mechanical characteristics. To get a rough understanding of wood, the fibres can be thought of as a bundle of tubes. With this analogy it is easy to understand that the axial strength is greater than in the perpendicular direction. The difference is especially distinct in tension, where the material strength for tension parallel to the grain direction is of the order $f_t \approx 100$ MPa compared with a strength of $f_{t,90} \approx 0.5$ MPa for tension perpendicular to the grain direction (ibid., chap 2). For compression the corresponding strength is $f_c \approx 80$ MPa and $f_{c,90} \approx 3 - 5$ MPa respectively.

2.8.4 Brittle failure and possible connections

Timber as a material can be seen as having a brittle failure which means that only small elongation of the material will develop before failure. Here a more ductile failure is preferred as large deformation before failure, enable safe evacuation. A material can of course be more or less brittle, for timber a tensile failure exhibits a very brittle failure while compression failure is still brittle but has a more plastic behaviour. Timber having a brittle failure is of course not a desirable trait of wood which is in combination with practicalities, the reason why wood connections are typically designed with ductile steel parts (ibid., chap 4). An alternative to this is a finger joint that can be manufactured with higher capacity then the rest of the cross-section and therefore enables minimum use of steel which also has both economic and environmental benefits.

2.9 Reference timber building

Similar to the natural frequency it could be useful to look at reference buildings to benefit from already made studies. Since Grandview Heights Aquatic Centre shares many similarities with the proposed stress ribbon concept in both structural solution and material use, a little deeper analysis for this building was made.

Grandview Heights Aquatic Centre is an indoor swimming hall in the south west part of Canada, more precisely in the city of Surrey. The roof has a primary load carrying structure of timber catenary glulam beams and has a maximum span of 55 m with a 300 mm deep structure, see fig. 2.11 (CCE, 2016). This makes it the longest spanning timber catenary roof built to date and its slenderness can be compared to a 3000 mm high steel truss that would otherwise have been required. The shape of the building is also utilized well as the diving tower is placed at maximum roof height while the roof height over the swimming pools is lower. This at the same time as reducing the buildings internal volume and ensuring long term energy cost savings.

The original idea for this building was to use steel cables with wooden cladding for aesthetic reasons. From this engineers realized that "timber cables" could be used to carry the load instead. The load bearing structure consists of two 5" x 10.5" (127 x 267 mm) glulam beams with a center to center distance of 30 inch (762 mm) (Gonchar, 2014). These beams act like cables under a double layer of plywood as shown in fig. 2.13. In order to limit the length, the glulam beams were split into two or three parts (depending on span length) with a connection as shown in fig. 2.12. This resulted in a longest glulam beam of 22 m which made it was possible to transport the glulam beams to the building site, enabling manufacturing under controlled conditions in a factory.

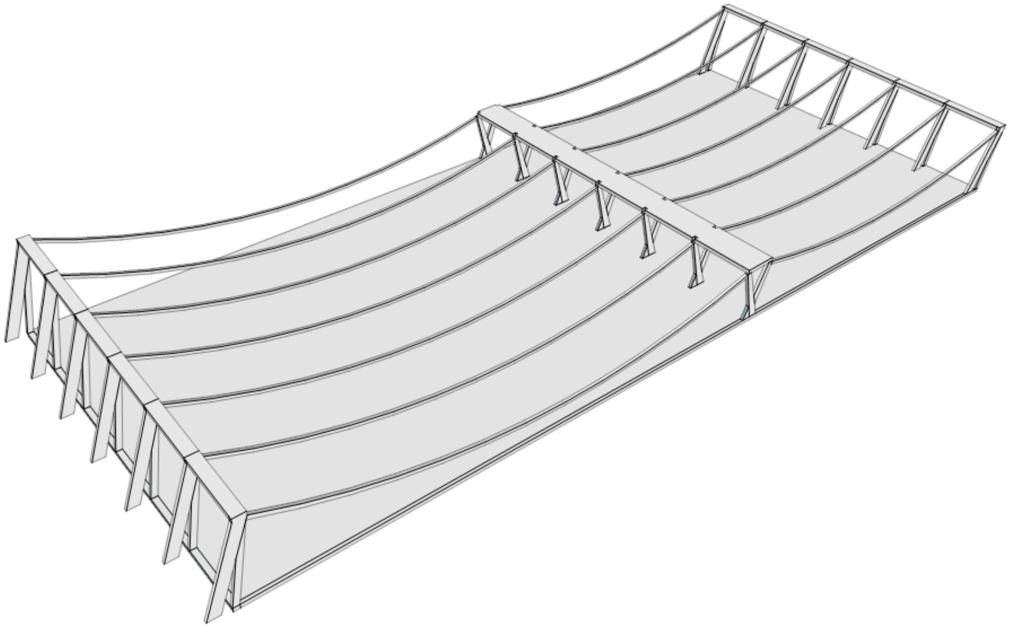

Figure 2.11: Overview of the structural details in Grandview Heights Aquatic Centre

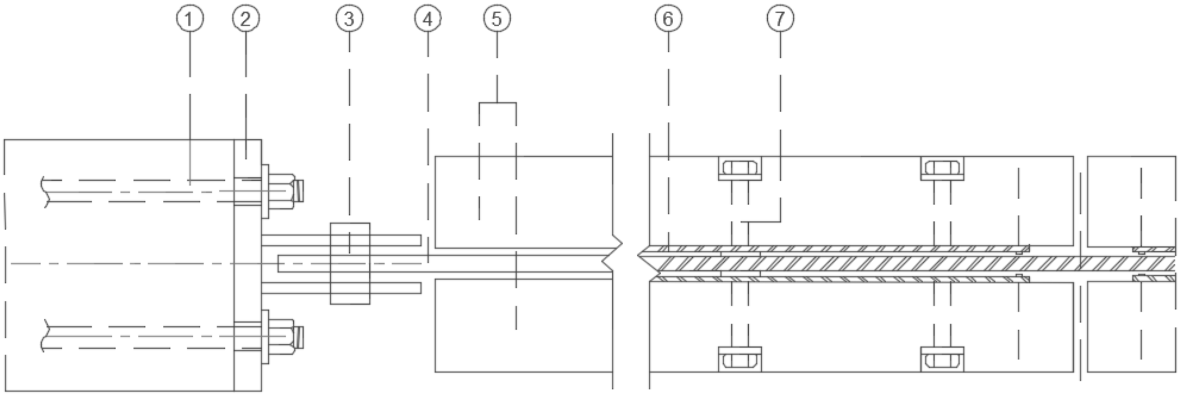

1. D 29 mm x 1500 mm steel rod anchored into concrete slab and 25 mm nonshrink grout (not shown)
2. 38 mm steel plate
3. D57 mm pin and 16 mm plate
4. 22 mm x 200 mm steel plate
5. 5" x 10" deep Douglas fir glulam
6. 220 mm x 800 mm nailing plate
7. D25 mm ASTM A325 bolts, hot-dopped galvanized (220 mm o.c.) with wood plugs

Figure 2.12: Connection details for Grandview Heights Aquatic Centre
Inspired by: Schuler, 2017

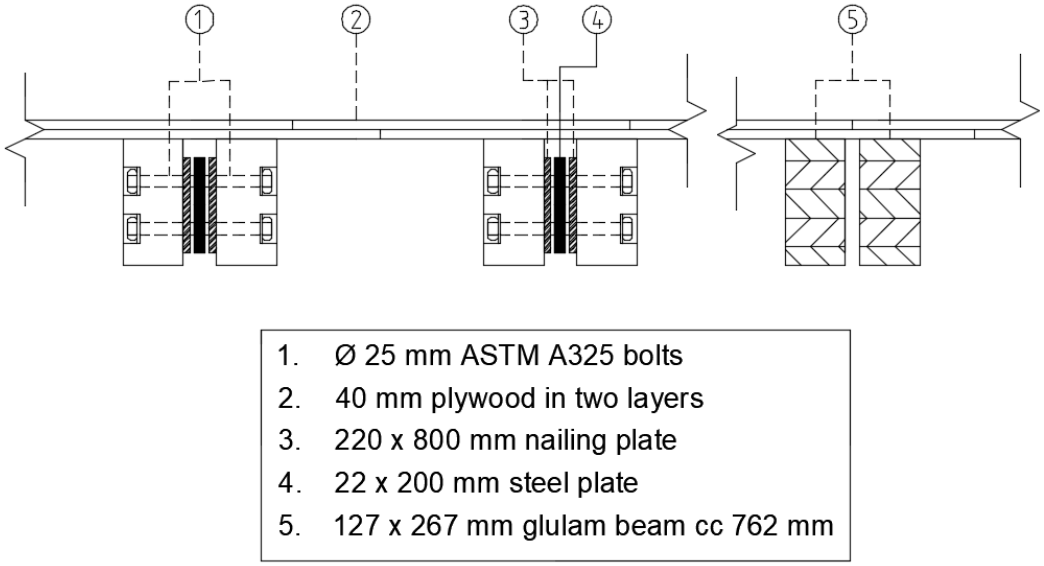

Figure 2.13: Cross-section of the load carrying section in Grandview Heights Aquatic Centre

According to (CCE, 2016), in this project there were three key technical difficulties that have the following solutions:

1) Unbalanced snow loading. Early analysis of unbalanced snow loading for cable spanning 105 m showed a vertical deflection in the order of 1000 mm. To solve this an intermediate support was added as well as central structure with a shear wall in one end and steel brace at the other end. With this changes engineers effectively reduced the maximum deflection to acceptable 250 mm.

2) Wind uplift forces. One of the drawbacks of using timber is its low self-weight to counteract wind uplifting forces. The usual solution for this problem is adding a thin concrete layer on the roof but as this was thought of as being counterproductive to the buildings environmental impression, as well as costly, this idea was not used. Another standard solution is to install stabilizing cables inside the building, but this would at the same time ruin the aesthetic impression. Instead the timber members were designed to act as an upside down compression arch against the upwards acting wind suction. Here the two layers of plywood also plays a part in stabilization by preventing buckling.

3) Dynamic excitation. With a very slender load carrying structure there will be risk for dynamic excitation from wind as discussed in section 3.1. The engineers felt that the roofs warped geometry in combination with high damping from glued roof insulation, would be sufficient to prevent resonance oscillation. This hypotheses was later confirmed with field test using accelerometers, metronome and dynamic load from a "jumping party".

With a cost of 55 million $ and an area of 8825 m^2 Grandview heights aquatic centre serves as a good example were "thinking outside the box" results in a more sustainable design with minimal material use, without substantially increasing building costs (CCE, 2016). This also lead to an increased public interest with the anticipated number of visitors surpassed as well as receiving two Canadian engineering awards with the motivation of being cost-effective, structurally-efficient and aesthetically-pleasing.

Chapter 3

Theory: External loads

With a brief understanding of factors that affect the internal force distribution, the next step was to study the possible external loads on this type of structure. Some of the loads that will be discussed is the following:

- Wind flow over the building to understand where the largest loads will occur.
- What dynamic behaviour could be expected.
- Static wind and snow loads that are likely for this type of roof, in order to determine the design loads.

3.1 Structural design for wind

Wind loads for a normal building are usually analysed in a static manner. However for very slender structures dynamic instability can also be a potential problem. Dynamic instability for wind is normally investigated for structures such as bridges, high-rise buildings, chimneys and masts, these structures are all described in Eurocode (CEN, 2005). All these structures are exposed for two-sided flow which is a more unfavourable load case for wind instability. This can be explained with that the attack angle and strength of the oncoming wind can alternate and vary which therefore causes oscillating effects more easily compared with a one sided wind flow (Simiu, 2011). Even if the studied structure is only exposed to one sided wind load, it is at the same time both lightweight and slender which can be problematic for wind instability and therefore require further investigation.

Dynamic excitation from wind can develop from the winds turbulent nature which result in fluctuating loads on the structure. As resonant vibration is one of the main causes for structural failure (ibid.), it is an important part to control in the design phase. Another cause for structural damage is fatigue which is relevant if the critical wind velocity responsible for resonance is frequently occurring (CEN, 2005).

A well-known rule of thumb states that the lowest natural frequency should be below 1 Hz for the resonant response to be of significance (Holmes, 2015). However, the dynamic response is also dependent on the structural- and aerodynamic damping. High-voltage transmission lines for example usually have fundamental frequencies well below 1 Hz, but as the aerodynamic damping for these lines is high, the resonance response is mostly damped out.

To estimate what types of wind instabilities that can occur the following section is devoted to fundamentals in bluff body aerodynamics and possible resonance phenomena in aeroelasticity that can be of interest when designing a flexible structure against wind (Holmes, 2015; Simiu, 2011).

3.2 Bluff Body Aerodynamics

A bluff body can be defined as a body that, as a result of its shape, has separated flow over a substantial part of its surface (Chen and Lui, 2005). As a building normally have sharp edges compared to a air plain wing, it's this type of theory that is relevant for the intended building. To introduce the fundamentals in fluid mechanics, Bernoulli equation, Reynolds number, boundary layers, flow separation, reattachment, negative pressures and drag are briefly discussed below.

3.2.1 Bernoulli Equation

The linear flow in an inviscid (frictionless) fluid can be described by the static pressure p, density ρ and the velocity V, with Bernoullis equation as:

$$p + \frac{1}{2}\rho V^2 = constant \qquad \text{(pressure variation due to elevation is neglected)} \tag{3.1}$$

In eq. (3.1) the first and second term denotes static and dynamic pressure respectively (Simiu, 2011). To understand how this relates to wind pressures on buildings let's take the following example. Two points are considered, point 1 is located far upstream while point 2 is on the windward face of the building (stagnation zone), where the wind velocity $V_2 \approx 0$. This can be expressed with Bernoulli as:

$$p_1 + \frac{1}{2}\rho V_1^2 = p_2 \tag{3.2}$$

From eq. (3.2) it is easy to understand that the pressure at the second point at the windward side is exposed to a larger statical pressure compared with the first point which results in a wind load on the structure. According to Holmes, 2015 the Bernoulli equation is not accurate in the separated flow and wake regions, see fig. 3.1, but can still give a reasonably good prediction for surface pressure coefficients outside the shear layer and wake regions (ibid.).

3.2.2 Pressure coefficient

From the Bernoulli equation (eq. (3.1)) the pressure terms can be used to define a non-dimensional quantity called the pressure coefficient C_p (Simiu, 2011). With V denoting reference wind speed (undisturbed oncoming windspeed), p current pressure, p_{ref} reference pressure (ambient static pressure) and $1/2\rho V^2$ the dynamic pressure, the pressure coefficient can be descried by:

$$C_p = \frac{p - p_{ref}}{1/2\rho V^2} \tag{3.3}$$

The equation in eq. (3.3) is often used in wind tunnel test, in order to map the pressure distribution. As the pressure coefficient is dimensionless it can therefore be used to predict the pressure distribution also on a similar shaped roof. This is for example implemented in Eurocode where the *external pressure coefficient* C_{pe} can be multiplied with characteristic wind pressure q_p at height z_e to estimate the external wind load w_e according to Eurocode (CEN, 2005):

$$w_e = q_e(z_e) \cdot c_{pe} \tag{3.4}$$

3.2.3 Reynolds Number

Another dimensionless quantity that has a wide application in aerodynamics is the *Reynolds number*, which can be seen as a measure of the ratio between internal and viscous forces acting in a flow field. Reynolds number can example be used to predict the flow pattern within fluid dynamics.

With a cross-section and wind velocity denoted LxL and V respectively, the internal force can be written as $\rho V^2 L^2$, while the viscous (friction) forces can be written as $\nu V/L$. Now using the ratio of $\nu = \mu/\rho$ (the fluids kinematic viscosity), the Reynolds number can be written as internal force divided with the friction force according to:

$$Re = \frac{VL}{\nu} \tag{3.5}$$

This equation is often used in wind tunnel test to ensure similarity in flow pattern around the full-scale and the small scale model respectively. This is called the Reynolds number similarity and is often used when testing aerodynamic shapes such as air plane model. For bluff body such as buildings that have big scale difference the Reynolds number similarity is unavoidably violated. This similarity violation has been studied by several researchers who have shown that the Reynolds number can be relaxed for structural modelling under certain conditions, where distinct zones for flow separation (sharp edges) is one of these conditions (Simiu, 2011).

3.2.4 Flow separation and reattachment

Another important phenomenon determining the wind flow and therefore the load on the structure are flow separation and possible flow reattachment. Both these flow phenomena originate from friction that is present at the boundary surface. Here the friction causes decreased flow velocity which also explains why wind speed generally increases with height. Another part of this phenomenon is the speed up effect that occurs when the wind passes a high object. This can be compared with the flow in pipes with different diameters, where a decrease of diameter results in an increase of flow velocity (in order to transport the same volume). The opposite occur with a increase of flow area and can in combination with friction at boundary surface further decelerate the flow and cause flow reversal and flow separation. This is typically associated with formation of a turbulent shear layer as shown in fig. 3.1, which gives a rough visualisation of the flow around a building with sharp edges.

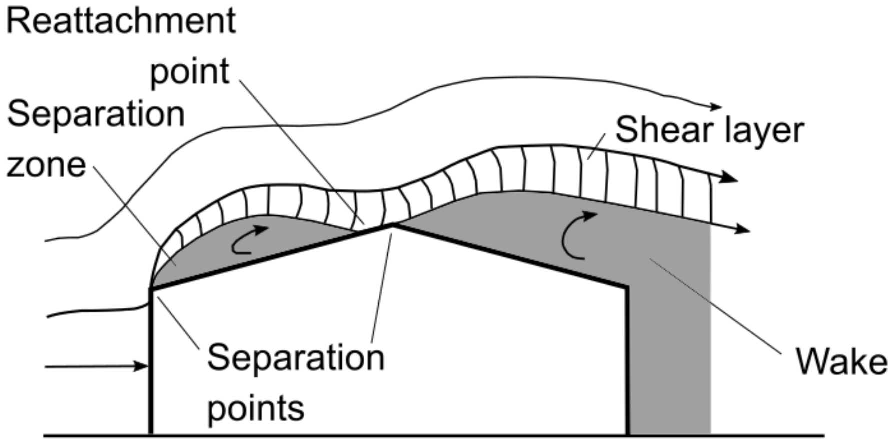

Figure 3.1: Principle of wind flow abound a bluff body with sharp edges
Inspired by: Simiu, 2011

Depending on the flow and the boundary geometry the separated flow can experience reattachment as seen in fig. 3.1. Reattachment normally results in increased pressure on the roof while velocity differences and local vortices in the separation zone and in the wake can create large suctions.

3.3 Wind induced vibrations

With some understanding of the flow patterns around the building, wind effects that cause vibration will therefore be discussed. Dynamic effect is usually divided in vortex-induced-vibration, self-excited vibration and buffeting. These types of vibrations usually occur at different wind velocities and have different response characteristics, seen in fig. 3.2.

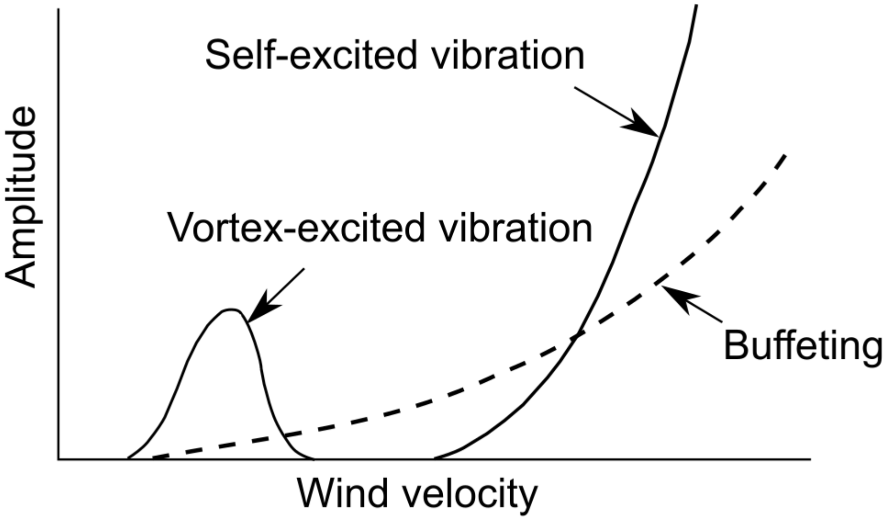

Figure 3.2: Relationship between wind velocity and amplitude for three types of aeroelastic responses
Inspired by: Chen and Lui, 2005, p. 13-16

3.3.1 Vortex-excited vibration

A result of the flow around a building, discussed in section 3.2.4, can be periodic shedding of vortices at some district frequencies, visualized in fig. 3.3.

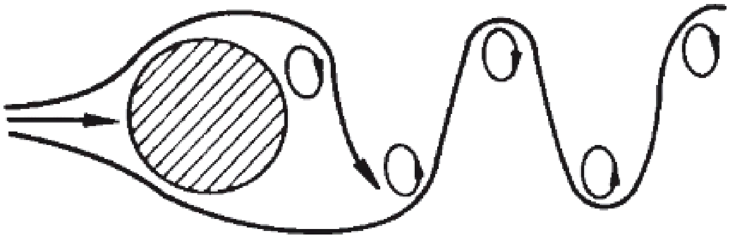

Figure 3.3: Alternate shedding of vortices
Inspired by: Ivoryresearch.com, 2017

This in turn gives rise to a fluctuating lift force which can lead to large vibration amplitudes seen in fig. 3.2, which could ultimately lead to structural failure. Determining the critical frequency for this type of resonance is often complex in large structures, but for cylindrical shapes such as cables, the equation of Strouhals number can be used to predict resonance frequencies (Simiu, 2011):

$$n_s = St\frac{V}{D} \tag{3.6}$$

where

n_s	Frequency of vortex-shedding [Hz]
St	Strouhal number (dependent on cross section shape and Reynolds number)
V	Constant flow velocity [m/s]
D	Characteristic dimension for cross section [m]

If the vortex-shedding frequency n_s in eq. (3.6) coincides with the buildings natural frequency n_1, resonant amplification can occur (ibid.). Experiments show that amplifications can develop also for other wind speeds in an interval of $n_sD/S - \Delta V < V < n_sD/S + \Delta V$. This is an aero-elastic effect and in this interval the vortex-shedding frequency aligns itself with the body's frequency and it's called lock-in effect. The interval can be graphically interpreted as the width of the curve for vortex-excited vibration shown in fig. 3.2. In Eurocode this is considered by calculating a critical wind speed that works as a threshold value which describes at what wind speed resonance starts to become relevant (CEN, 2005). Calculation of a critical wind velocity is also used for other resonance phenomena which unlike vortex-shedding lead to larger resulting amplitude with an increasing wind velocity.

3.3.2 Self-excited vibration

Galloping and Flutter are self-excited vibrations, this type of vibration increases the vibration amplitude by adding force from the motion of the body. This means that once this type of vibration occurs, the amplitude grows without increment of load (Chen and Lui, 2005).

Galloping

Galloping has a deflection parallel or perpendicular to the wind direction, similar to a heaving mode, see fig. 3.4 for an illustration. The amplitude of galloping oscillations is large and in the order of 1-10 times the cross section dimension of the body (Simiu, 2011). Galloping is usually relevant for structures with low natural frequency and low damping. Shapes that are more prone to galloping, ex. rectangular or other non cylindrical cross-sections. A layer of ice on a bridge cable is a typical example where a change of form can lead to galloping oscillation. Galloping usually occurs for structural elements with lower frequencies, or at much higher wind velocity compared with vortex-shedding as seen in fig. 3.2.

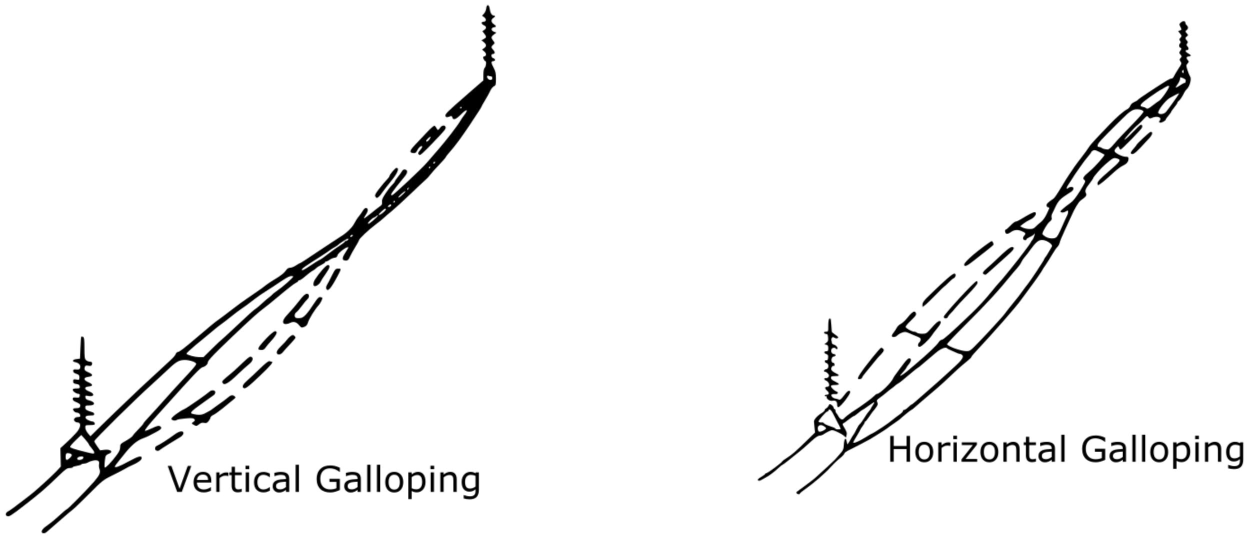

Figure 3.4: Example of galloping vibration on a slender structure (heaving modes)

Flutter

Flutter is a form of coupling effect between two modes of vibration e.g.. heaving modes as well as torsional modes (Chen and Lui, 2005), see fig. 3.5 for an illustration.

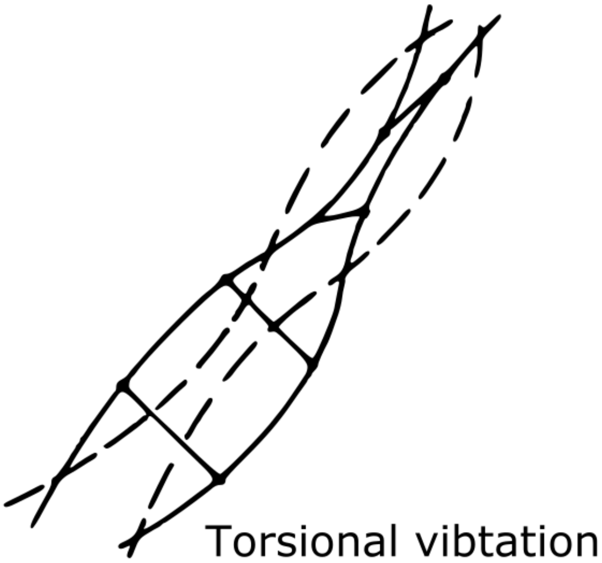

Figure 3.5: Example of torsional vibration (twisting mode), which in combination with heaving vibration seen in fig. 3.4 can describe flutter oscillation

In order to achieve flutter, the vibration frequency between the heaving and twisting mode has to be in similar range. If a bridge deck for example twists, the angle of attack changes. This in turn changes the lift force for the bridge deck, causing it to start flap up or down. This motion also changes the airflow over the bridge deck, which can generate more force and inturn cause further twisting. This describes the growth of flutter and with low damping the amplitude of these type of vibration leads to oscillation that ultimately causes structural failure.

Flutter therefore normally develop in flexible bodies, such as slender bridge decks, as these structures can have low and dense natural frequencies causing them to be prone to flutter (Simiu, 2011). According to Strasky, (2005) a ratio of 2.5 between torsional and bending frequency is sufficient to design a structure against flutter. Similar to galloping, flutter usually occur at high wind velocities (see fig. 3.2) and does not typically occur for buildings (Simiu, 2011). The most famous example of flutter leading to structural collapse is Tacoma Narrows Bridge, which had a main span of 853 m and collapsed at a wind speed of about 19 m/s (Xu, 2013), see fig. 3.6.

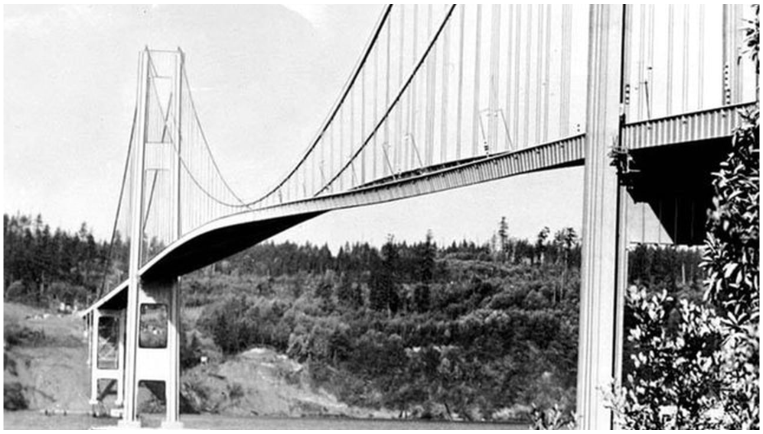

Figure 3.6: Flutter vibration on the bridge deck of Tacoma bridge moments before failure
Image source: Wikipedia, 2009

3.3.3 Buffeting

Buffeting vibration is caused by random loading due to turbulent wind. The velocity fluctuation in turbulent wind gives this type of vibration random properties and the amplitude from buffeting are therefore normally not critical for failure, but can instead be problematic in serviceability limit state (Hermansson and Holma, 2015).

3.4 External loads on the structure

To be able to determine the load on a parabolic shaped roof two different wind tunnel test were used. The first test that was analysed was the scale model of Nagano Olympic Arena (for design purposes), building shape can be seen in fig. 3.7. The second test was studied was the research on hyperparabolic roof shapes (Rizzo et al., 2009a).

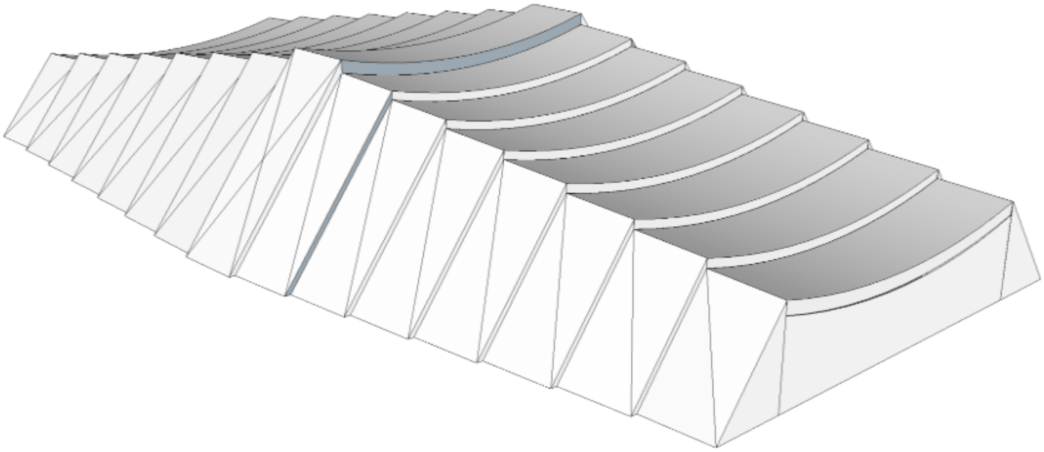

Figure 3.7: Outer shape of Nagano Olympic Arena

In both wind tunnel evaluation of Nagano olympic arena and in the research of hyperbolic roofs, showed that large suction forces can develop over the whole roof. Large suction can be problematic as it could develop compression forces in the stress ribbon elements which can cause instability problems such as buckling.

As the research performed by Rizzo et al., (2009b), was aimed to serve as guideline for design and therefore follows similar rules of calculations as Eurocode in order to give results on the safe side, aswell as the reasearch not being as specific as the scale test of Nagano Olympic Arena. It was decided to base the design load on Rizzo et al., (ibid.) research.

3.4.1 Flow pattern around a saddle shaped roof

The roof shape shown in fig. 3.7 can be referred to as saddle shaped, following a convex curve about one axis and a concave curve about the other. To understand the wind loading on the saddle shaped roof it was important to understand the flow pattern. This has been investigated by Rizzo et al., (ibid.) showing that there were two different behaviours in flow, dependent on the attack angle of the oncoming wind as shown in Figure 3.8. In the studies a scale model of 1:100 with a roof slope of 1/10 L_{max} was used with 155-230 pressure taps that could monitor the pressure distribution over the entire roof (Rizzo et al., 2012a). The pressure was then mapped with mean pressure coefficient shown in fig. 3.10c, here the mapping was scaled in to non-dimensional x/D and y/B coordinates (for depth and width respectively) to be comparable with Eurocode.

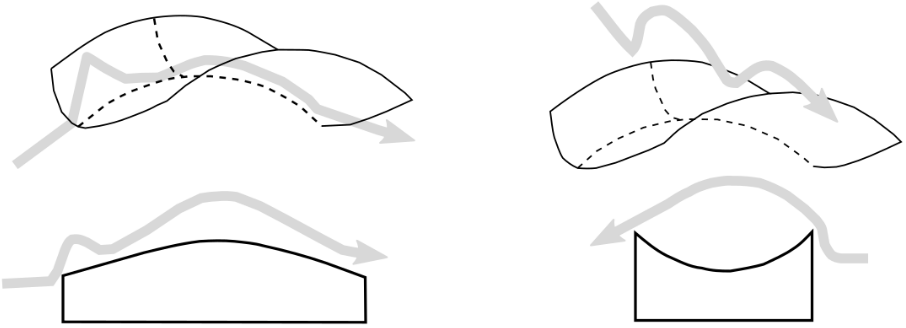

Figure 3.8: Flow pattern over saddle roof
Inspired from: Rizzo et al., (2009a)

From the left flow pattern in fig. 3.8 (oncoming wind 90°), it can be concluded that a spike in suction occurs at the beginning of the roof where flow separation is the most distinct. This means that air just behind the separation zone has a higher velocity because of the speed up effect discussed in section 3.2.4. This higher wind velocity leads to a decreased static pressure according to Bernoulli eq and explains the low pressure (suction) behind the separation zones. After the separation zone the aerodynamic shape causes the wind to follow the curvature resulting in a more moderate suction force which also is reflected in the C_{pe} values in fig. 3.9c.

3.4.2 Mapping of pressure coefficients

With the wind flow around the building known, the pressure coefficient C_p was mapped for both the saddle- (measurement of Rizzo et al., (2009a)) and butterfly roof (Eurocode). Similar to the wind flow the mapping of C_p was divided in an oncoming wind direction of 0°and 90°.

For oncoming wind flow from 90°, compare with left figure of fig. 3.8. The pressure distrubution of both the saddel and butterfly are similar, with a peak of negative pressure just behind face with oncoming wind (inital separation zone, see section 3.2.4).

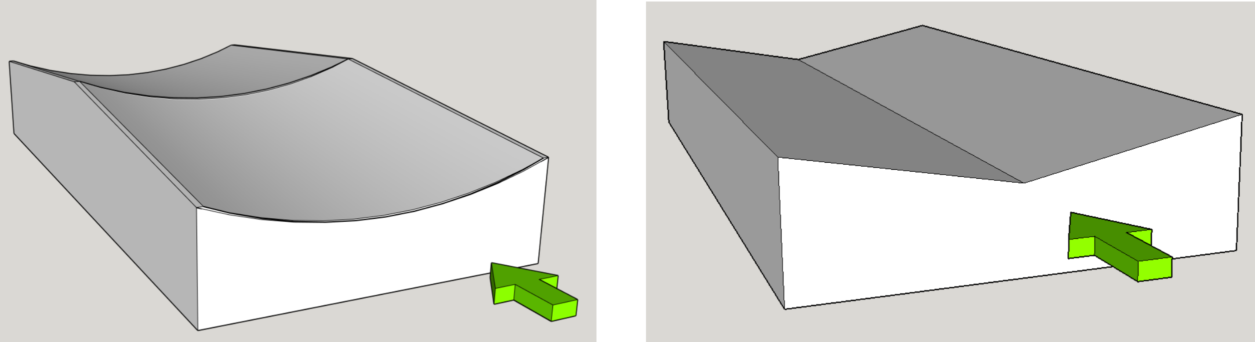

(a) Wind loading on saddle roof $\theta = 90°$ **(b)** Wind loading on butterfly roof $\theta = 90°$

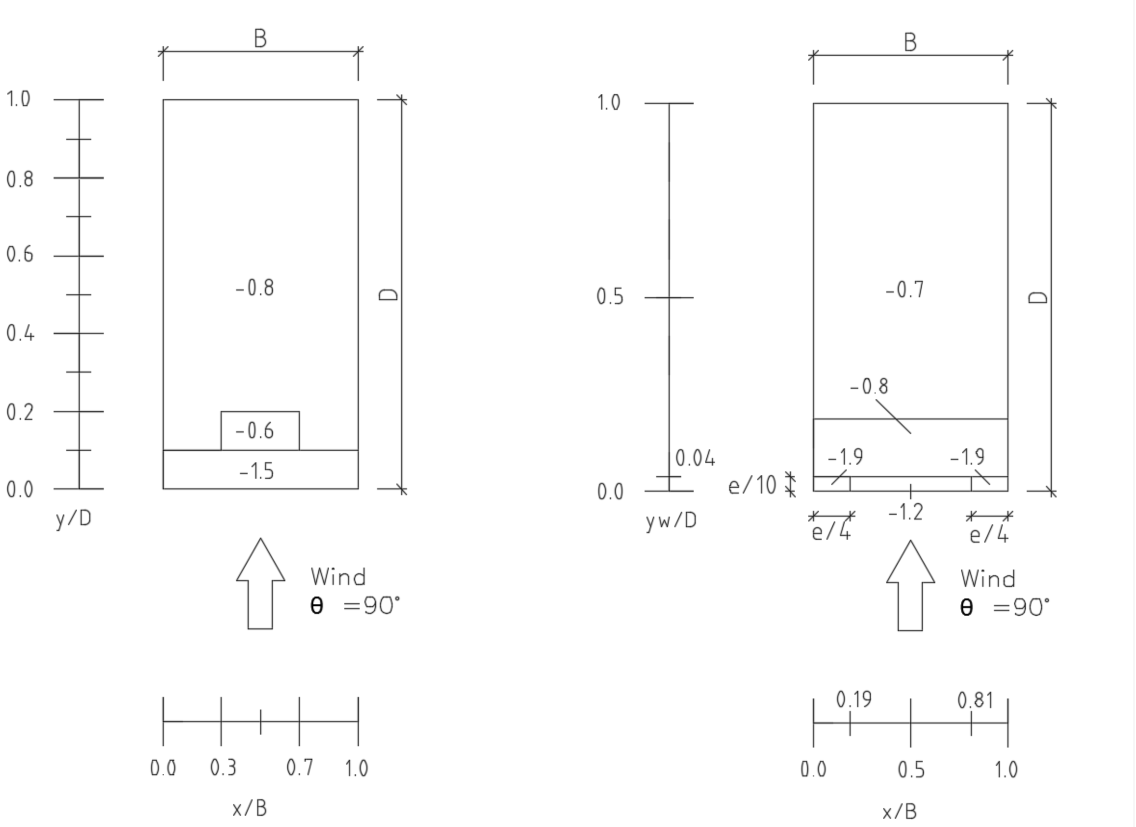

(c) Mean pressure coefficient $C_{p,mean}$ for saddle roof Inspired from: Rizzo et al., (2012a)

(d) Pressure coefficient $C_{pe,10}$ for butterfly roof in Eurocode Inspired from: CEN, (2005)

Figure 3.9: Comparison of C_p between saddle roof and butterfly roof (wind $\theta = 90°$)

For flow pattern for the right figure in 3.8 (oncoming wind 0°), it can be seen that the wind never reattaches to the bowl shaped roof. This results in larger suction across the entire roof, with the highest suction in the initial separation zone and then gradually decreasing according to fig. 3.10.

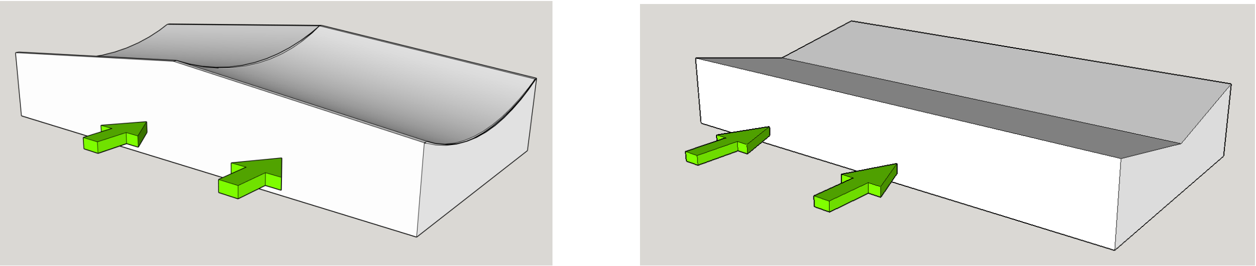

(a) Wind loading on saddle roof $\theta = 0°$ **(b)** Wind loading on butterfly roof $\theta = 0°$

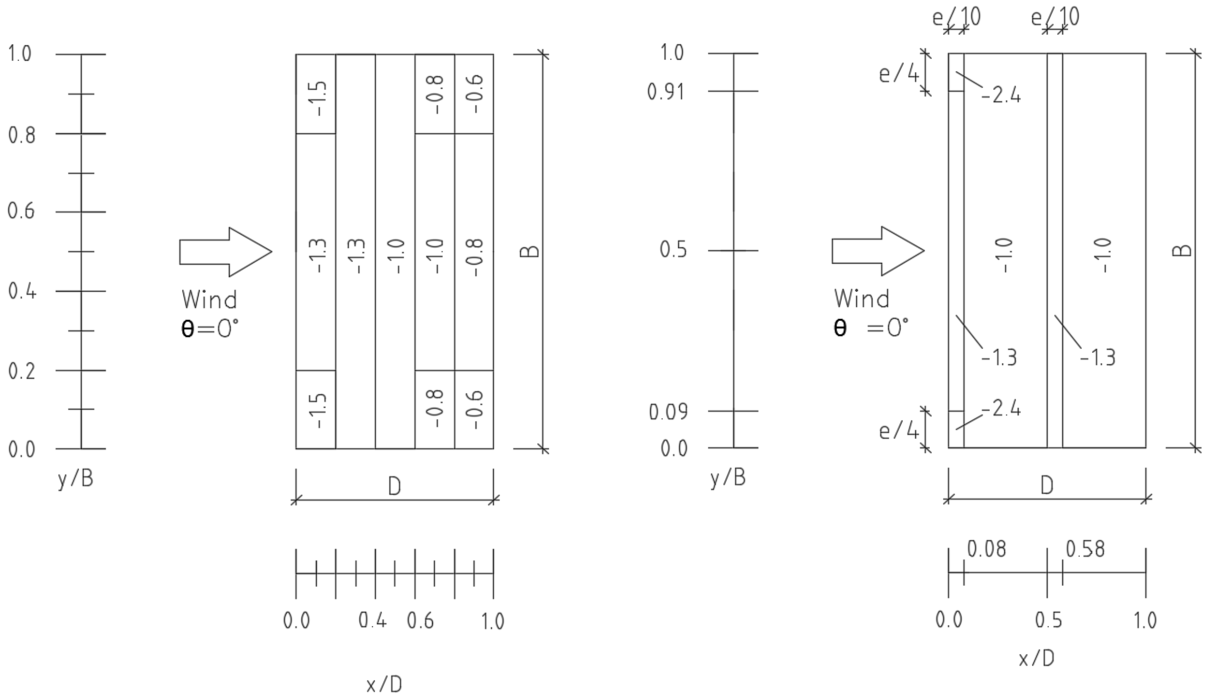

(c) Mean pressure coefficient $C_{p,mean}$ for saddle roof
Inspired by: Rizzo et al., (2012a)

(d) Pressure coefficient $C_{pe,10}$ for butterfly roof
Inspired by: CEN, (2005)

Figure 3.10: Comparison of C_p between sadel- and butterfly roof (wind $\theta = 0°$)

In fig. 3.9 and fig. 3.10 the saddle roof shape is compared with the $C_{pe,10}$ value for a butterfly roof according to Eurocode (CEN, 2005). From this comparison it can be seen that maximum suction in the initial separation is higher in the corner zones for the butterfly roof $C_{pe,10} = -2.4$ compared to $C_{pe} = -1.5$ for the saddle roof. This higher value can be explained by the butterfly roof is using sharper edges and also having smaller zone sizes compared with the saddle roof. With the smaller zone division the peaks at the sharp edgest have a bigger effect on the mean value and therefore result in a higher mean value for the specific zone.From the pressure coefficient in both fig. 3.10 and fig. 3.9, it can also be seen that both the saddle and butterfly roof have no distinct reattachment point as there is negative wind pressure over the roof independent on wind direction.

It could be noted that the wind tunnel test for Nagano Olympic arena confirm a similar pressure distribution as that shown in figs. 3.9 and 3.10. From this wind tunnel test it was also concluded that the long side of Nagano Olypmic arena was more streamlined compared with the scale models of Rizzo, resulting in lower pressure coefficients (Ban et al., 1998).

3.4.3 Snowdrift

Another effect from wind is the redistribution of snow. This occurs when the wind speed at surface layer is greater than the threshold velocity u_* which is about 0.35 m/s for snow particles (Zhou et al., 2016). Redistribution of snow will in turn impact the flow past the building, causing the problem to be time dependent but similar to other variable loads it is only the worst load case that is of interest in design.

The closest approximation for the snow load on this type of roof type was similar to the wind load, the buttery roof shown in fig. 3.11. To further get a feeling of how good this approximation was, scale tests on the two roof alternatives were performed according to section 4.1 and are analysed in section 4.3.1.

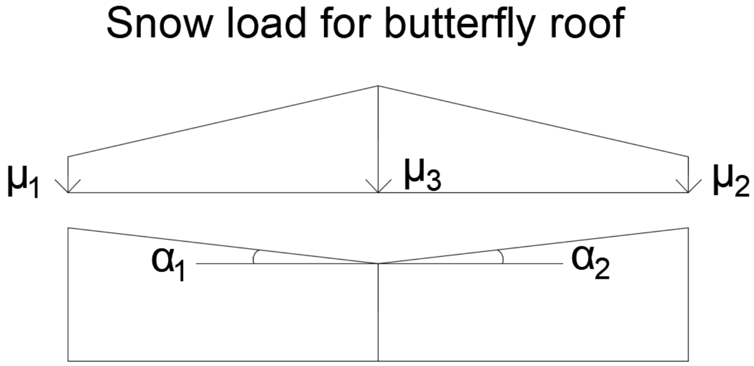

Figure 3.11: Snow load for butterfly roof with snow drift (symmetric if α_1=α_2)
Inspired by: CEN, (2003)

Chapter 4

Laboration

4.1 Background

4.1.1 Wind tunnel testing

Scale tests are often used to get a better understanding of structures. For example, a special design of a building can present potential problems that are not often faced in typical construction, where testing therefore can be used to investigate the structural response. Compared to other laboratory experiments, wind tunnel testing is highly sensitive for example to changes in geometry and surface material. One consequence of this is that even in commercial wind tunnels, results can vary by up to 40 % between different laboratories (Simiu, 2011). According to Holmes, (2015) Simiu, (2011) and Rizzo et al., (2012a), testing on scale models still remain the best reliable means of obtaining aerodynamic data usable for design of engineering structures. This could be exemplified by Rizzo et al., (2012b) where a CFD simulation took 240 hours and was later compared to a wind tunnel test that lasted 8 hours and it could be concluded that the wind tunnel resulted in the more precise data. The biggest drawback with scale test is that they can be expensive especially

4.1.2 Scale relaxation on bluff bodies

Wind-tunnel testing of a bluff body (see section 3.2), such as the model in fig. 4.3, are generally less sensitive to scale relaxation (the ratio between model- and full scale geometry), compared with streamlined shapes. This effect occur as the generated suctions are primary produced in the turbulence caused by flow separation (Stathopoulos and Surry, 1983). This is in contrast to the streamlined shapes which are more dependent on the composition of the oncoming wind. Another factor that simplify scale relaxation was that the model seen in fig. 4.3 was built rigid. This eliminate shape change due to wind loading. An aero-elastic model on the other hand could have been used but this would have required that the scale model mimics the structures actual response, which of course means a much more complex model.

This meant that for geometrically similar models, the wind loading of the roof structure is considered to not be sensitive to changes in scale. As a example of this a study of pressure coefficient could be used as reference. In a study preformed by Stathopoulos and Surry, (1983), the same rigid bluff body was built in different scales (1:100, 1:250 and 1:500) and the pressure coefficients were measured and compared. The result was a error in the order of 10 % between the pressure coefficients for the different scale models (ibid.).

4.2 Materials and methods

4.2.1 Roof shape

Among other things, using a cable like roof shape with a cross section according to figs. 4.1 and 4.2, gives problems with rain and snow accumulation towards the midpoint of the span. This might also be a reason why this type of roof shape is still unusual. To permit surface runoff it is therefore necessary for the roof to tilt in the out of plane direction, this gives rise to two different roof shape suggestions (see figs. 4.1–4.3. From a structural point of view it was therefore interesting to investigate these of this roof shapes was most beneficial against snowdrift, which was one of the governing criteria in design. To determine the answer of this question, scale tests were therefore performed.

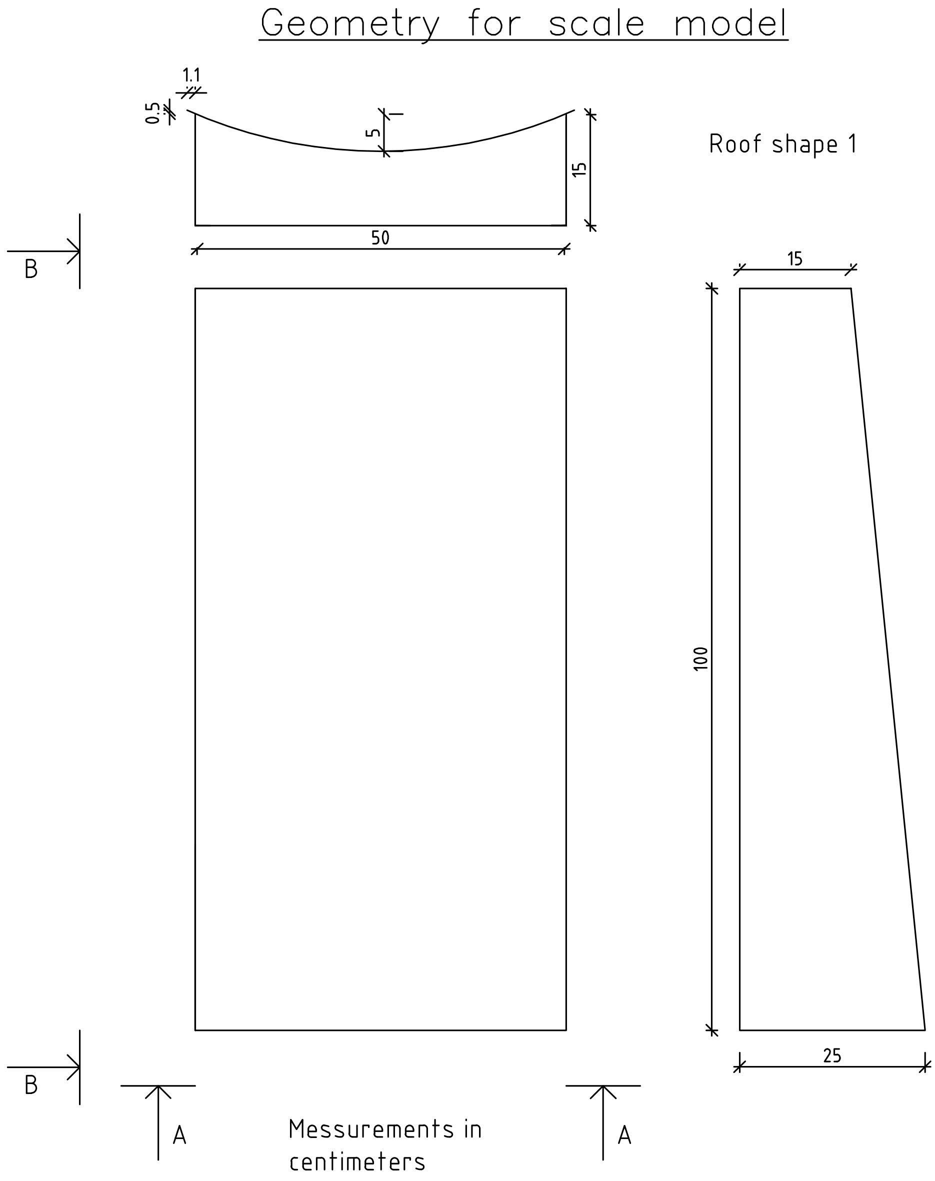

Figure 4.1: Dimensions for scale model with roof shape 1

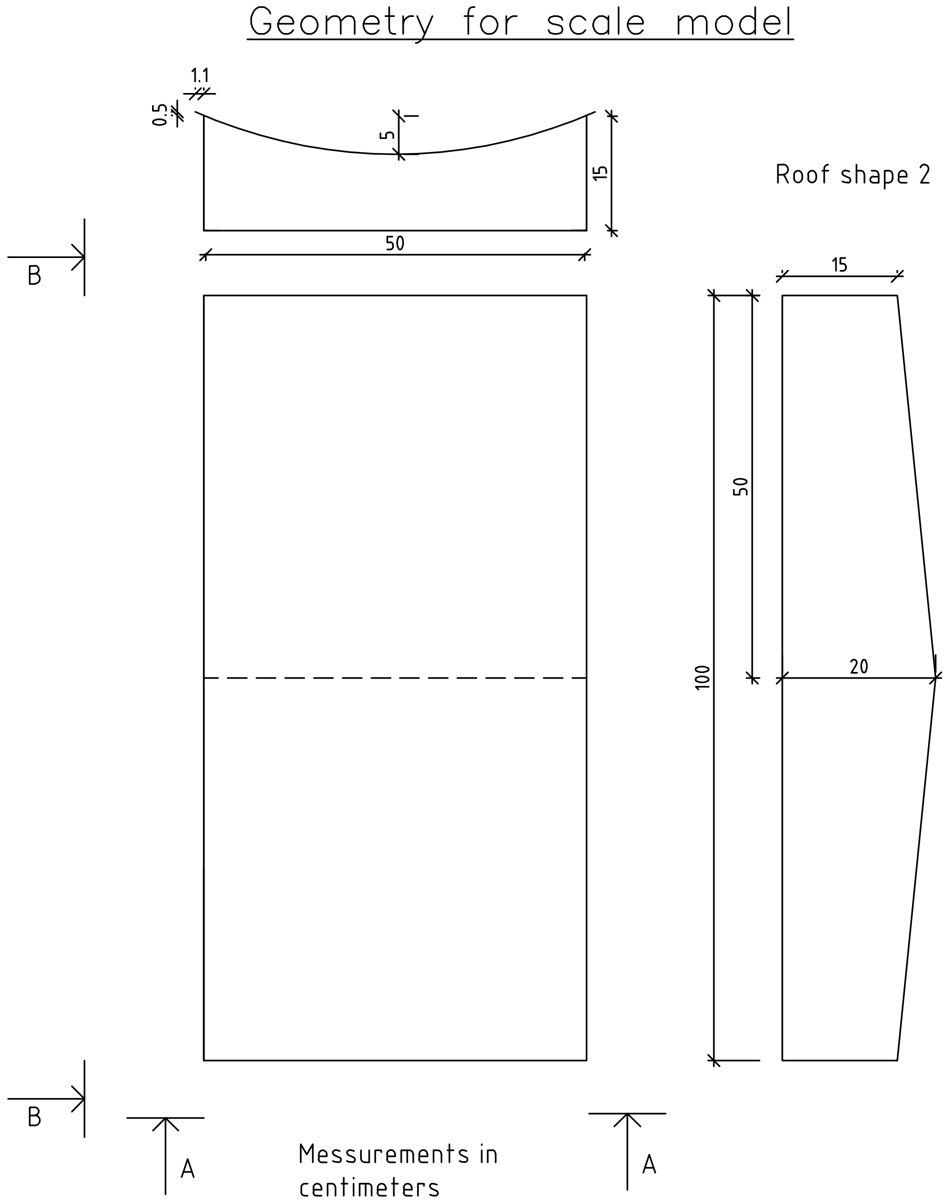

Figure 4.2: Dimensions for scale model with roof shape 2

Figure 4.3: Completed scale model with different roof shape

4.2.2 Material

As the experiment could not use real snow in the simulation, another material with similar properties had to be used. The material that was used was therefore fine grained silica sand which according to Zhou et al., (2014), gives the most approximate results compared with field observation as well as having good similarity conditions compared with real snow particles (see appendix for further information). The material used for the scale test can be divided in timber, sand and nails and screws used to put the model together.

The timber material used was a 18 mm thick wood board, a 12 mm thick plywood board and a 3 mm thick oil coated masonite board. The masonite board was later given a more rough surface, for reasons that will be discussed later in section 4.2.4. The different building blocks were then put together with thin nails to minimise impact on surface area and sealed with latex to prevent uneven internal wind flow. The snow was modelled with sand, having a particle diameter of 0.2-0.7mm which was the closest found resembling the silica sand.

4.2.3 Instruments used in testing

In the experiment two similar fans with a diameter of 40 cm were used. The wind speed was measured with both an anemometer and with a differential pressure gauge to ensure accurate readings. The sand depth was measured with a digital caliper. The accuracy of these instruments is further discussed in section 4.2.6.

4.2.4 Conditions for wind test

The fans were placed 12 cm above ground to achieve an increasing wind speed with height. This is to better mimic the winds natural speed gradient that is present in natural wind (Holmes, 2015; Simiu, 2011).

For wind on the buildings short side one fan was used (fig. 4.4) while wind on the buildings long side required two fans to have a sufficient flow distribution. The two fans were positioned side by side according to fig. 4.5.

Before every wind test a layer of 20 mm sand was added to the roof surface, this layer was then distributed and evened out with a guiding board with 2 cm distances according to fig. 4.6. The sand layer depth was then controlled with a caliper in numerous points to ensure a constant thickness of the sand layer. Sand was then added or removed depending on the situation, followed by a new control until satisfactory sand depth was achieved.

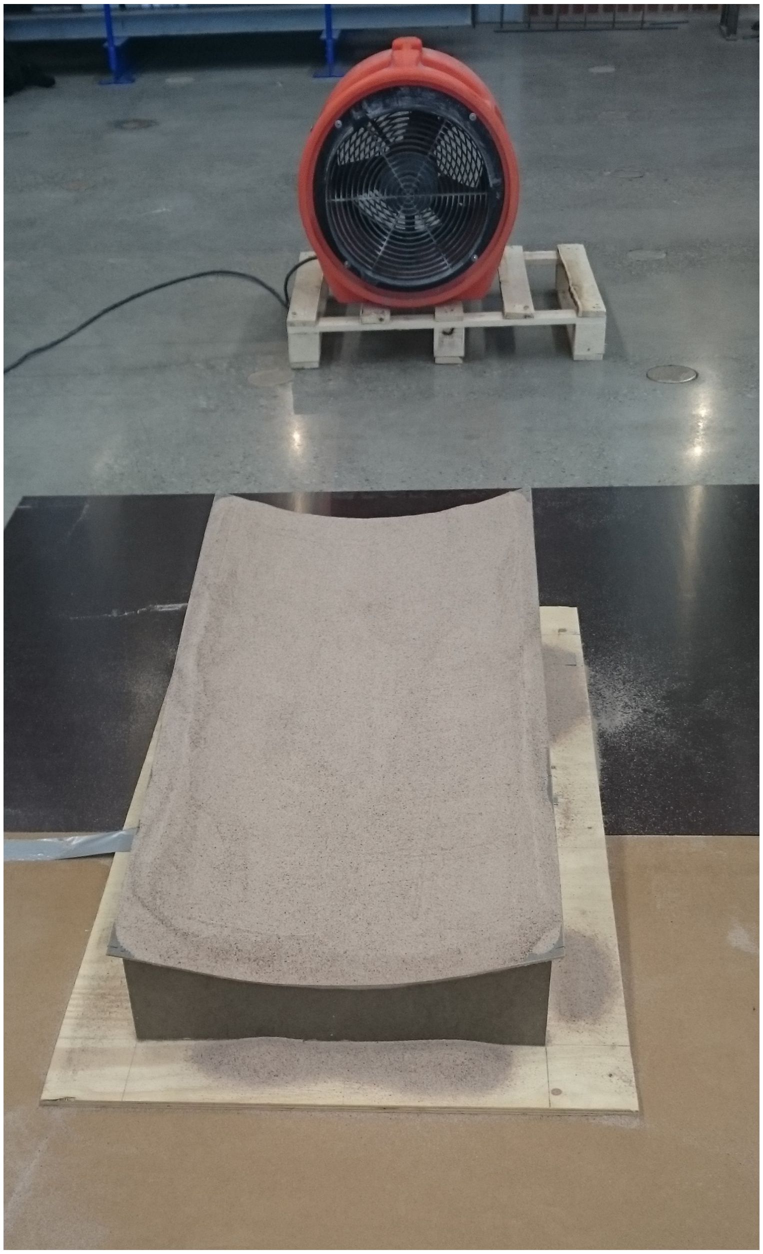

Figure 4.4: Fan position for wind loading on the buildings short side

Figure 4.5: Fan position for wind loading on the buildings long side

Figure 4.6: Guiding board with two 2 cm long strews that helped distribute the sand layer evenly over the entire roof

Surface roughness

Before testing the masonite was sand papered to give the roof a rougher surface, as this was assumed to reduce gliding of particles and therefore give a more unfavourable snow drift. This of course needs to be tested further to determine how it impacts snow drift. Surface roughness is one of the parameters affecting snow distribution according to Eurocode but Eurocode does not explain how this generally affects snow drift (CEN, 2003). One thing to note is that the modelled snow depth will also affect the friction force between particles, as well as the current weather conditions of the snow.

Terrain roughness was not modelled in the test and therefore consists of smooth concrete surface which was believed to correspond to a very open terrain with negligible vegetation.

Test duration and fan characteristics

The duration of the experiment was determined by observation, which meant that the time was measured between the start of the experiment and until no significant redistribution of sand could be observed. This gave a duration of test length t=4 min for all the experiments. One thing to note was that the time for steady state to develop was longer for the test with the fan closer to the model and was therefore the deciding factor for the duration of the test.

The simulation consists of wind loading from two different distances between the fan and the model. This meant that with an "open wind tunnel", the fan could run on a constant speed but still produce different wind velocities. The two distances used in testing were 1.5 m and 2.5 m between the model and fan respectively. Here the closer distance simulates a higher oncoming wind velocity.

To determine the flow distribution of the fan, a side test of wind speed at separate points without the scale model were made. In this test the wind velocity was measured at distances of 1.5 m, 2.0 m and 2.5 m from the fan, with three measurement points at each distance. The three different points were -25 cm , 0 cm and +25 cm from the centre line of the oncoming wind according to fig. 4.7. These points in fig. 4.7 represent an oncoming wind on the models corners and midpoints. The evaluation of these points was also used to determine the conditions for later analysis, here the oncoming wind velocity was set as the velocity at the midpoint (0°), at the distances of 1.5 and 2.5 m respectively (see section 4.3).

From fig. 4.7 it can also be seen that the test with one fan has more measuring points which also served as a calibration of the three different measurement techniques used in the test. These three techniques consist of the digital anemometer, differential pressure gauge with direct wind speed readings or from dynamic pressure readings. The measurement points with two fans also showed similar behaviour to the test with one fan, even if the perpendicular wind distribution was more even. This was understood when the measurement of fig. 4.7a and fig. 4.7b was compared, at the distance of 1.5m and at the height of 40cm between the fan and the model.

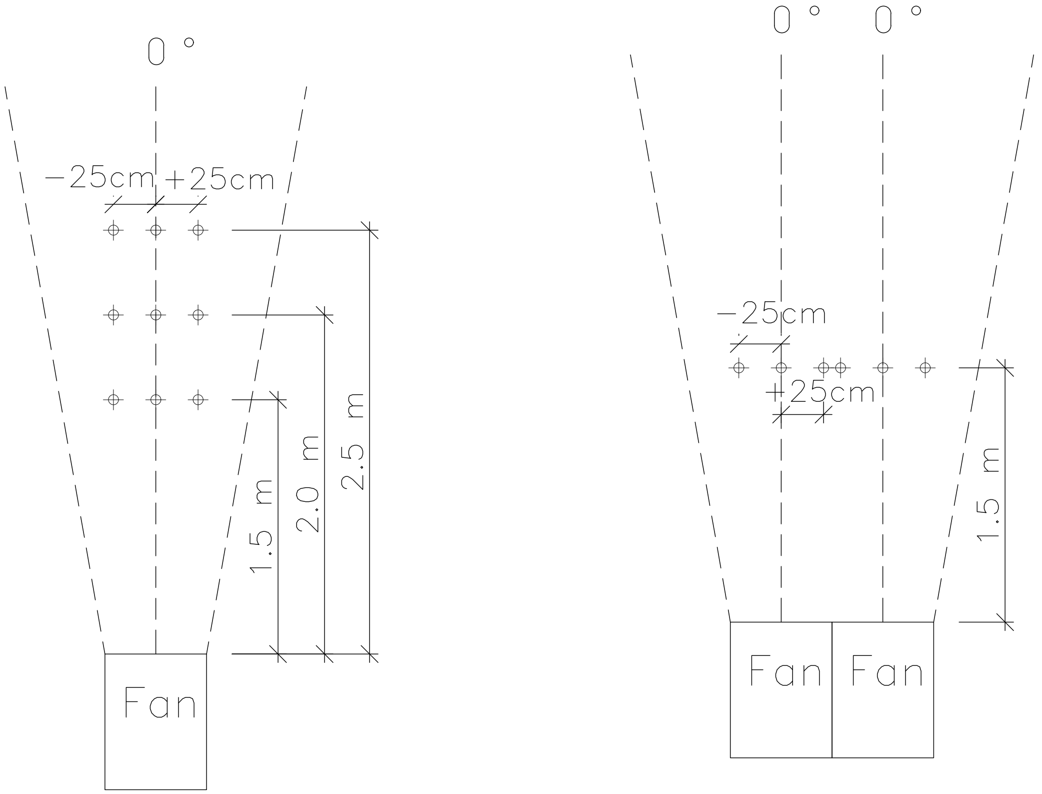

(a) Measuring points for wind velocity with one fan

(b) Measuring points for wind velocity with two fans

Figure 4.7: Sketch of measuring points for wind speed

The differential pressure gauge used for wind speed evaluation could be calibrated for both a direct reading of velocity in (m/s) and a dynamic pressure (Pa).The most accurate reading of the wind velocities was considered to be from the dynamic pressure readings accoring to Norberg, (2017), as this instrument is regularly used in aerodynamic experiments. To translate the dynamic pressure to a wind velocity, the air density ρ_a was first calculated according to the *ideal gas law*:

$$\rho_a = \frac{P_s}{RT} \tag{4.1}$$

where

P_s	static atmospheric pressure
R	Specific gas constant for dry air
T	Air temperature

When air density was known the wind velocity for an incompressible flow was calculated from the dynamic pressure P_d as (eq. (3.1)):

$$V = \sqrt{\frac{2P_d}{\rho_a}} \tag{4.2}$$

With the wind velocity calculated according to eq. (4.2), the wind gradient could then be plotted and compared with the fitted power law for wind-speed profile (Crawley and Dillon, 1993), seen in fig. 4.8

$$V_z = V_g \left(\frac{z}{z_g}\right)^{\frac{1}{\alpha}} \tag{4.3}$$

where

V_z	Wind speed at height z
V_g	Gradient wind at gradient height z_g
α	Exponential coefficient

In this calibration test the best fitted curve between the measurements at different heights and eq. (4.3), was achieved by having the calibration point at height $z = 50$ cm and choosing $\alpha = 5$, see fig. 4.8.

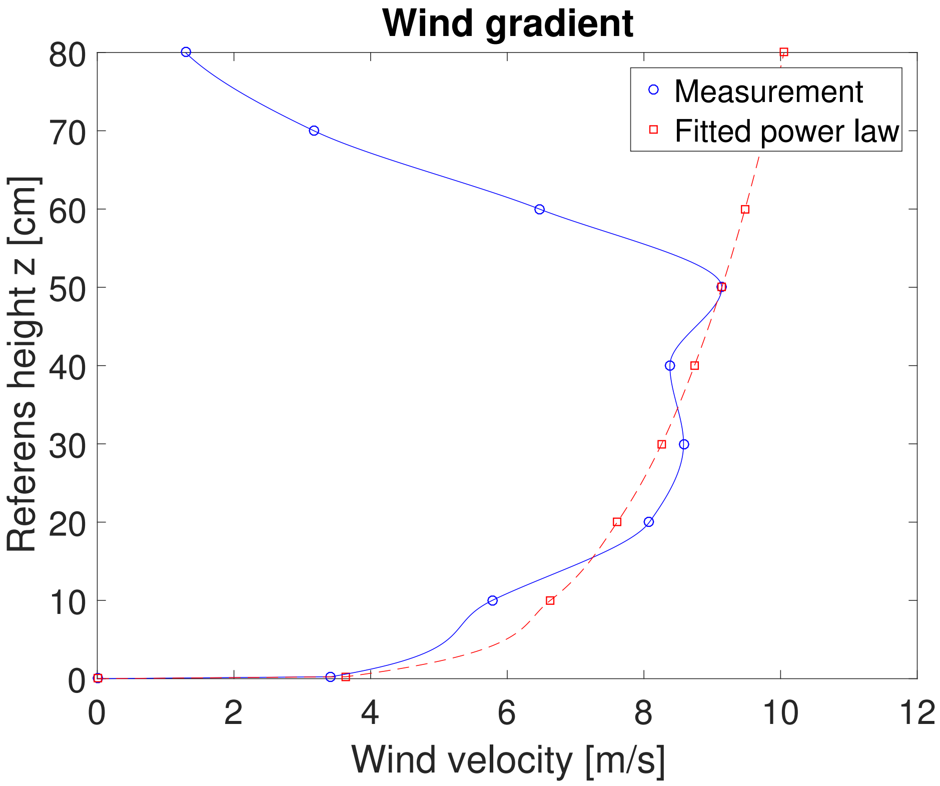

Figure 4.8: Wind gradient for the fan used in the experiment (Dist. Fan-model 1.5m 0°, see fig. 4.7a)

From fig. 4.8 it can be seen that eq. (4.3) fits the measurement quite well up to the height z=50 cm. Up to this height an increase of height corresponds to an increase of wind velocity. As the Equation (4.3) is used to model a realistic wind gradient and as the scale model was exposed to the wind gradient between 0-25 cm, the wind loading from the fan was assumed to be sufficient to be able to simulate snow drift.

Loading of the scale model

The models were exposed to wind load from three different angles according to figs. 4.9–4.11. Here the reference of the attack angle of wind $\theta = 0°$ was set in the load carrying direction of the real structure, shown in fig. 4.11. The second roof shape with double roof slope is symmetrical across the midspan and was therefore only tested from the attack angle of $\theta = 90$ and 0 °.

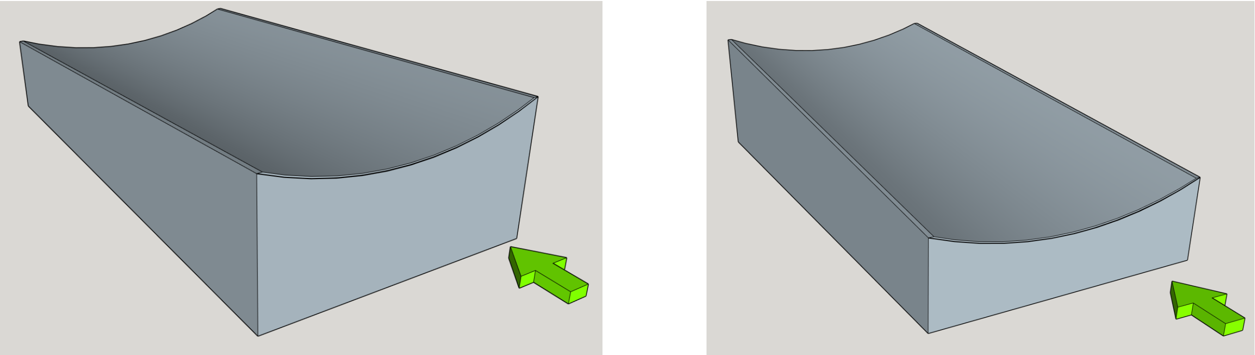

(a) Wind loading for case 1. $\theta = 270°$ **(b)** Wind loading for case 2. $\theta = 90°$

Figure 4.9: Attack angle of wind for load cases 1 and 2

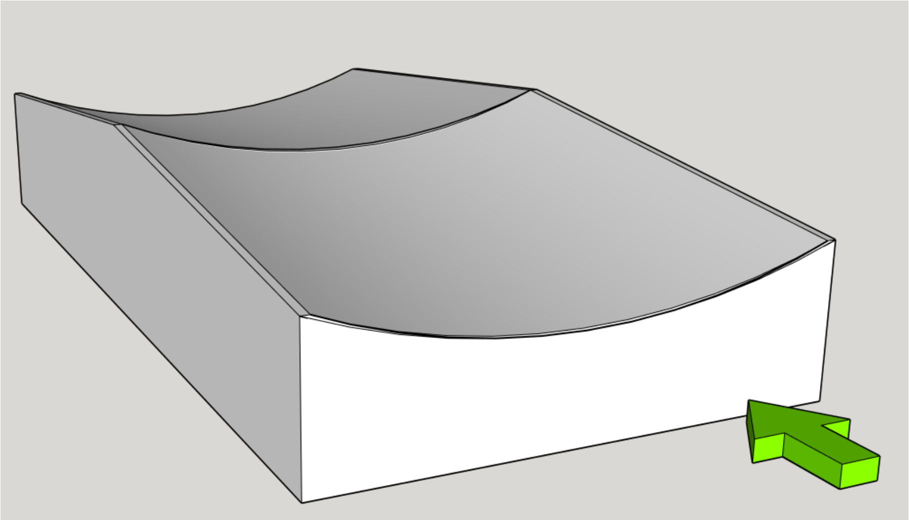

Figure 4.10: Attack angle of wind for load case 3. $\theta = 90°$

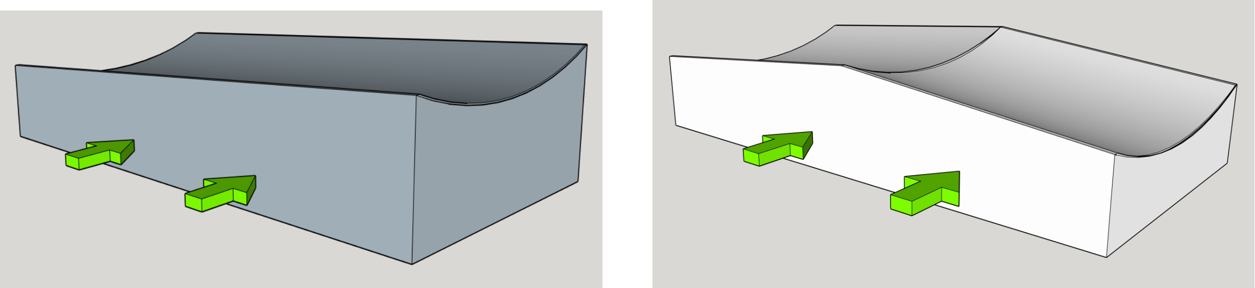

(a) Wind loading for case 4. $\theta = 0°$ **(b)** Wind loading for case 5. $\theta = 0°$

Figure 4.11: Attack angle of wind for load cases 4 and 5

4.2.5 Measurement of snow depth

After a constant wind loading for 4 minutes the fan/fans were stopped and sand depth could then be measured at specific points. The points were divided in a grid with rows B-J and columns from 2-10 according to fig. 4.12. The neglect ion of rows A and K respectively columns 1 and 11 was due to the large sand erosion in these zones and could be assumed to be zero.

Measurement was performed with a caliper and with the guidance of a wooden ruler seen in fig. 4.13. This board were marked with vertical lines similar to the columns 2-10 and aligned with the rows B-J according to fig. 4.12. In this way the measurement could be executed systematically with the same conditions.

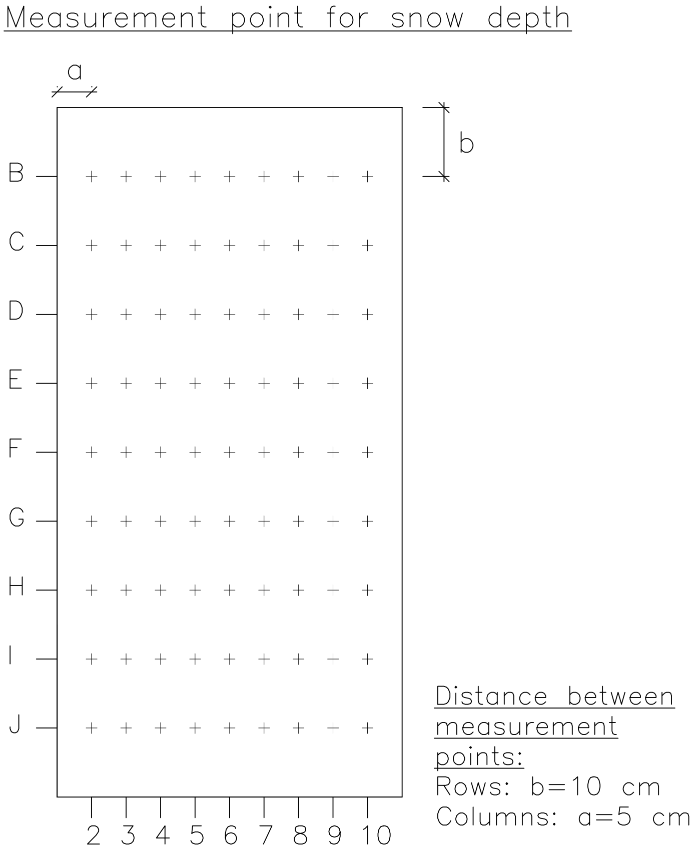

Figure 4.12: Description of location for snow depth evaluation

Figure 4.13: Method for taking point measurement over the roof

With data of snow depth at these 81 points, a surface of the snow distribution over the roof could be plotted with the program MATLAB. To get a finer mesh which simplifies understandings the data was interpolated between measurement point with cubic spline.

4.2.6 Sources of error

In the experiment several approximations have been made despite limited time and resources, get a feeling of how problematic snow drift is for these two types of roof shapes. Uncertainties are also believed to come from human errors, for example in the readings of the snow depth and difficulties in getting a perfectly uniformly thick sand layer over the whole roof. Especially getting the uniform sand depth was time consuming as control measurements were made ocular and sand depth is therefore estimated to locally vary with up to ± 1 mm. Known error sources of wind speed evaluation is ± 5 % error for the anemometer and approximately ± 1 % for the differential pressure gauge.

The fans used in testing were only designed to give a large wind flow and therefore had the drawback of not producing a homogeneous wind flow for both the wind velocity and for the turbulence intensity.

From the test with flow distribution of the fan it could be concluded that the wind load was not symmetrical and that the left oncoming wind (as seen in fig. 4.7) was stronger, for both the case with one or two fans. This correspond to that the resulting wind direction had a different attack angle than the assumed 0°, 90° or 270°. The turbulence intensity in the flow was also a cause of uncertainties even if it was not studied in this test, but could be observed when measuring the wind velocity. The turbulence was from this wind measuring tests believed to be greater at the outer edges of the flow, as wind velocity readings in this zone tended to have a higher fluctuation.

4.2.7 Hypothesis

The zones with the most snow erosion are expected to be in the separation zone and in reattachment points, according to section 3.2.4, as these are areas which locally can have increased wind velocity. Just behind these zones the opposite situation for the wind speed is valid and the largest snow accumulation is therefore anticipated in these areas.

Applying this reasoning to the scale model it would mean snow erosion is expected in the outer boarders of the roof, depending on the wind direction. This means large erosion in row A and K for wind on the buildings short side $\theta = 90°$ and $\theta = 270°$, similarly the most erosion for wind on the buildings long side ($\theta = 0°$) was expected to occur in column 1 and 11. With a two sided sloping roof there is also risk for erosion in row F as this zone is a reattachment point, discussed in section 3.4.1 ($\theta = 90°$).

4.3 Results and Discussion

In this section the result will be visualization as a surface with x- and y- axis describing location while the z- axis describes the sand depth. Before the result is shown, the conditions for the measurement is presented in a table and similarly the result was also summarised in a table.

4.3.1 Determination of design loads

As mentioned in section 4.2.4 a sand layer of 20 mm perpendicular to the surface was distributed evenly over the roof. To easier understand the movement of snow, the measurements from the experiment were normalized, so that the factor 1 corresponds to the original sand depth and scaled up 20 times to make the differences more visible.

To be able to determine the section with the worst load case for the structure, the area under the curves in figs. 4.14–4.18 was calculated for the alphabetical rows B-J (direction of the load bearing elements). With this method the largest load could be determined as the section with largest area under the curve.

As a structure with a cable like behaviour described in section 2.2, the asymmetric loading was also of interest for design in SLS. This was determined similarly to the largest load with calculation of the area under the curve for the rows B-J but here the loads of the two halves of the span were compared, to find the section with biggest difference between the load on the left and right side of the span. In the tests, a coordinate system with x-,y- and z-axis were used. Here the y-axis corresponds to the scale models long side, x-axis the models short side and the z-axis corresponds to the normalized sand depth. In all the tests the same colour scale has been used in order to simplify comparison between the different tests. The tests consist of 10 different measurements using the two different models seen in section 4.2.1. This two models were then exposed to a different wind loads and from different angels which is described in tab. 4.1.

Table 4.1: Conditions for laboration measurements

Test nr.	Load case	Wind speed [m/s]	Attack angle [°]	Distance fan-model [m]	Model type*
1	1	6.1	270	2.5	1
2	1	8.3	270	1.5	1
3	2	6.1	90	2.5	1
4	2	8.3	90	1.5	1
5	3	6.1	90	2.5	2
6	3	8.3	90	1.5	2
7	4	6.1	0	2.5	1
8	4	8.3	0	1.5	1
9	5	6.1	0	2.5	2
10	5	8.3	0	1.5	2

*) Model with (1) one-sided respectively (2) two-sided roof slope

The visualization of the result is presented for the five different load cases discussed in section 4.2.4, meaning that the fig. 4.14a describes the result with a distance between fan and model of 1.5 while the corresponding distance in fig. 4.14b is 2.5 m. This also applies to the for rest of the result presentation in this section.

Visualization of load case 1

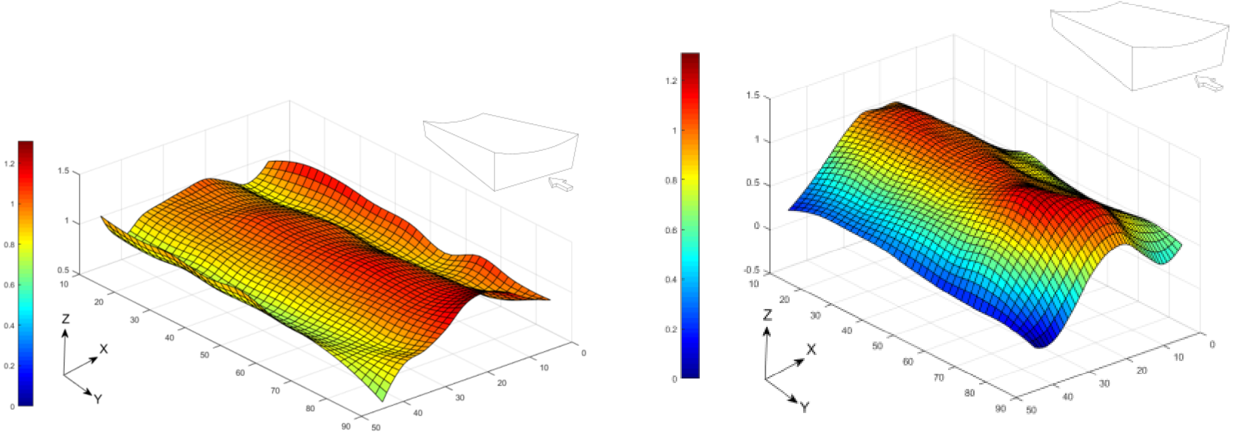

(a) Result of test 1 **(b)** Result of test 2

Figure 4.14: Normalized sand depth for load case 1 see tab section 4.3.1 for more details

In test 1 the largest accumulation of sand was in y=90 (fig. 4.12) which is close to the initial separation zone. In fig. 4.14a it can also be seen that the accumulation is concentrated in the mid part of the span. An observation during test 1 was that the principle particle transport was in the wind direction (along the y-axis). A small transport could also be observed along the x-axis towards the higher edges (x=45 and x=5).

In test 2 a lot more sand was blown off the roof, compared with test 1. This can be seen in fig. 4.14b, where almost all sand depth were lower than the starting value of 1. It can also be seen that the sand depth at the edges (X=0 and X=50) were lower compared with test 1 , as the wind speed in this test was enough to blow the sand over the edge, while the sand depth at midspan almost stayed unchanged ($z_m id \approx 1$). A interesting result from comparing the two test was that the distribution of sand was more asymmetric for test 2, which can be explained by the uneven loading discussed in section 4.2.6, which have a larger effect as the wind speed increase.

Visualization of load case 2

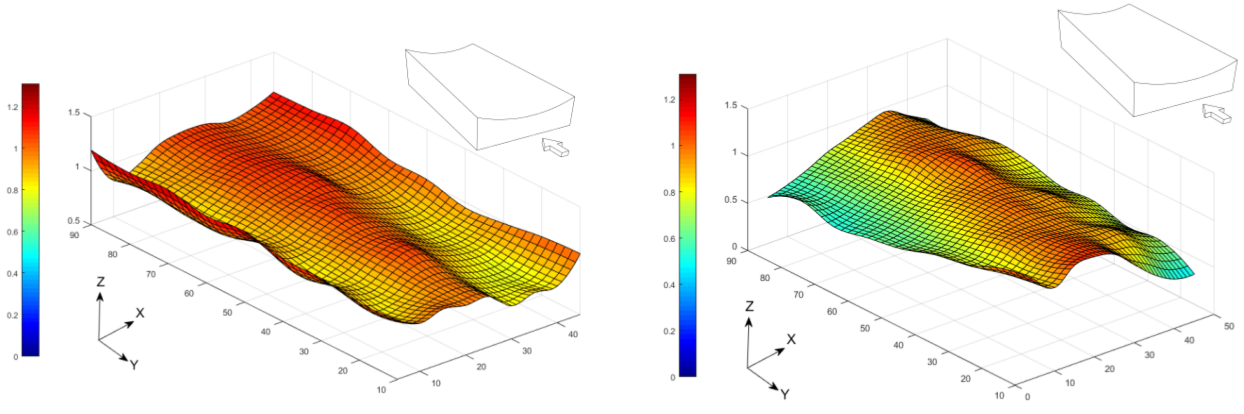

(a) Result of test 3

(b) Result of test 4

Figure 4.15: Normalized sand depth for load case 2 see tab section 4.3.1 for more details

Similar to test 1, the snow accumulation occurs in the middle and the outer edges of the wind exposed span, see fig. 4.15a. From this test the influence of roof slope can be seen as the variation in sand depth is smaller in test 3 (fig. 4.15a) compared to test 1 (fig. 4.14a). From comparing these two cases it can also be seen that there is no distinct accumulation in the initial separation zone, instead a minor erosion occurred at y=10.

The same conclusion can be drawn in test 4. Namely that the roof shape leads to lower variation in sand depth compared with test 2. From comparing test 4 (fig. 4.15b) and test 2 (fig. 4.14b) it can also be seen that no accumulation in initial separation zone but that the overall distribution is similar between a loading from $\theta = 270$ and $\theta = 90$.

Visualization of load case 3

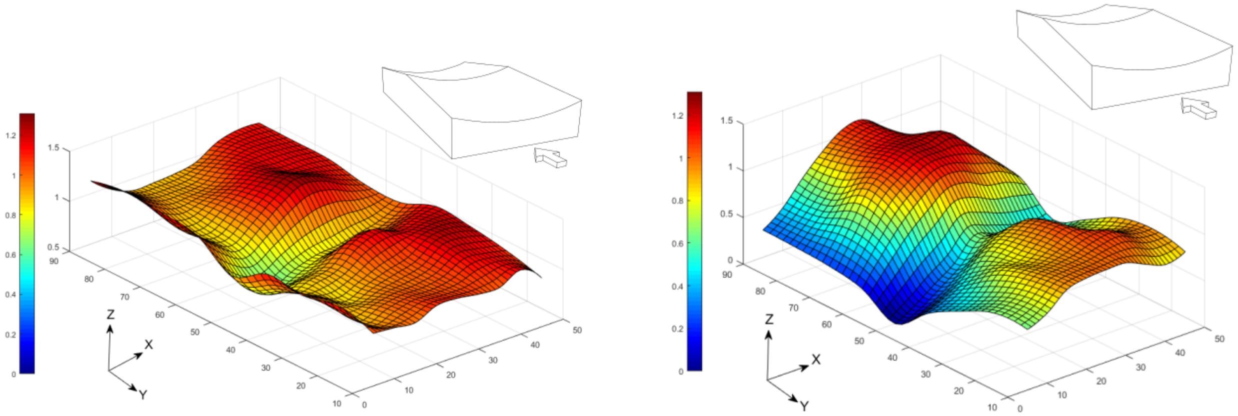

(a) Result of test 5 **(b)** Result of test 6

Figure 4.16: Normalized sand depth for load case 3 see tab section 4.3.1 for more details

For this test 5 and 6 in fig. 4.16 sand erosion can be seen in the midspan of the building (section y=45 in fig. 4.16b). This can be partly explain with the speed up effect discussed in section 3.2.4, which result in locally increased wind speeds. Another reason for large sand erosion in this zone is the use of tape to seal the joint between the two masonite boards as seen in fig. 4.3. This tape gave the section at y=45 a lower surface roughness compared to the rest of the roof which also lead to larger erosion. Even with the large sand erosion at section y=45, the sand drift follow a similar pattern to the model with one-sided roof slope which meant that the result could still be used. For example similarities can be seen between test 6 and test 4 at Y=0-45, same observation can also be seen between 6 and test 2 at Y=45-90.

Visualization of load case 4

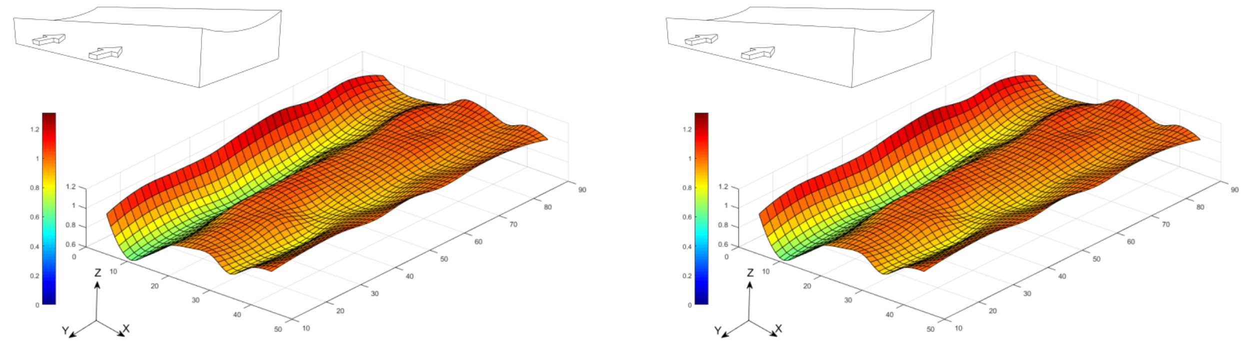

(a) Result of test 7 **(b)** Result of test 8

Figure 4.17: Normalized sand depth for load case 1 see tab section 4.3.1 for more details

From test 7 in fig. 4.17a, it can be seen that most snow drift takes place at x=10 and towards the outer edge of x=5. The impact of roof slope is also visible in fig. 4.17a as particle transport was larger down hill. In test 8, the observed hill in fig. 4.17b at x=45, was moved towards the midspan compared with test 7 (fig. 4.17a). It can also be suspected that some of the sand in column x=0 has blown over the edge as peaks of sand depth in this zone were lower in test 8 compared with those in test 7.

Noteworthy is also that lower variation in sand depth between the low- and high speed tests for the wind on the buildings long-side, compared with test on the buildings short side. This was believed to be connected with the flow pattern over the roof in this direction. According to section 3.4.1, the flow is expected to be over the entire roof in this direction without any reattachments, causing the snow to be shielded from the direct oncoming wind and therefore resulting in less snow drift.

Visualization of load case 5

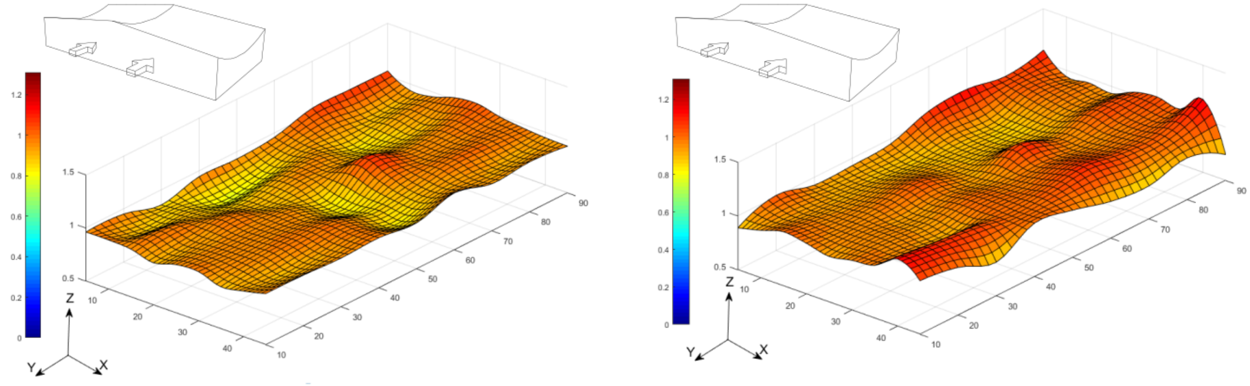

(a) Result of test 9 **(b)** Result of test 10

Figure 4.18: Normalized sand depth for load case 5 see tab section 4.3.1 for more details

Similar to test 7 and 8 the variation in sand depth is less compared with wind oncoming on the buildings short side. From fig. 4.18a it is also apparent that most snow drift occurs in proximity to y=50, but this is also the zone with largest uncertainties as discussed in test 5. An unexpected result from wind loading on this roof shape is the difference in sand erosion between tests 8-10, where in tests 9-10 there is not such a distinct sand drift at x=5.

Comparing test 10 with test 8 it is yet again similarities between the two different roof shapes which are exposed to the same wind load. This can be seen in the build up of the hill at x=5 which is present in both test 10 (fig. 4.18b) and test 8 (fig. 4.17b).

Table 4.2: Result of laboration measurements

Test nr.	Wind speed [m/s]	Attack angle [°]	Larges load (norm.) [-]	Smalest load (norm.) [-]	Most asy. load (norm.) [-]
1	6.1	270	1.07 (y=90)	0.9 (y=20)	0.12 (y=90)
2	8.3	270	0.85 (y=80)	0.47 (y=20)	0.16 (y=90)
3	6.1	90	1.01 (y=90)	0.89 (y=20)	0.05 (y=10)
4	8.3	90	0.89 (y=20)	0.75 (y=90)	0.16 (y=90)
5	6.1	90	1.06 (y=70)	0.80 (y=50)	0.10 (y=60)
6	8.3	90	0.98 (y=70)	0.41 (y=50)	0.14 (y=70)
7	6.1	0	0.99 (y=80)	0.88 (y=10)	0.07 (y=10)
8	8.3	0	0.99 (y=90)	0.90 (y=40)	0.09 (y=10)
9	6.1	0	0.98 (y=90)	0.87 (y=50)	0.04 (y=40)
10	8.3	0	1.00 (y=90)	0.93 (y=30)	0.03 (y=50)

See tab. 4.1 for more details about test conditions

4.3.2 Discussion of scale tests

In most of the tests similarities can be found in the sand drift between the tests exposed to the same wind load. For example both test 1 and 3 showed drift from y=10 and y=40 out towards column y=5 and y=45 respectively. Similarly test 2 and 4 could be compared, but in these tests sand erosion occurs in all outer columns, leaving the sand depth in the mid point of the span almost unchanged.

For wind loading on the buildings long side it can be concluded that the sand is more protected from the oncoming wind and therefore making this direction less dependent on the direct wind flow and instead more influenced by phenomenons like vortex shedding.

The designing load from test occurred for the roof with one sided slope (test 1 and 2), where test 1 gave the largest total load, while test 2 resulted in the largest asymmetric load case. To simply the modelling and comparison of the load with Eurocode, the measured load was translated according to fig. 4.19. In this simplification the area under the curve was preserved, as this can be interpreted as the size of the total load.

In the simplification of the asymmetric load seen in fig. 4.19c, the area under the curve was kept the same as in fig. 4.19a. This is of course a big simplification of the measured load but can be explained by that this load resulted in a load case on the safe side. In this simplification the measured sand distribution was changed to a triangle load similar to the extensive snow drift load case for multi-span roofs, seen in fig. 4.19f. As mentioned above, the area of the triangle matches that of the measurements while the top of the triangle was moved until the same asymmetry about the left and right part of the span was achieved.

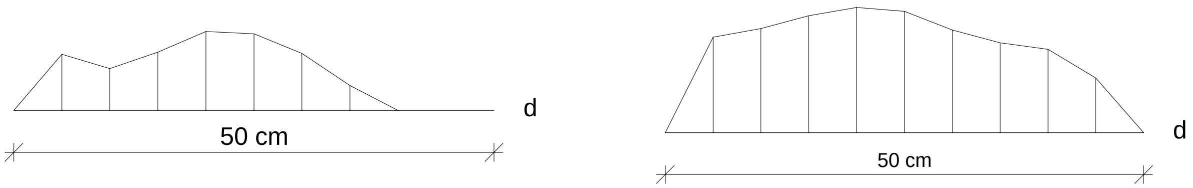

(a) Section with design asymmetric (sand depth from measurements)

(b) Section with design load (sand depth from measurements)

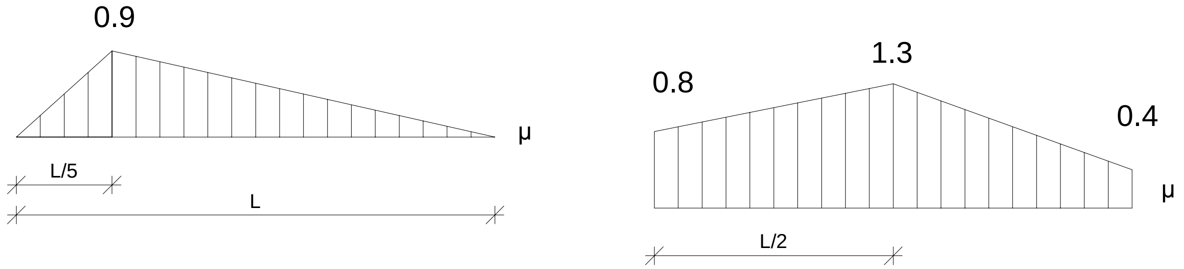

(c) Simplified asymmetric load case from measurements

(d) Simplified design load case from measurements

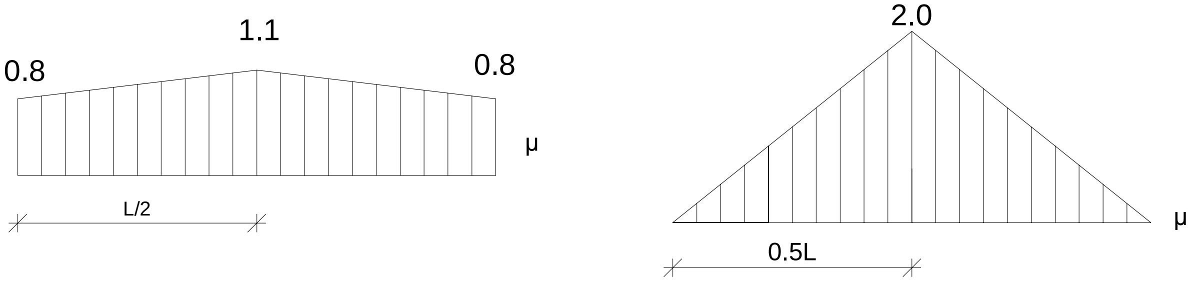

(e) Load case for butterfly roof according to CEN, 2003, kap 5 s16

(f) Load case for exceptional snow drift on multi-span roofs according to CEN, (2003, Bilaga B S26)

Figure 4.19: Comparison of result between measurements and Eurocode

4.3.3 Design load from test and comparison with Eurocode

Again using the area under the curve as a measurement of the load, the size of the simplified measurement loads could be compared to the butterfly roof snow load according to Eurocode. The largest total load from the test in fig. 4.19d had approximately the same area as Eurocode snow load in fig. 4.19e. From figs. 4.19d and 4.19e it can also be seen that there is a difference in symmetry. This difference can be explained with the uneven wind loading on the scale model, as discussed in section 4.2.6. It can therefore be suspected that the load in fig. 4.19d could have been symmetrical which in that case would result in a load of 110 % compared to

Eurocode. The conclusion of this was that the load case for the butterfly roof matches well with the measurement for the design load, but can be considered to be on the unsafe side as safety factors were not implemented for the measured loads.

If exceptional snowdrift can be assumed, a snow distribution according to fig. 4.19f could be assumed as a possible load case (CEN, 2003). Comparing this exceptional snow load it can be conclude that its 105 % of the butterfly snow load. For the asymmetric load case seen in fig. 4.19c there was not found a good comparison in Eurocode. Having this lack of comparison, combined with the errors in the measurement (see Section 4.2.6), the result in this load case can be considered more uncertain.

Chapter 5

Analytical Model

As briefly mentioned in section 2.6, it is important to have some sort of reference when using a FE simulation, as small errors in input data can result in drastically different results. The risk for this problem is especially high in modern FE programs, as these will automatically assume a lot of parameters. Then the reference serves as a quick way to know if the output from FE is realistic (Crocetti, 2016a). As a reference to the FE calculation an analytical model has therefore been developed. This analytical model uses derivations from Marti, (2013) which could then be applied on a specific structure. All the analytical calculations were implemented in MATLAB (see Appendix) which made it possible to plot and compare to the FE calculations (see section 6.3.2).

5.1 Theory of cables (no bending stiffness)

Similar to the evaluation of the buildings natural frequency, parallels can be seen between the behaviour in a cable and the stress ribbon member. This simplification can e.g. be used to calculate the normal force in the stress ribbon member. With a cable approximation, the value of the normal force will be on the safe side as an infinitely stiff beam will carry all load in bending (no normal force) while a cable will carry all load though normal force. From fig. 5.1 the following length for the cable segment can be expressed:

$$ds = \sqrt{dx^2 + dz^2} = dx\sqrt{1 + z'^2} \tag{5.1}$$

Horizontal equilibrium gives ($H^* = H + \mathrm{d}H$):

$$(\rightarrow) \qquad H^* - (H^* + \mathrm{d}H) = 0 \quad \Rightarrow \quad \mathrm{d}H = 0 \quad H^* = \text{constant} \tag{5.2}$$

Moment equilibrium at right side ($\cdot$):

$$(\curvearrowleft) \qquad H^*\mathrm{d}w - V\,\mathrm{d}x + q\,\mathrm{d}x^2/2 + g\,\mathrm{d}x^2/2 = 0 \tag{5.3}$$

As dx is small, the terms with d$x^2 \approx 0$. This results in that the vertical force V in eq. (5.3) can be expressed as:

$$V = H^* \frac{\mathrm{d}z}{\mathrm{d}x} = H^* z' \tag{5.4}$$

Now eq. (5.4) can be inserted into eq. (5.1) which yields:

$$N = \sqrt{H^{*2} + V^2} = H^* \sqrt{1 + z'^2} \tag{5.5}$$

To determine the normal force the similarity between the moment in a beam and the shape of the cable was utilized. This similarity occurs as the cable is assumed to inherit no bending stiffness ($EI \approx 0$) and therefore shapes itself to only carry in tension as discussed in section 2.1.

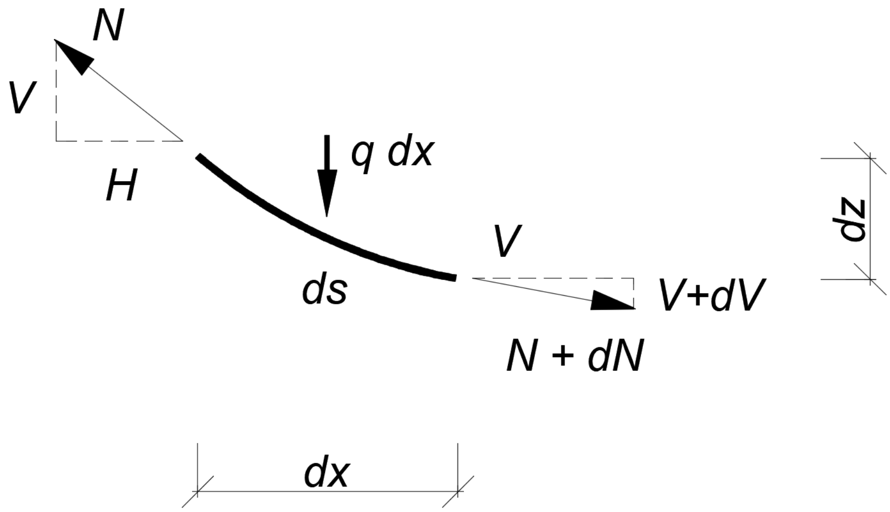

Figure 5.1: Small cable section with length ds

If the beam is assumed to be simply supported, the following equation can therefore describe the cables position (Crocetti, 2016a):

$$z = \frac{\bar{M}}{H^*} \tag{5.6}$$

5.2 Theory of a cable with bending stiffness

As mentioned in section 2.2 the stress ribbon system uses a degree of bending stiffness in order to increase structural stiffness. The bending stiffness in combination with a catenary shape causes the system to have both beam and cable like properties.

The following derivation follows the method presented in Marti, (2013) with conditions according to fig. 5.2. Here the differential equation for a combined cable and beam type response can be expressed as:

$$EIw'''' - (H + \Delta H)(z + w)'' = g + q \tag{5.7}$$

where:

E	Modulus of elasticity [Pa]
I	Second moment of inertia $[m^4]$
w	Deflection [m]
H	Horizontal tension from permanent load [N]
ΔH	Horizontal tension from variable load q [N]
z	Cable curve z(x) see Equation (5.6) [m]
g	Permanent load g [N/m]
q	Variable load q [N/m]

If the permanent load is assumed to be carried only in cable-type response (no resulting bending moment) i.e. $g = -Hz''$, then eq. (5.7) can be rewritten as:

$$EIw'''' - (H + \Delta H)w'' = q - g\frac{\Delta H}{H} \tag{5.8}$$

The general solution for eq. (5.8) is:

$$w = c_1 + c_2 x + c_3 \cosh(\lambda x) + c_4 \sinh(\lambda x) + w_{part} \qquad \text{where} \qquad \left(\lambda^2 = \frac{H + \Delta H}{EI}\right) \tag{5.9}$$

To determinate ΔH the following equation needs to be designated:

$$\int_0^l w'z'dx = \frac{\Delta H l}{EA} \qquad \text{where} \qquad l \text{ is the span length} \tag{5.10}$$

With boundary conditions $w(0) = w(l) = 0$ and assuming a parabolic cable curve with cable sag f for a the permanent load g ($z'' = -8f/l^2$) an integration by parts on the left side of eq. (5.10) gives:

$$\int_0^l w'z'dx = wz'\bigg|_0^l - \int_0^l wz''dx = \frac{8f}{l^2}\int_0^l w\,dx \tag{5.11}$$

Using 5.10 and 5.11 ΔH can be determined as:

$$\Delta H = \frac{8fEA}{l^3}\int_0^l w\,dx \tag{5.12}$$

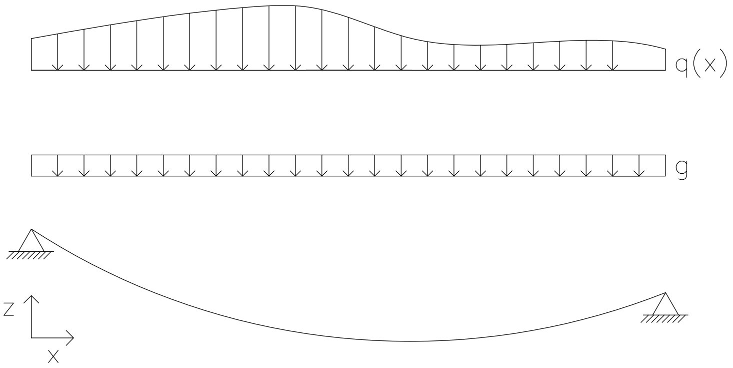

Figure 5.2: Analysed model

5.2.1 Uniform loading on stress ribbon

For the specific case of a symmetric load over the whole span (seen in fig. 5.3), eq. (5.7) can be further expanded.

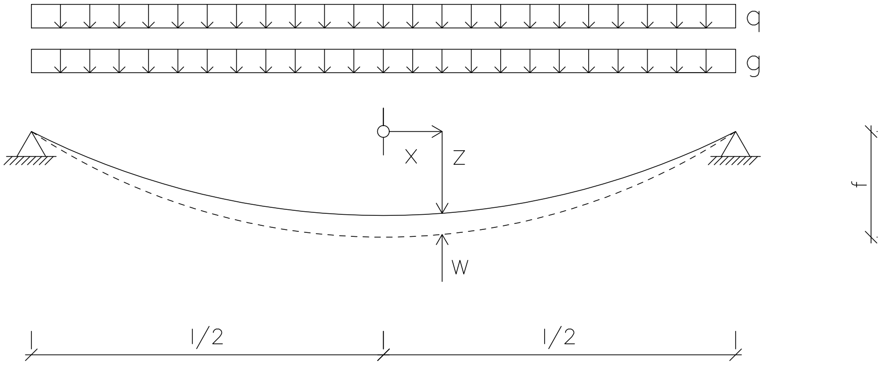

Figure 5.3: Symmetric load case for the stress ribbon element
Inspired from: Marti, 2013, p. 364

Deflection

Now using the theory for a cable with bending stiffness (section 5.2), the equations can be further expanded for the symmetric load case.

First the equations for the deflections were established according to Marti, (2013) below: Using eq. (5.8) for the load case shown in fig. 5.3, with the following boundary conditions $w'(0) = w'''(0) = w(l/2) = w''(l/2) = 0$ gives the following deflection:

$$w = \frac{q - g\frac{\Delta H}{H}}{2(H + \Delta H)} \cdot \left[\frac{l^2}{4} - \frac{2}{\lambda^2} + \frac{2\cosh(\lambda x)}{\lambda^2 \cosh(\lambda l/2)} - x^2\right] \tag{5.13}$$

The horizontal force from the variable load in eq. (5.13) can now be expressed with the help of eq. (5.12) as:

$$\Delta H = \frac{q - g\frac{\Delta H}{H}}{2(H + \Delta H)} \cdot 16 f E A \cdot \left[\frac{1}{12} - \frac{1}{(\lambda l)^2} + \frac{2\tanh(\lambda l/2)}{(\lambda l)^3}\right] \tag{5.14}$$

Moment

Continuing using the theory for the bending stiff cable, the moment of the stress ribbon member could be calculated according to Marti, (ibid.) as:

$$M = -EIw'' \tag{5.15}$$

To determine w'' the second derivative was calculated for eq. (5.13) and gave the following result (Hofverberg, 2016; Marti, 2013) :

$$M = -EI\frac{q - g\frac{\Delta H}{H}}{(H + \Delta H)} \cdot \left[\operatorname{sech}\frac{\lambda l}{2}\cosh(\lambda x) - 1\right] \tag{5.16}$$

Normal force

Here the approximation with a cable with no bending stiffness was used instead (solution on the safe side, as discussed in section 5.1).

According to eq. (5.6), the z-coordinate for a cable can easily be calculated by dividing the moment in a beam with the horizontal force H. With a uniformly distributed load the moment can be calculated with the help of beam tables, see fig. 5.4.

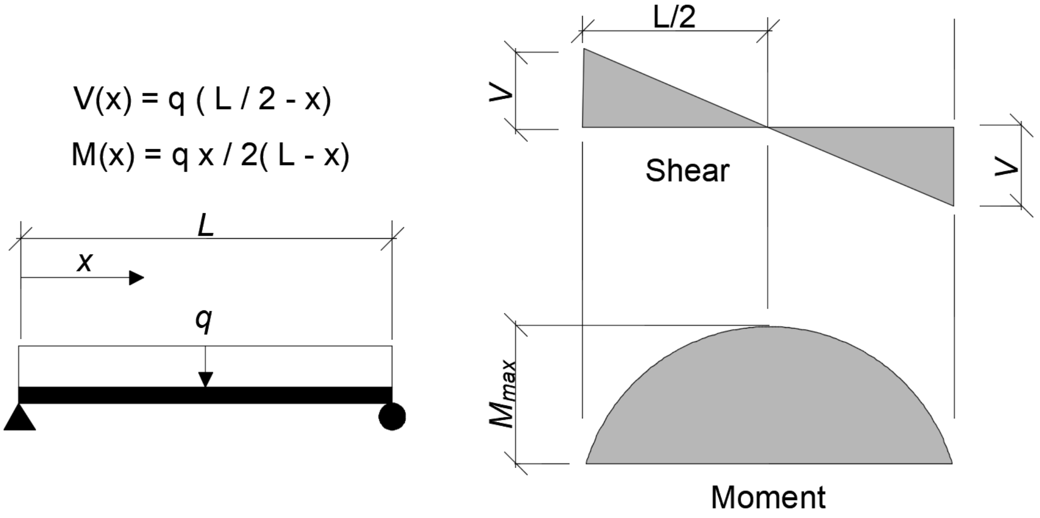

Figure 5.4: Beam table for evaluate the moment when exposed to a symmetrical load
Inspired from: AWC, 2007

The z-position can therefore be expressed as:

$$z(x) = \frac{\bar{M}}{H^*} = \frac{1}{H^*}\frac{qx}{2}(L - x) \tag{5.17}$$

Derivation of eq. (5.17) yields:

$$z'(x) = \frac{1}{H^*}\frac{q}{2}(L - 2x) \tag{5.18}$$

The normal force can now be calculated according to eq. (5.5)

$$N = H^*\sqrt{1 + \left(\frac{1}{H^*}\frac{q}{2}(L - 2x)\right)^2} \tag{5.19}$$

5.2.2 Antisymmetric load

Another special load case that is interesting is for an uneven loading as discussed in section 2.9.

Deflection

A Similar derivation as for deflection in section 5.2.1, can be made for a asymmetric loading case which can be seen in fig. 5.5. This result in the following expression:

$$\begin{aligned} w_1 &= c_1 + c_2 x + c_3 \cosh(\lambda x) + c_4 \sinh(\lambda x) - \frac{q - g\frac{\Delta H}{H}}{2(H+\Delta H)} x^2 \quad (-l/2 \leq x \leq 0) \\ w_2 &= c_5 + c_6 x + c_7 \cosh(\lambda x) + c_8 \sinh(\lambda x) - \frac{g\frac{\Delta H}{H}}{2(H+\Delta H)} x^2 \quad (-l/2 \leq x \leq 0) \end{aligned} \tag{5.20}$$

With the boundary conditions:
$w_1(-l/2) = w_1''(-l/2) = w_2(l/2) = w_2''(0)$

and continuity conditions:
$w_1(0) = w_2(0)$, $w_1'(0) = w_2'(0)$, $w_1''(0) = w_2''(0)$, $w_1'''(0) = w_2'''(0)$

This leads to the following values on constants c_{1-8} in eq. (5.20):

$$\begin{aligned} c_1 &= \frac{\left(q - g\frac{\Delta H}{H}\right) - \frac{l^2}{8} g \frac{\Delta H}{H}}{2(H+\Delta H)} & c_2 = c_6 &= \frac{-ql}{8(H+\Delta H)} \\ c_3 &= \frac{q(\cosh(\lambda l/2) + 1) - 2g\frac{\Delta H}{H}}{2(H+\Delta H)\lambda^2 \cosh(\lambda l/2)} & c_4 = c_8 &= \frac{q(\cosh(\lambda l/2) - 1)}{2(H+\Delta H)\lambda^2 \sinh(\lambda l/2)} \\ c_5 &= \frac{\left(q - 2g\frac{\Delta H}{H}\right)\frac{l^2}{8} + \frac{2}{\lambda^2} g \frac{\Delta H}{H}}{2(H+\Delta H)} & c_7 &= \frac{-q(\cosh(\lambda l/2) - 1) - 2g\frac{\Delta H}{H}}{2(H+\Delta H)\lambda^2 \cosh(\lambda l/2)} \end{aligned}$$

Using the same equation (eq. (5.12)) as for the symmetric case, the horizontal force from the variable load can be expressed as:

$$\Delta H = \frac{q - 2g\frac{\Delta H}{H} f E A}{(H + \Delta H)} \cdot \left[\frac{1}{3} - \frac{4}{(\lambda l)^2} + \frac{8\tanh(\lambda l/2)}{(\lambda l)^3}\right] \tag{5.21}$$

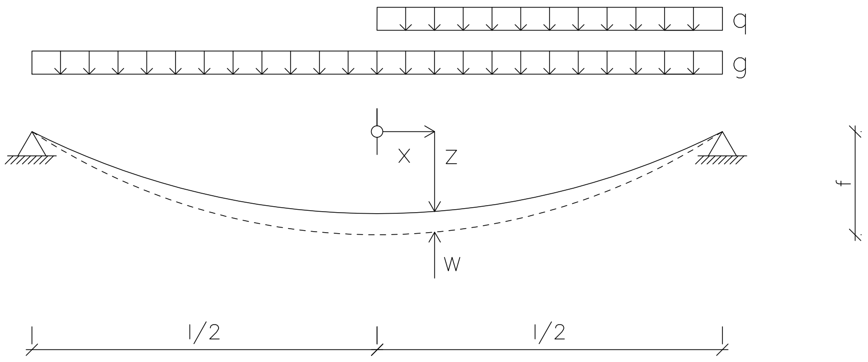

Figure 5.5: Asymmetric load case for the stress ribbon element
Inspired from: Marti, 2013, p. 366

Moment

Using the same solving method as in section 5.2.1, the unknown terms for M and N are w'' and z'. Derivation of eq. (5.20) gives the following result:

$$\begin{aligned} w_1' &= c_2 + c_3\lambda\sinh(\lambda x) + c_4\lambda\cosh(\lambda x) - \frac{\left(q - g\frac{\Delta H}{H}\right)}{(H+\Delta H)}x \\ w_1'' &= c_3\lambda^2\cosh(\lambda x) + c_4\lambda^2\sinh(\lambda x) - \frac{\left(q - g\frac{\Delta H}{H}\right)}{(H+\Delta H)} \end{aligned} \tag{5.22}$$

With no variable load in the second span, corresponding expression for w_2 is:

$$\begin{aligned} w_2' &= c_6 + c_7\lambda\sinh(\lambda x) + c_8\lambda\cosh(\lambda x) - \frac{\left(g\frac{\Delta H}{H}\right)}{(H+\Delta H)}x \\ w_2'' &= c_7\lambda^2\cosh(\lambda x) + c_8\lambda^2\sinh(\lambda x) - \frac{\left(g\frac{\Delta H}{H}\right)}{(H+\Delta H)} \end{aligned} \tag{5.23}$$

Inserting the boundary conditions $w_1''(-l/2) = 0$ and $w_1''(0) = 0$, the constant in eq. (5.22) can now be determined:

$$\begin{cases} c_3''\lambda^2\cosh(\lambda\cdot(-l/2)) + c_4''\lambda^2 sinh(\lambda\cdot(-l/2)) = \dfrac{q-g\frac{\Delta H}{H}}{H+\Delta H} \\ c_3''\lambda^2\cosh(\lambda\cdot 0) + c_4''\lambda^2\sinh(\lambda\cdot 0) = \dfrac{q-g\frac{\Delta H}{H}}{H+\Delta H} \end{cases} \tag{5.24}$$

As cosh(0)=1 sinh(0)=0

$$c_3'' = \frac{1}{\lambda^2}\left(\frac{q-g\frac{\Delta H}{H}}{H+\Delta H}\right) \tag{5.25}$$

Inserting this c_3'' in eq. (5.24) yields:

$$c_4'' = \frac{1}{\lambda^2\sinh(\lambda\cdot(-l/2))}\left(\frac{q-g\frac{\Delta}{H}}{H+\Delta} - c_3''\lambda^2\cosh(\lambda\cdot(-l/2))\right) \tag{5.26}$$

Same method for w_2'' (eq. (5.23)) result in constants according to:

$$c_7'' = \frac{1}{\lambda^2}\left(\frac{-g\frac{\Delta H}{H}}{H+\Delta H}\right) \tag{5.27}$$

Inserting this c_3'' in eq. (5.24) yields:

$$c_8'' = \frac{1}{\lambda^2\sinh(\lambda\cdot(-l/2))}\left(\frac{q-g\frac{\Delta}{H}}{H+\Delta} - c_7''\lambda^2\cosh(\lambda\cdot(-l/2))\right) \tag{5.28}$$

With constants according eqs. (5.25)–(5.28) and deflection according to eqs. (5.22) and (5.23) the moment for the asymmetric load case can be written as:

$$M_1 = EIw_1'' \quad ;-l/2 < x < 0 \qquad \text{and} \qquad M_2 = EIw_2'' \quad ;0 < x < l/2 \tag{5.29}$$

Normal force

Using the same method as for the symmetric case, the normal force was approximated with a cable response. Similar to the symmetric load case the z-position of the corresponding cable was determined with the help of beam tables, see fig. 5.6.

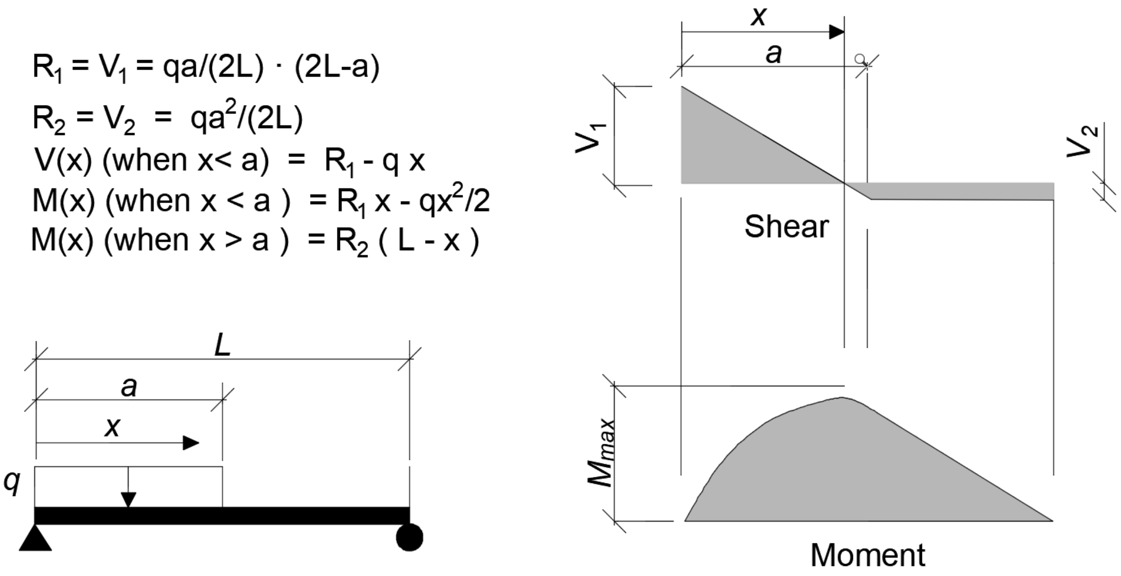

Figure 5.6: Analysed model
Inspired from: AWC, 2007

From fig. 5.6 the z-position for the left zone with live load ($z_{1,q}$) and right zone without load ($z_{2,q}$) are determined:

$$\begin{aligned} z_{1,q} &= \frac{\bar{M}}{H} = \frac{1}{H}(R_1 - \frac{qx^2}{2}) \qquad &\text{where} \qquad R_1 &= \frac{qa}{2L}(2L-a) \\ z_{2,q} &= \frac{\bar{M}}{H} = \frac{1}{H}(R_2(L-x)) \qquad &\text{where} \qquad R_2 &= \frac{qa^2}{2L} \end{aligned}$$

Recalling $N = H\sqrt{1+z'^2}$ and assuming the self weight is evenly distributed, the expression for z' from section 5.2.1 could be used. Superpositioning the normal force for the symmetric load (g) and antisymmetric live load (q) shown in fig. 5.5, the total normal force for a pure cable can be written as:

$$\begin{aligned} N_1 &= H\sqrt{1+z_g'^2} + \Delta H\sqrt{1+z_{1,q}'^2} \\ N_1(x) &= H\sqrt{1+\Big(\frac{1}{H}\frac{w}{2}(l-2x)\Big)^2} + \Delta H\sqrt{1+\Big(\frac{1}{H}(R_1 - wx)\Big)^2} \end{aligned} \tag{5.30}$$

This expression is for the left part of the span and the the same could also be done for the right side of the span. Here the first term corresponds to the normal force from self weight while the second term estimates the normal force from the live load.

5.2.3 Natural modes and frequency

As an estimation of instability is of interest, the structural frequency of a single stress ribbon element was calculated. According to Strasky, (2005) an expression for the natural frequency can be found for a single cable similar to the case shown in fig. 5.7 as:

$$f_{(1)} = \frac{1}{2}\sqrt{\frac{1}{\mu}\left(\frac{H}{l^2} + \frac{EAf^2\pi^2}{2l^4} + \frac{EI\pi^2}{l^4}\right)} \tag{5.31}$$

$$f_{(n)} = \frac{1}{2}\sqrt{\frac{1}{\mu}\left(\frac{Hn^2}{l^2} + \frac{EI\pi^2n^2}{l^4}\right)} \tag{5.32}$$

where

μ	mass of cable per unit length [kg/m]
H	Horizontal force [N]
E	Modulus of elasticity [Pa]
I	Second moment of inertia [m^4]
A	Cross section area [m^2]
l	Span length [m]
n	mode number

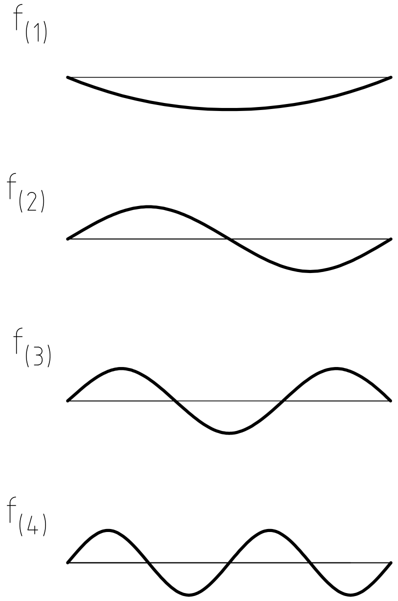

Figure 5.7: Mode shapes of calculated natural frequencys

All the terms in eqs. (5.31) and (5.32) describe how the natural frequency is affected by different parameters. Therefore let's explain the terms, starting with the first term:

$$\frac{H}{\mu l^2}$$

This can be interpreted a pure cable like response and can be compared with the equation for a cable in section 2.3

$$\frac{EAf^2\pi^2}{2l^4}$$

The second term in eqs. (5.31) and (5.32) takes into consideration the normal stiffness of the cable as it has to elongate to vibrate at the first mode. This is another reason why the second mode shape $f_{(2)}$ can have a lower frequency which was briefly discussed in section 2.4.

$$\frac{EI\pi^2n^2}{l^4}$$

The third term describes the bending stiffness of the cable which according to Strasky, 2005, in engineering calculations, is insignificant.

5.2.4 Cross-section properties of stress ribbon element

As indicated by the equations above some properties as bending stiffness EI and axial stiffness EA of the cross-section must be known. The effective bending stiffness EI_{eff} with presumed ridged connection between the composite cross section of plywood (1) and glulam (2) can be calculated for a wood floor according to McCutcheon, (1977):

$$EI_{eff} = EI_u + \frac{(EA_1)(EA_2)}{(EA_1 + EA_2)}\,h^2 \tag{5.33}$$

where EI_u is the summation of the individual stiffness of the plywood and glulam beam and h is the distance between the centroid of the plywood and glulam beam.

The effective axial stiffness EA_{eff} can also be calculated by transforming the composite cross section into equivalent glulam section as seen in fig. 5.8. This homogeneous glulam section was obtained by scaling the width of the plywood with the stiffness ratio according to eq. (5.34) (Crocetti, 2016b) (shown in fig. 5.8):

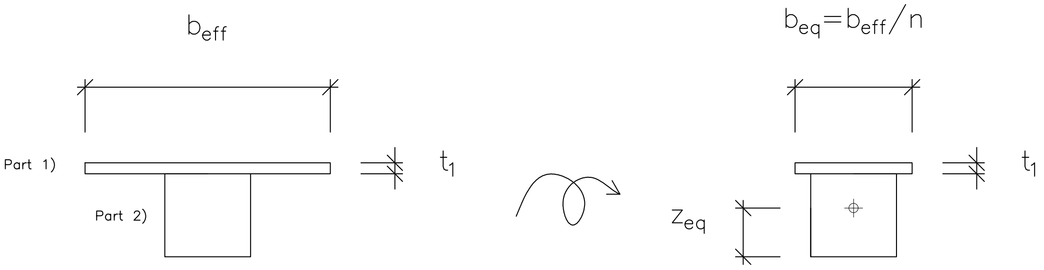

Figure 5.8: Analysed model
From: Crocetti, 2016b

$$A_{ply,eff} = \frac{A_{ply}}{E_{GL}/E_{ply}} \tag{5.34}$$

If the elongation is assumed to vary linearly over the cross-section the combined effective combined axial stiffness EA_{eff} can be determined as:

$$EA_{eff} = E_{glulam}(A_{ply,eff} + A_{glulam}) \tag{5.35}$$

Chapter 6

Finite element model

6.1 Modelling a stress ribbon with different element types

As described in the previous chapter, the load carrying element has neither a pure cable or pure beam response. It is therefore of interest to choose the modelling element in finite element that was the most consistent with the bending stiff cable presented in section 5.2.1. This leads to a short comparison between the element types, specific between the cable- and beam element in the finite element program Rfem with the help of the reference example presented in Marti, (2013, p. 365). The comparison could then determine which element type has the best similarity between the theory and the finite element program.

The load case used in the comparison is the asymmetric load case seen in fig. 5.3.

The cross-section of the reference example consists of a 200 mm deep concrete roof with the following parameters: $g = 5kN/m$, $q = 2$ kN/m, $EA = 6$ GN and $EI = 20$ MNm^2 per metre width of roof. The roof spans a distance of $l = 100$ m as a suspension roof with a sag of $f = 10$ m.

Table 6.1: Similarity between Rfem and reference example in Marti, (2013, p. 365) for an asymmetric load

	u_{max} [mm]	u_{min} [mm]	M_{max} [kNm]	M_{min} [kNm]
Rfem cable element (C)	409,1 (at x=26,4)	-419,8 (at x=76,1)	-	-
Rfem beam element (B)	378,0 (at x=26,3)	-380,3 (at x=76,4)	25,1 (at x=32,5)	25,1 (at x=70,3)
Analytical solution (T)	384,7 (at x=25)	-378,9 (at x=75)	26,3 (at x=25)	26,2 (at x=75)
Diff. for cable (C-A)	24.4	40.9	26.3	26.2
% (Diff./T)	6.3 %	10.8 %	-	-
Diff. for beam (B-A)	-6.7	1.4	-1.2	-1.1
% (Diff./T)	-1.7%	0.4%	-4.6%	-4.2%

From Table 6.1 it can be seen that the beam element have a lower difference between the analytical and the used element type in Rfem in all the compared categories (deflection, and moment) and was therefore used for further calculations.

6.2 Method Parameter study

In this study the following parameters were evaluated: influence of support stiffness, sag and the slenderness of the cross section. To describe the effects of this parameters, the resulting normal force, displacements, moment and natural frequency were compared for different beam cross-sections.

6.2.1 Load cases

In this parameter study two load cases were used in order to understand how the load carrying element would be affected by a symmetric- and asymmetric loading respectively. The approximate force distribution shown in fig. 6.1 and fig. 6.2 helps with the understanding of behaviour of the stress ribbon. The notations in these figures also explains in what points the result of this study was collected. For example the result of the parameter study, that is presented later uses the maximum normal force, displacement and deflection which can be located according to figs. 6.1 and 6.2.

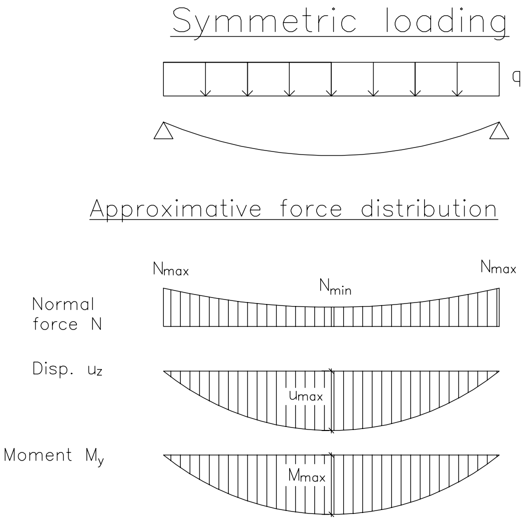

Figure 6.1: Force distribution in the stress ribbon member due to uniform loading. Max/Min values seen here were later used in the parameter study (section 6.3).

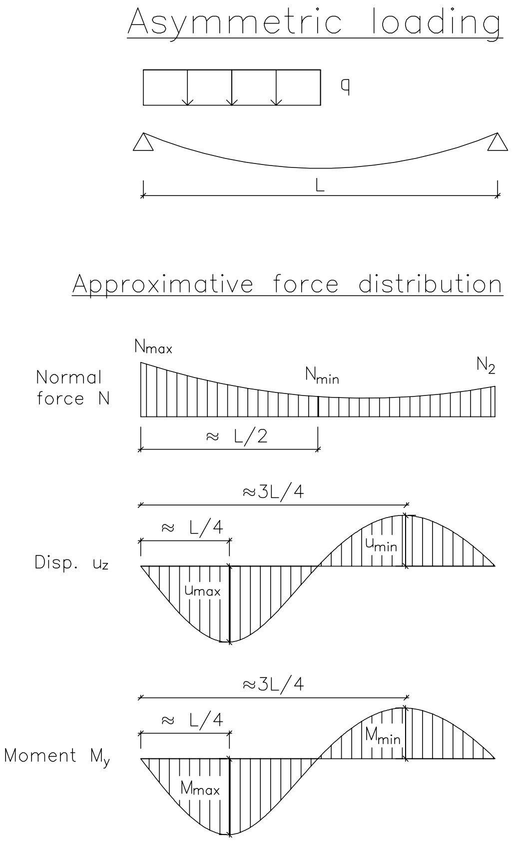

Figure 6.2: Force distribution in the stress ribbon member due to asymmetric loading. Max/Min values seen here were later used in the parameter study (section 6.3).

6.2.2 Determining stiffness of spring support

To determine a suitable stiffness in supports two different column designs were studied as seen in fig. 6.3 and fig. 6.4. The first design consists of two inclined columns with a cross-section according to fig. 6.6, this gives stiffness from two factors. Firstly stiffness comes from maximize the lever arm between supports and secondly by having a stocky cross section, this therefore define the higher boundary for the support stiffness. The second column design in fig. 6.4 instead uses high strength cables as backstays which results in a more slender design and therefore defines the lower stiffness boundary. The stiffness for these two column design was then translated to equivalent linear springs, with the reaction force R and displacement u at column top according to fig. 6.5a.

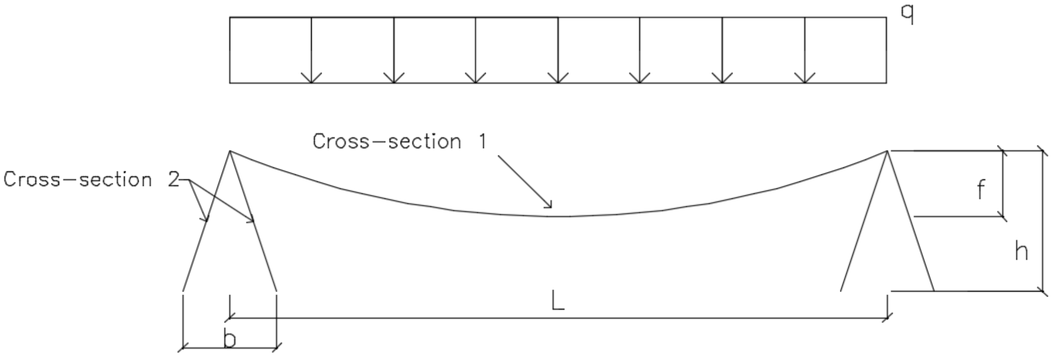

Figure 6.3: Conditions for determining the higher boundary for spring stiffness at column top (see fig. 6.6 for cross-section info)

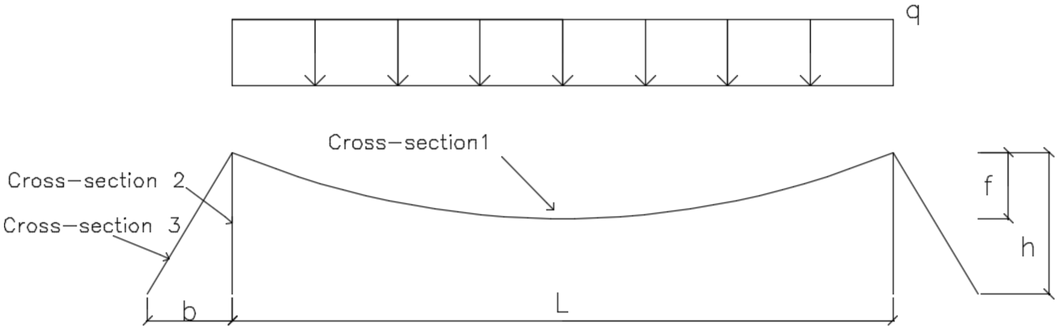

Figure 6.4: Conditions for determining the lower boundary for spring stiffness at column top (see fig. 6.6 for cross-section info)

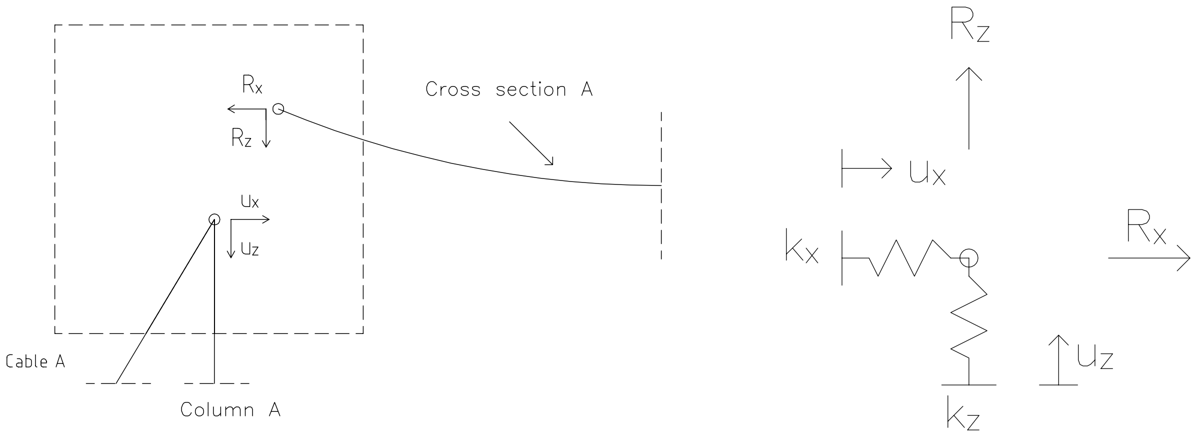

(a) Forces and disp. at column top **(b)** From forces and disp. to linear springs

Figure 6.5: Calculation of the equivalent spring support

6.2.3 Cross-section used for determination of support stiffness

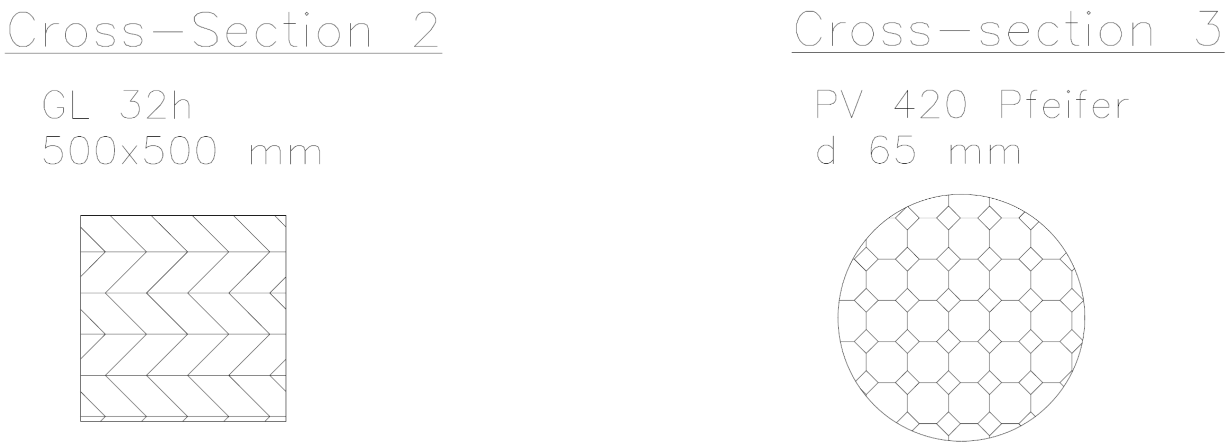

(a) Cross-section for main column (column design 1)

(b) Cross-section for backstay (column design 2)

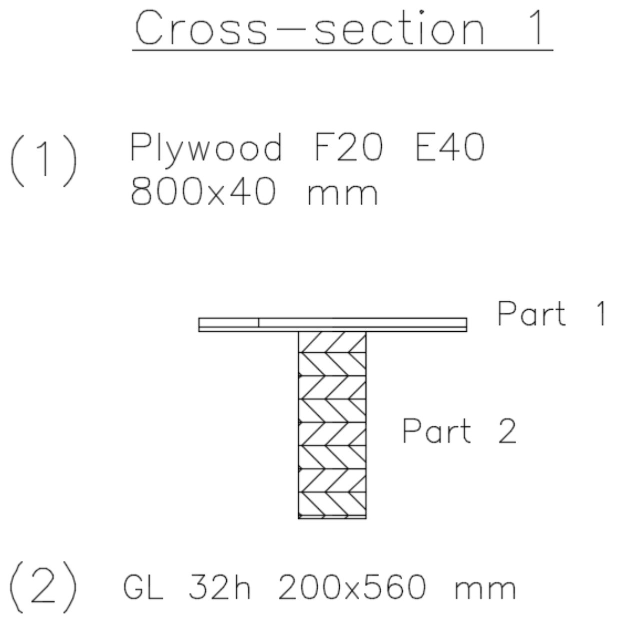

(c) Cross-section for stress ribbon element (design 1 + 2)

Figure 6.6: Cross-section used in parameter study

The reaction force was obtained by dividing the normal force in the cross-section 1 (fig. 6.6c) at column top in a horizontal and vertical component, see fig. 6.5a. This then enabled calculation of a spring with the equivalent stiffness, according to fig. 6.5b and eq. (6.1):

$$k = \frac{F}{\Delta u} \tag{6.1}$$

where

k	Spring stiffness [kN/m]
F	Force in spring [kN]
Δu	Displacement in spring [m]

Using eq. (6.1) it could for example be concluded that the horizontal stiffness in the first column design was 8 times stiffer compared with design two. With values of the low and high boundary of the support stiffness more data points was then linearly interpolated and were then used in the parameter study, see section 6.3.

The stiffness was implemented according to fig. 6.7 with a cross-section shown in fig. 6.6c.

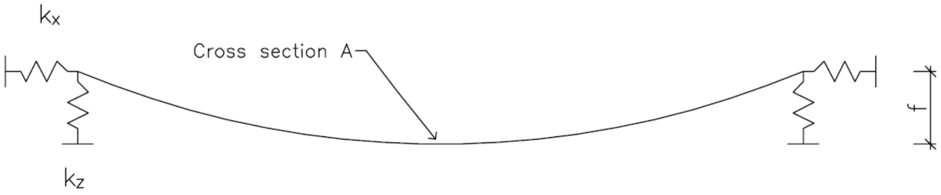

Figure 6.7: Implementation of support stiffness

6.2.4 Determining influence of sag

When studying the influence of sag the supports were assumed pinned and the cross-section used in analysis can be seen in fig. 6.6c (same as for determination of support stiffness). Then the sag was varied in ten points between 2-11 m according to fig. 6.8.

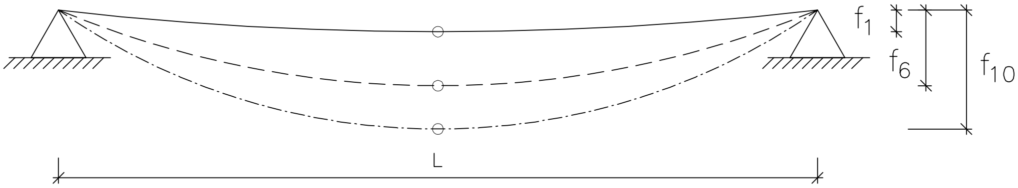

Figure 6.8: Description of the diffrent sag height later used in section 6.3

6.2.5 Determining cross-section for slenderness test

To describe the slenderness of the analysed cross-section the ratio of I/A was used, i.e. the square of the radius of gyration $R_g^2 = I/A$. As this ratio contains two factors, this meant that the study was divided in two parts, first the cross-section area A was kept constant and in the second part the moment of inertia I was kept constant. In this way both the influence of bending stiffness I and the difference of self weight though A could later be evaluated.

The start and end cross-section of the slenderness analysis is shown in fig. 6.9. The dimension originates from that the start and end dimensions for a beam with a constant area. This start dimension were set so that a cross-section with lower hight to width ratio (h/w) didn't seemed likely as this beam have a low bending stiffness (I) which was thought to give the section more cable like responses to loading. Similar reasoning was behind the end cross-sections but here the beam have a really high bending stiffness which instead was to believed to give the section of a more beam type response to loading. The idea with this was to have a reasonable h/w somewhere in this span, in order to determine the optimal h/w for the design.

(a) Start cross-section (A const.) **(b)** Start cross-section (I const.)

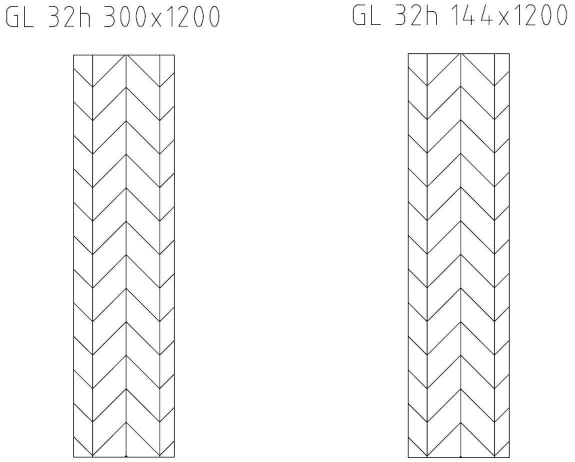

(c) End cross-section (A const.) **(d)** End cross-section (I const.)

Figure 6.9: Start and end cross-sections for the parameter study with of slenderness

Cross-sections for beam with constant A

To obtain cross-sections between the extremes shown in figs. 6.9a and 6.9c the bending stiffness I for the start and end dimension was calculated. Points in-between these I-values were then interpolated similar to the calculation for support stiffness and were then translated to cross-sections according to:

$$h = \sqrt{\frac{12I}{A}} \qquad \text{and} \qquad w = A/h \tag{6.2}$$

where:

h	Cross-section height [m]
w	Cross-section width [m]
h	Cross-section Area [m^2]
I	Cross-section bending stiffness [m^4]

Cross-sections for beam with constant I

With calculated beam cross-sections according to section 6.2.5 the slenderness ratio (I/A) was known for the beam with constant area and using the bending stiffness in the middle of this interval, the cross-sections for the beam with constant bending stiffness could be determined as:

$$A = I_{constI} / \left(\frac{I}{A}\right)_{constA} \qquad \text{and with} \qquad \textit{Equation}\ (6.2) \tag{6.3}$$

With a low slenderness ratio I/A and using a constant I, this meant that the beams with low height resulted in excessive width, seen in fig. 6.9b. This can also be understood by eq. (6.4), as the relationship between the bending stiffness I and beam height h is cubic.

$$I = \frac{wh^3}{12} \tag{6.4}$$

6.3 Result and discussion of parameter study

Recalling from previous chapter, the following parameters were studied:

- Stiffness of support
- Sag of the stress ribbon element
- Slenderness of cross-section

To describe the impact of these parameters for a stress ribbon element with a span of 70m, normal force, displacements, moment and natural frequency were studied and are discussed below.

All the calculation in Rfem were made with third order theory, which is discussed in section 6.4 and it was only in the slenderness study the self weight was considered. The plots are also scaled to enable direct comparison between the symmetric- and asymmetric load case. In these plots the blue line represents the results from the symmetric load (left y-axis) while the red line displays the results for an asymmetric load (right y-axis).

6.3.1 Dependence of support stiffness

Recalling from section 6.2.2 the stiffness of the support was calculated from a stiff to a more slender column design see fig. 6.3 and fig. 6.4, resultings in a model used for analysis shown in fig. 6.4. The data from this analysis is shown in fig. 6.10.

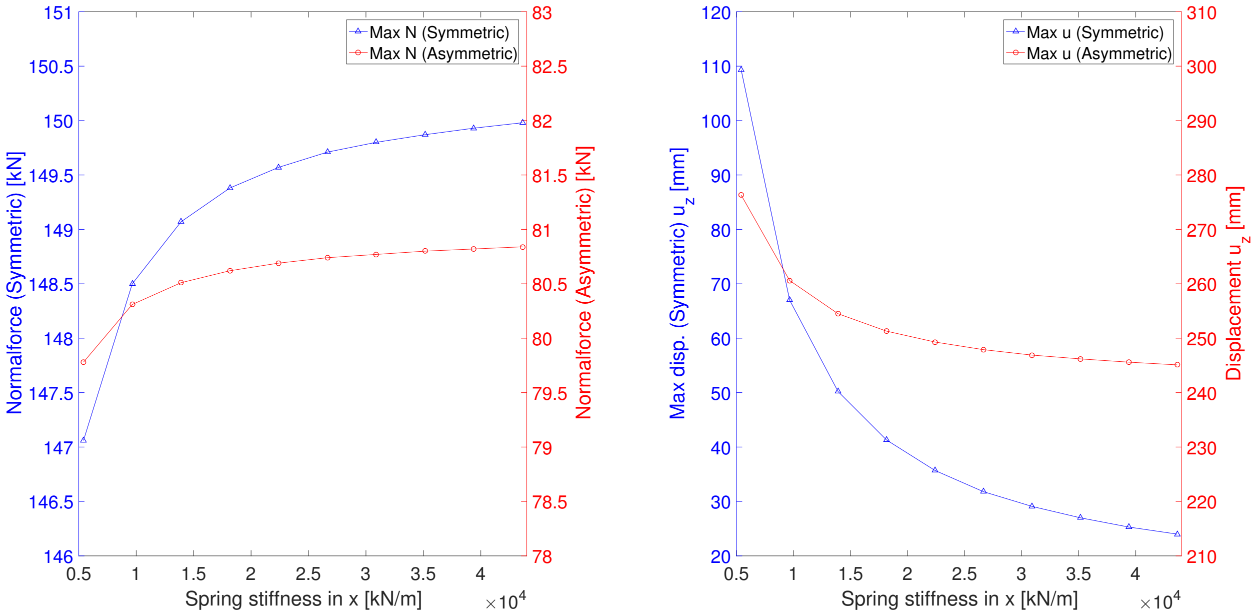

(a) Impact of support stiffness on normal force **(b)** Impact of support stiffness on disp.

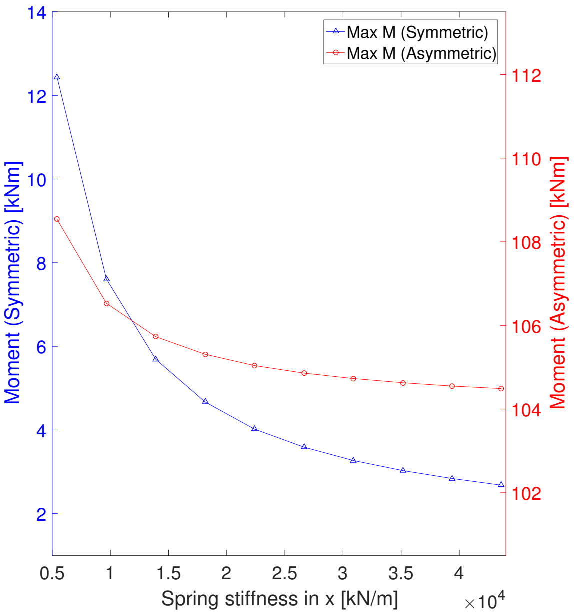

(c) Impact of support stiffness on moment

Figure 6.10: Parameter study of the support stiffness. Blue line = symmetric load, Red line = asymmetric load

From fig. 6.10a it can be seen that normal force decreases with a lower support stiffness. The effect is however small as using the normal force at the low stiffness result in a relative difference of ≈ 1-2 % between the lower and higher normal force (for both the symmstric and assymetric case). It can also be seen that this effect was more noticeable for the symmetric loading but can partly be explained with that the total load was double in the symmetric load case.

The displacement shown in fig. 6.10b, instead displays more correlation with the support stiffness, compared to the normal force. The dependence on support stiffens for displacement was larger for the symmetric load case but at the same time, the load was double in the symmetric case. To test the influence of this load difference, a special asymmetric load case with the same load as the symmetric case was also preformed. This test showed a similar dependence on the support stiffness compared too the asymmetric load case which meant that a symmetric load really have larger dependency with support stiffness independent of load. The result of this special load case followed the same behaviour as the other asymmetric load case and was therefore not shown here. The remaining difference in displacement is therefore believed to also depend on the deflection shape which can be seen in fig. 6.1 and fig. 6.2.

As a example of this the displacements at a low support stiffness can be compared with a totally stiff support. Using the displacements at the low stiffness boundary as reference, the relative difference between these displacements result in a 89 % difference (109.3 to 11,6 mm) for the symmetric case, compared with a 13 % difference (276,3 to 240,7 mm) for the asymmetric load case. Although the system is more affected by the support stiffness for the symmetric load case, the absolute values for the displacements was still larger for the asymmetric load case.

Similar to the displacement the moment seen fig. 6.10c decreases with increased support stiffness. Using the same method for calculating the relative difference the outcome is also similar, 90 % difference (12,44 to 1,26 kNm) for the symmetric case and 4 % difference (108,5 to 103,91 kNm) for the asymmetric load case. The correlation between the moment and displacement can be seen as an indication of that the stress ribbon system resist the displacements with a more beam like behaviour, when deflected from it's original cable like shape. In this way the local deflection is reduced and instead taken up as moment as discussed in section 2.2.

It can therefore be concluded that a low support stiffness doesn't influence the normal force but has more impact on the displacements and moment. Another conclusion that could be made from this test, was that the support stiffness affected the stress ribbon system more when the system was exposed to a symmetric load compared with an asymmetric load, even if the asymmetric loading lead to higher absolute values of displacement and bending moment.

6.3.2 Dependence of sag

In this test the support was assumed totally stiff and the sag f at the mid point of the span was varied from 2-11 m. With these conditions both theoretical (chapter 5) and FE analysis (chapter 6) could be used and the result is shown in fig. 6.11. The colours follow those in section 6.3.1 and the dashed lines show the analytical calculations according to chapter 5. In order to separate the calculation of natural frequency, that don't use the symmetric and antisymmetric load cases, different plot colours were used, see fig. 6.11d.

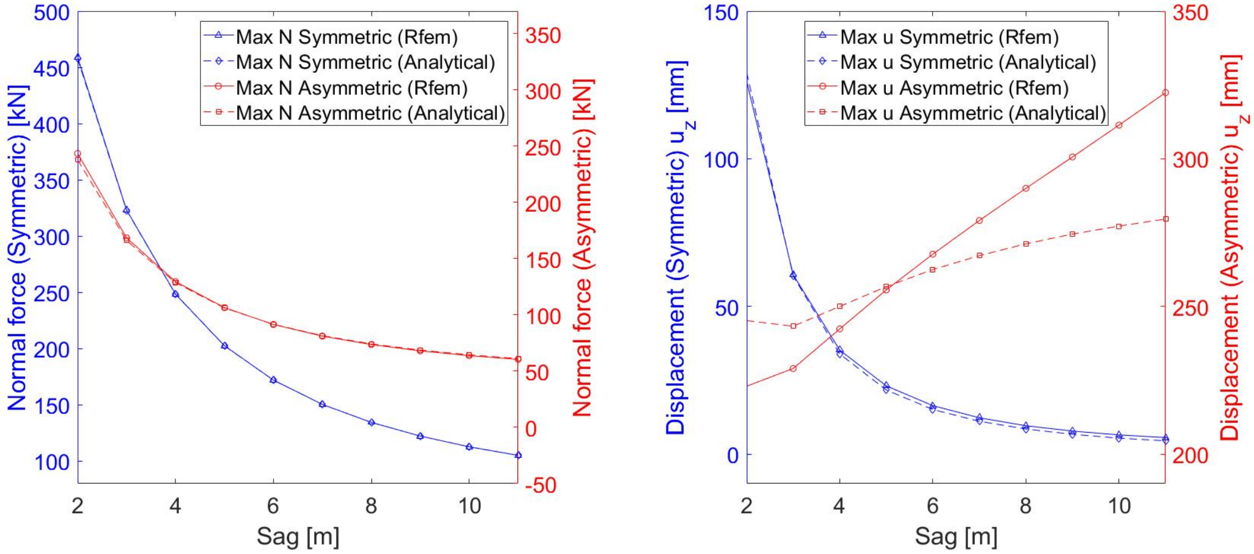

(a) Impact of sag on normal force

(b) Impact of sag on displacements

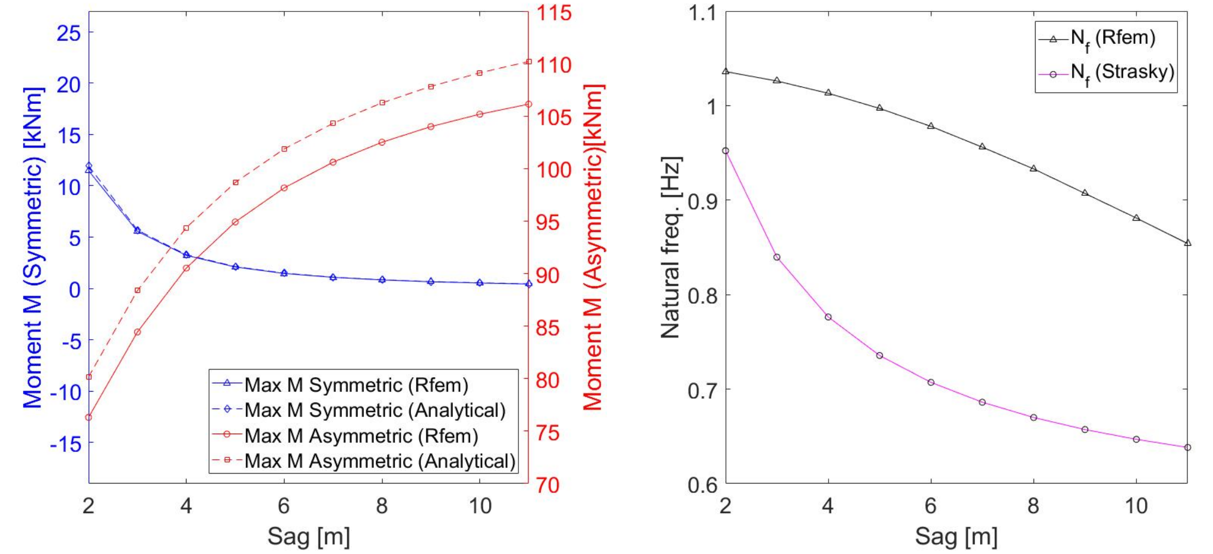

(c) Impact of sag on moment

(d) Impact of sag on natural frequency. Black- Rfem, Mageta- Strasky.

Figure 6.11: Parameter study of the sag. Blue line- symmetric load case, Red line- asymmetric load case. Solid line- Rfem, Dashed line- analytical solution.

Similar to the theory described in eq. (2.2) (Section 2.2) the relationship between normal force and sag is quadratic, as seen in fig. 6.11a. This means that it is beneficial for the normal force if the stress ribbon system has a large sag. It can also be interpreted as the normal force follows a cable like response. Both the symmetric and the asymmetric load case show this behaviour, hence the load type doesn't affect the correlation between the normal force and the sag. If the normal force calculated analytically respectively with Rfem were compared, it is evident that the different methods have very good agreement for both load cases.

The displacements also seem to follow the decreasing quadratic pattern as the normal force, when loaded with a symmetric load, seen in fig. 6.11b. The opposite relationship was however true for the asymmetric loading. It is for the asymmetric load case where the largest differences between analytical solution and Rfem can be observed. A part of this difference can be caused by the fact that third order theory was used in Rfem calculations while the analytical calculations were derived with first order theory.

The moment shown in fig. 6.11c again shows great similarity to the displacements. The interesting from this test was that the behaviour for the asymmetric load were the same for both the analytical solution and Rfem in contrast to what was the case for the displacements.

For the natural frequency shown in 6.11d, it is evident that increased sag means a lower natural frequency for the stress ribbon. As no real test of the natural frequency has been performed, both the displayed frequencies in 6.11d were considered quite uncertain.

The conclusion from this test was that the sag had influence on all the tested parameters in the system. For the normal force and natural frequency an increased sag was beneficial for normal force while the opposite was true for displacements, bending moment and natural frequency. This means that a good balance in sag is required that allows enough sag to lower the normal forces but at the same not to much sag which would lead to large deflections.

6.3.3 Dependence of slenderness ratio I/A

The last parameter that was studied was the slenderness of the cross-section. This was described with the slenderness ratio $\boldsymbol{I/A}$, which is described in section 6.2.5 and the result from this analysis can be seen in fig. 6.12. As cross-section in the middle of the interval ($\frac{I}{A} = 600\text{m}^2$) was used as reference, this point is the same regardless of varied parameter.

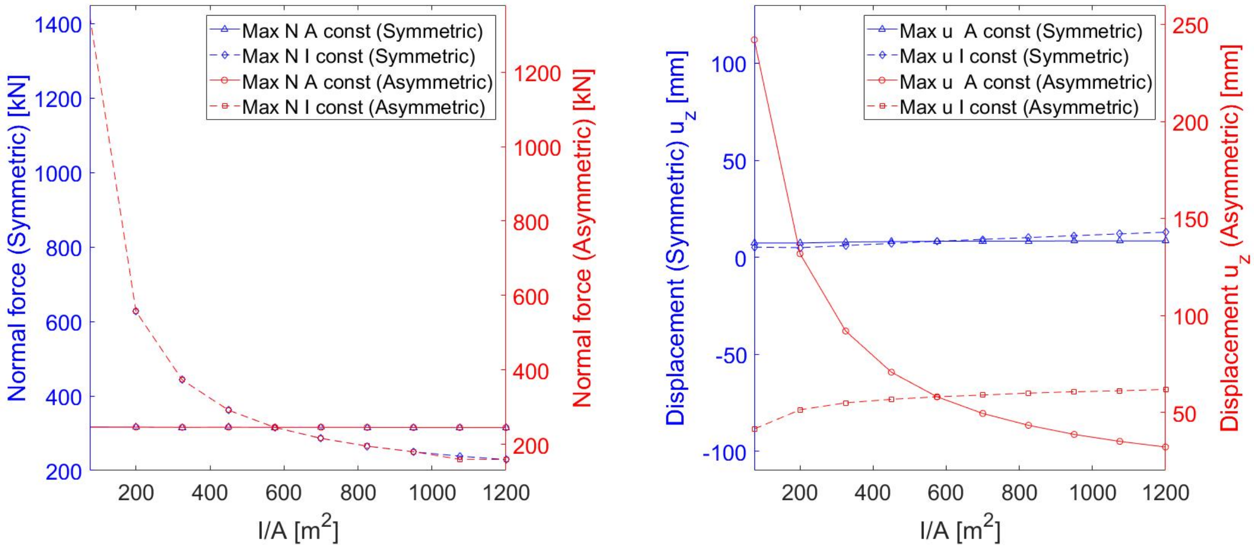

(a) Impact of slenderness on the normal force **(b)** Impact of slenderness on the disp.

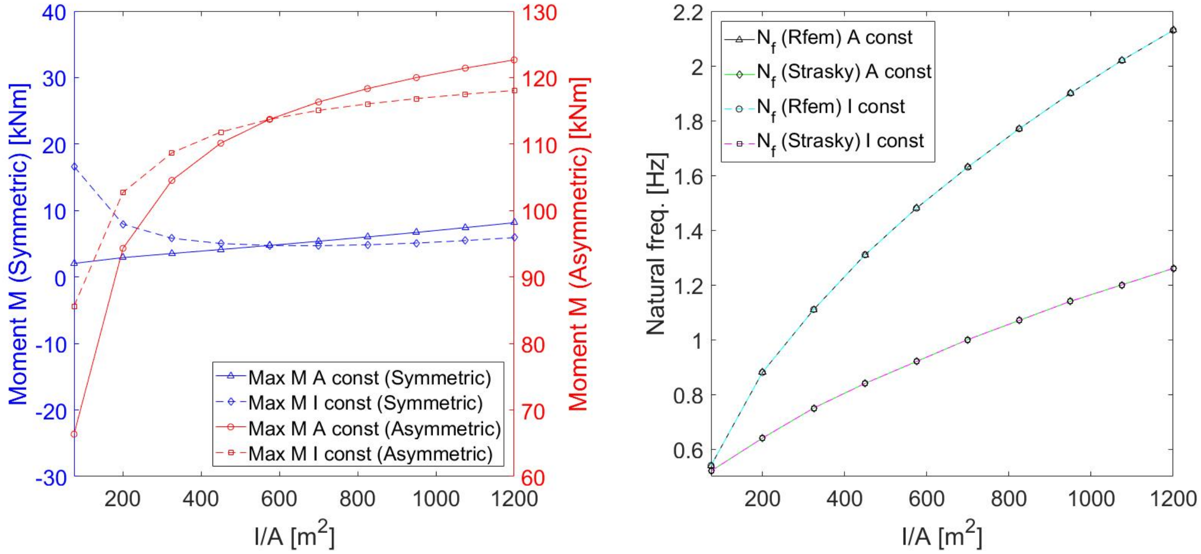

(c) Impact of slenderness on the moment **(d)** Impact of slenderness on the natural frequency

Figure 6.12: Impact of the cross-sections slenderness. The line explanation follow those in section 6.3.2

In fig. 6.12a, it can be seen that the largest variation in normal force was in the test when bending stiffness I was kept constant. This is due to the difference in self weight as this test starts with a large cross-section area that decreases with increased slenderness (explained in section 6.2.5).

For the displacement plot shown in Figure 6.12b it was again primarily the asymmetric load that caused the largest displacements. From this graph it was clear that the displacement decreases rapidly with a linear increase of bending stiffness. The difference between the displacement for the most stocky and the most slender beam was 210 mm (242 to 32 mm) for the asymmetric load and beam with constant area, while the corresponding difference for the test with constant bending stiffness was -21 mm (41 to 62 mm) with the decrement of material use by approximately 94 %.

Unlike the other two tests (influence of support stiffness and sag) the correlation that more displacement leads to more moment in the stress ribbon was no longer valid. Instead fig. 6.12c shows that more moment develops in a more slender beam but it should be noted that the moment capacity increases faster than the moment. The difference between the most stocky and the most slender beam was -32,5 kNm (85,6 to 118,1 kNm) for the asymmetric load and test with constant area and the corresponding for the beam with constant bending stiffness was -56,3 kNm (66,4 to 122,7 kNm).

From fig. 6.12d it can be seen that the natural frequency increases with increasing slenderness of the cross-section. Both the test with constant area and constant bending stiffness overlap. This is thought to occur due to two effects cancelling out each other; First is that the cross-section with lager self weight has higher mass per unit length that lowers a cables natural frequency, at the same time the weight creates higher prestress which increases the natural frequency, in the end creating the independence of the cables self weight. This result is believed to be a bit unrealistic as e.g. deformations at support for cross-sections with large self weight would in reality give the SR system a lower stiffness.

To give an idea of how the slenderness affects the forces and moments in the SR member, a reference beam of GL32h 300x300 was assumed. Then the material was redistributed to give a high respectively low beam cross-section and the result of these calculations is shown in table 6.2, where U denotes utilization ratio.

Table 6.2: Example of forces in specific cross sections (U-utilization ratio)

Symmetric load Cross-section	N [kN]	U N %	u [mm]	M [kNm]	U M %	U Tot %
GL32h 300x300	193	15	19	0.5	0.5	15,5
GL32h 200x450	193	15	20	0.9	0.6	15,5
GL32h 450x200	193	15	18	0.3	0.5	15,4
Asymmetric load Cross-section	N	U N %	u	M	U M %	U Tot %
GL32h 300x300	126	10	604	43.7	47	57
GL32h 200x450	126	10	435	68.9	50	60
GL32h 450x200	126	10	724	23.5	38	48

Calculations were made with same conditions as other parameter studies see section 6.2 for more info

From table 6.2 it can be seen that the asymmetric load results in the most unfavourable parameters and that the high beam had a higher utilisation ratio. At the same time it was only the high beam that had low enough displacement. Evident in asymmetric load case was also that it was primarily the moment with the given conditions that was governing the degree of utilization. The conclusion was therefore that there must be a balance between beam height so that the hight is high enough to limit deflection but at the same time not too high as this would result in a large bending moment.

6.4 The influence of the order of theory

To investigate the influence of the order of theory, the same cross-section and load conditions as in the parameter study with stiffness and sag were assumed. Normal force, displacements and moment were then calculated with different order of theory in Rfem and are shown in table 6.3.

In table 6.3 it can be seen that most of the differences occur in the asymmetric load case where the displacements were lower in the higher order of theories. Interesting is that it was between first and second order theory where most differences could be observed, here the relative difference of 14 % could be seen for both the displacements and moment. This could be compared with the difference of 18 % for the displacements and 9 % for the moment between the analytical and third order FE calculation using the same conditions. From this comparison it can therefore be suspected that difference in result between the analytical and FE calculations in fig. 6.11 can partly is dependent on that the analytical solution uses first order theory while FE calculation uses third order theory.

Table 6.3: Example of impact of the degree of theory

Symmetric load Order of theory (OT)	N [kN]	u [mm]	M [kNm]
First OT(T1)	150.61	11.6	1.28
Second OT (T2)	150.4	11.6	1.26
Third OT (T3)	150.41	11.6	1.26
Diff. T1-T2	0.21	0	0.02
Diff. T2-T3	-0.01	0	0
Asymmetric load Order of theory (OT)	**N [kN]**	**u [mm]**	**M [kNm]**
First OT(T1)	80.51	293.6	122.98
Second OT (T2)	80.6	252.8	105.38
Third OT (T3)	80.99	240.7	103.91
Diff. T1-T2	-0.09	-40.7	17.6
Diff. T2-T3	-0.39	11.7	1.47

Calculations were made with same conditions as other parameter studies, see section 6.3 for more info.

6.5 Summary of info from parameter study that was implemented in preliminary design

- Impotence of support stiffness for both displacement and moment. This meant that the column design should be made as stiff as possible.
- Balance in sag, high enough to decrease normal force but at the same time not too high as it increases bending moments.
- Use a cross section that is slender enough to not attract to much bending moment but at the same time, stocky enough to prevent large displacements.

6.6 Description of preliminary design

In order to apply the information gathered from the parameter study about the structural workings of the stress ribbon concept, a preliminary design of the timber cable was made. The first change was to reduce the sag from L/10 to L/17.5 (sag of 4 m) which limited the deflection so that the deciding limitations in both characteristic SLS and design ULS became more similar.

All calculations were made in 2D to simplify calculations, and the material was chosen as GL 32 h. The load carrying SR members runs in the buildings width W according to fig. 6.13.

From fig. 6.13 it is also possible to explain the position of the design loads. For the snow load the design load was in a section at $\mathrm{h}_{\mathrm{high}}$ (see section 4.1), similarly the design asymmetric wind was in a section at $\mathrm{h}_{\mathrm{high}}$, while the largest negative wind pressure was in a section at D_{m} (middle of the buildings depth direction, see section 3.4.2). The span W and the depth D of the building was set with the same proportion as the scale test with snow drift and with a span of 70m the depth of the building was 140 m. The highest point of the building was set to $h_{high} = 16$ m which with a 5 % roof slope would result in $h_{low} = 9$ m.

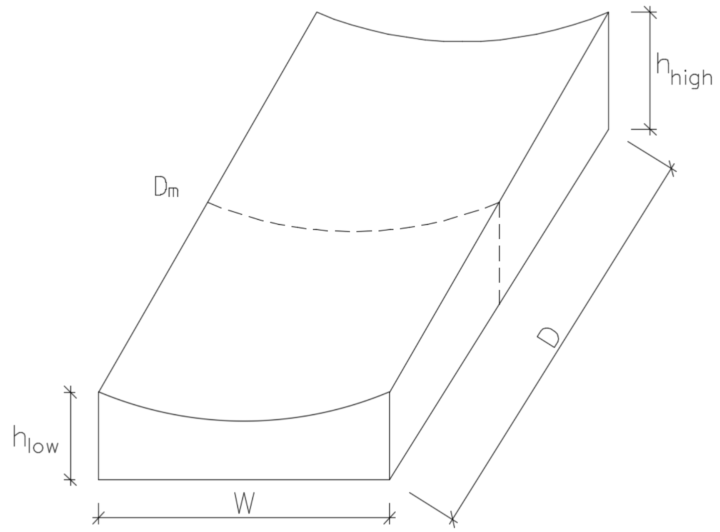

Figure 6.13: Sketch of the designed building

6.6.1 Characteristic loads

The self weight of the structure was approximately 0,72 kN/m^2 and the added weight of the green roof were set to 1,25 kN/m^2 which corresponds to a sedum roof with a thickness of $\approx$ 100 mm (*Svenska Naturtak* 2017).

For the characteristic wind load a roof height of 16 m, reference wind speed of 25 m/s and terrain with low vegetation was assumed. This results in a characteristic wind pressure of $q_p = 0.96$ kN/m^2.

The characteristic snow load was assumed to 2 kN/m^2. This means that the building can be build in quite windy environment and can take a snow load that is approximately south of Stockholm.

After testing of different load cases, four load cases could be identified to be deciding for design, see fig. 6.14. Here the self weight of the structure and weight of the green roof was noted with E$_g$, while the snow- and wind load were noted with S$_k$ and C$_{pe,10}$ respectively.

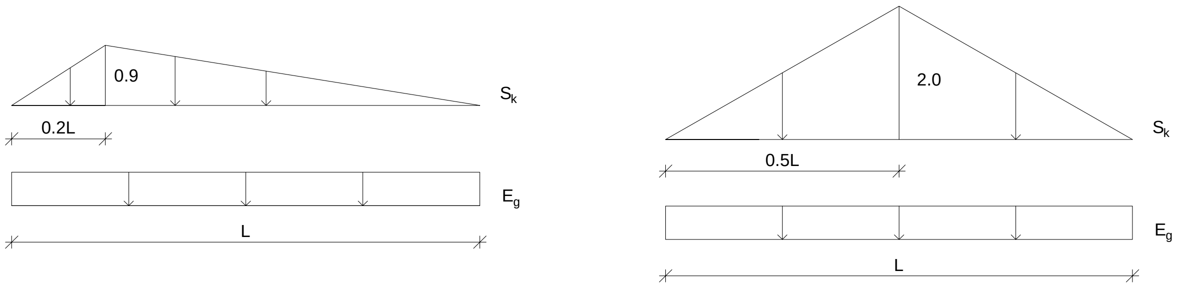

(a) Load case 1: Asymmetric snow load (measurement, see section 4.3.3)

(b) Load case 2: Exceptional snow drift (EN 1991)

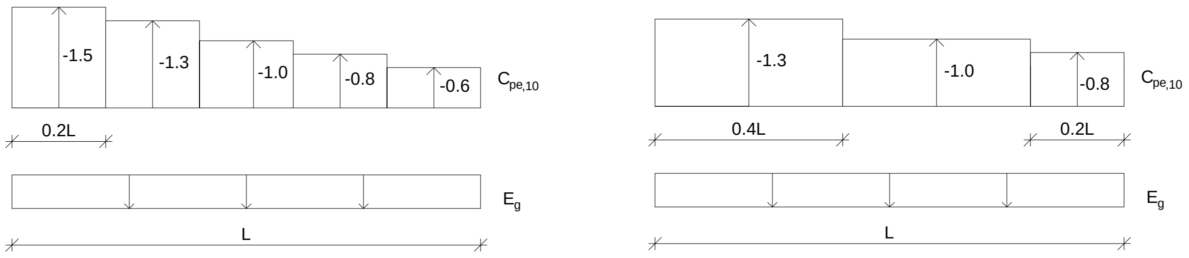

(c) Load case 3: Asymmetric wind load (measurement, see section 4.3.3)

(d) Load case 4: Maximum wind suction (measurement, see section 4.3.3)

Figure 6.14: Deciding load cases for design

Load case 1

The worst case for uneven snow loading was the asymmetric load case fig. 6.14a and was calculated according to section 4.3.3. This load case primarily gave problems with deflections.

Load case 2

Biggest total load who determined by the exceptional snow drift from Eurocode see fig. 6.14b. This load case resulted in the highest normal force and with spring support also gave considerable deformations.

Load case 3

The largest asymmetric load case for wind was determined according to and corresponds to a section close to the roofs corners (wind $\theta = 0$), see section 3.4.2. This load gave problems with deflections as well as large bending moments.

Load case 4

The final design load case can be seen in fig. 6.14d and was quite similar to load case 3 also originates from section 3.4.2 (wind $\theta = 0$). This load case corresponds to a section in the middle of the building and results in the least tension in the stress ribbon and the main reason why the "green roof" was implemented, as this extra weight resulted in a timber cable always loaded in tension.

When designing the cross-section the worst load case for both the normal force and moment in ULS was determined. The result was that the symmetric load case for exceptional snowdrift according to load case 2 presented the largest normal forces while the asymmetric wind in load case 3 gave the largest bending moment. Using these two load cases it was possible to find a cross-section where both the normal- and moment capacity were utilized efficiently. In order to be on the safe side the capacity utilization limit was set to a maximum of 90 %, in combination with neglecting the capacity in the plywood.

6.6.2 Calculations used in the preliminary design

The cross-section of the SR member consists of both plywood and glulam beams which both contribute to an increased moment of inertia which was used to limit the deflections in the characteristic SLS. There were, however, uncertainties about the force distribution in the ULS and therefore only the capacity in the beam was considered as a conservative approach (plywood neglected) which also explains the high limits for utilization mentioned above.

Bending moment capacity in SR member

As only the beams capacity was utilized the SR members section modulus could be calculated as:

$$W_y = \frac{wh^2}{6} \tag{6.5}$$

Where:

w	section width
h	section height

Using Equation (6.5) with a cross-section of 250x300 mm results in W_y=3750 cm^3

The material strength was calculated as:

$$f_d = \frac{k_{mod} \cdot f_k}{\gamma_M} \tag{6.6}$$

Where:

f_k	Characteristic material strength
k_{mod}	Modification factor which takes the influence of moisture and load duration into consideration
γ_M	Partial coefficient for the material

As GL 32 h was used, the characteristic bending strength parallel to grain f_{mk} was 32 MPa (EN 1194), k_{mod} was set to 0,8 as snow can be considered a load with a medium duration and γ_M was set to 1.25 (CEN, 2004).

With the parameters listed above the design bending strength was determined to f_{md}=20.48MPa.

The design bending moment capacity could then be calculated as:

$$M_{Rd} = f_{md} W_y k_{crit} \tag{6.7}$$

Where:

W	Is the section modulus
k_{crit}	Reduction factor which considers the risk for lateral torsional buckling

As all load cases resulted in tension forces, the whole beams capacity could therefore be utilized i.e. $k_{crit} = 1$.

This meant a moment capacity of $M_{Rd} = 76.8$ kNm for the cross-section.

Normal force capacity in SR member

The calculation of the material strength follows those in eq. (6.6), but with the characteristic tension capacity of f_{tk} = 22.5 MPa (parallel to grain). This gave design tensile strength of f_{td} =14.4 MPa.

The tensile normal force capacity could then be calculated as:

$$N_{t,Rd} = f_{td}A \tag{6.8}$$

This gave a tensile capacity of $N_{t,Rd}$=1080 kN.

6.6.3 Bending and normal force

In all load cases there was both bending moment and normal force involved. To calculate the material utilization for this case the following equation was used:

$$\frac{M_{Ed}}{M_{Rd}} + \frac{N_{t,Ed}}{N_{t,Rd}} \leq 1$$

6.6.4 Load combinations and partial coefficients

ULS

For ULS calculations the load combination STR-B according to SS-EN 1990 and with only one variable load considered at a time the equation can be written as:

$$\gamma_d 1.2 G_{kj,sup} + \gamma_d 1.5 Q_{k,1} \qquad \text{(unfavourable permanent load)} \tag{6.9}$$

Or

$$\gamma_d 1.0 G_{kj,inf} + \gamma_d 1.5 Q_{k,1} \qquad \text{(favourable permanent load)} \tag{6.10}$$

where:

γ_d	Is the partial coefficient for safety class
$G_{kj,sup}$	Unfavourable permanent load
$G_{kj,inf}$	Favourable permanent load
$Q_{k,1}$	Main variable load

A failure in the SR members was considered to result in a high risk for severe personal injuries and the safety class was therefore set to γ_d = 1.0.

SLS

For the deflections the characteristic SLS was used according to SS-EN 1990:

$$1.0G_{k,j} + 1.0Q_{k,1} \tag{6.11}$$

Where:

$G_{k,j}$	Permanent load
$Q_{k,1}$	Main variable load

6.6.5 Safety factors in different loads

As the design loads used are from different sources they have different levels of safety margin. Using loads from Eurocode is considered to be on the safe side while using loads from direct measurement contains more uncertainty. This leads to that load case with asymmetric snow load is considered more uncertain. As the wind loads presented have implemented safety factors to measurement, they can also be considered to contain sufficient safety.

6.7 Preliminary design of stress ribbon element

From the preliminary design a cross-section of the load carrying stress ribbon according to 6.15 was determined.

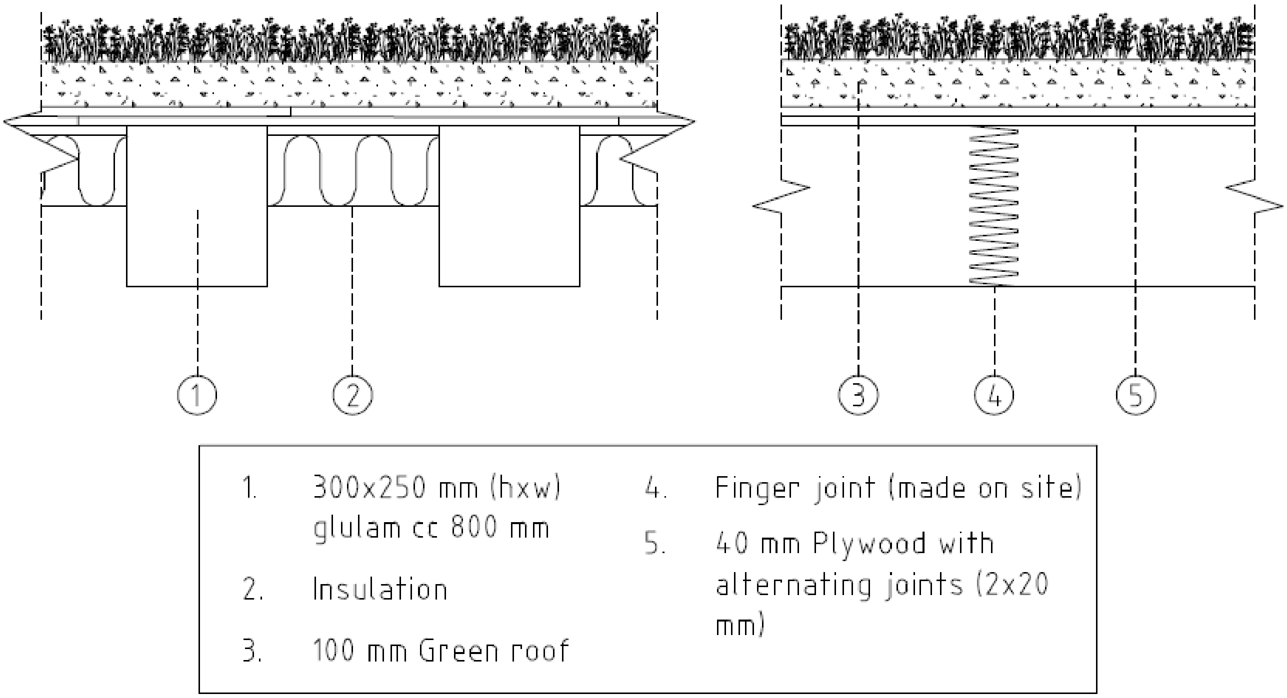

Figure 6.15: Cross-section of the preliminary design

With the cross-section seen in fig. 6.15, a utilization of 90 % was calculated for the glulam beam with the exceptional snow drift load (load case 2), while the corresponding utilization for the asymmetric wind load (load case 4) was 86 %. The maximum displacement in characteristic SLS for this cross-section was 323 mm for load case 2 while the minimum displacement was -317 mm upwards for load case 3. These displacements occur far away from the supports which avoids damage on the buildings secondary structure and is also considered to be sufficiently small to be perceived as safe. With these two arguments the calculated deflection is therefore deemed as acceptable. As described in sections 2.3 and 6.6, the green roof serves multiple purposes; to provide weight for stability, reducing deflection and bending moment for wind uplift as well as delaying water run-off. The drawbacks with this design, it add more load for the the symmetric load and requires a perfectly tight moisture barrier.

With a load carrying cross-section with a height of just 340 mm for a span of 70 m this shows that the stress ribbon system could be designed very slender compared with truss or arc alternative. It should although be kept in mind that some effects might have been overlooked e.g. that every stress ribbon element would not be connected to a column, causing the real stiffness to be lower than the one used in the analysis. As an decreased support stiffness according to the parameter study leads to both increased displacements and moment it is a important parameter to consider when designing this type of structure.

When the modes of the natural frequency of the stress ribbon element were compared with the reference building A it can be be concluded that the shape of the two first modes were the same. As discussed in section 2.3.4 it was primarily the asymmetrical mode shape with the lowest frequency that was exited from dynamic wind loads and here the reference building has an eigenfrequency of 0,6544 Hz while the chosen cross-section had a frequency of ≈ 1.1 Hz. It can also be compared with the suspension bridges Vranov Lake bridge and Willamette River bridge which also had a first asymmetric mode shape, with an eigenfrequencies of 0.298 Hz and 0.541 Hz respectively. If an increased natural frequency is desired the sag and the slenderness can be increased according to the parameter study e.g. a cross-section with GL 32h 200x400 and with a sag of 3.5 m results in a natural frequency of ≈ 1.2 Hz even if this section has a slightly higher normal force utilization.

Chapter 7

Discussion and Conclusions

7.1 Discussion

In his theses the main focus have been to get a deeper understanding of using a SR design. In order to achieve this the following steps were made; Literature study, laboratory experiments, analytical calculation model, FEM model and finally a preliminary design.

From the literature studies theory the complexity of aerodynamic experiments was understood. Ideas of wind tunnel test for aerodynamic scale experiments was therefore replaced with a rigid building model. With scale models the redistribution of snow on a saddle shaped roof could be studied and compared with the current design code. In this way the design code worked as a control for laboratory tests and also served as a interesting comparison between theory and reality. The laboratory test was also useful to determine the asymmetric design load that was later used in the preliminary design of the SR building.

The analytical calculations and FE calculations were similarly to the design code and experiments compared in order to achieve more reliable results. The analytical calculation was for instance used too calibrate the FE model after a trusted reference example. Then the advantage of FE being more general could be used by analysing the affect of different conditions such as support stiffness, sag and slenderness for the SR structure. With this information a good balance between different parameters could be implemented and a preliminary design could finally be made to the potential slenderness in the load carrying system can be made with the SR principle.

7.2 Conclusion

The loads that were used in design of this structure have all been collected from different sources (Eurocode, Rizzo's research and own measurements) and contains different safety margins. Both Eurocode and Rizzo's research aims to be used in design these can be considered to be more conservative. While the result of the preformed laboratory measurements, with no considerations to safety factors other then using a starting sand depth corresponding to a Eurocode snow depth, can be considered to contain more uncertainties. This explains why the conservative loads from Eurocode and Rizzo's research was used for all the design loads except for asymmetric snow load were the result from the laboratory measurements was used instead as this type of load situation was not found elsewhere. From the loads the snow load for exceptional snowdrift resulted in the worst symmetric load while the uneven wind load gave the most asymmetric load case. For the symmetric load the normal force was the most influential for capacity utilization while the asymmetric load was decisive for development of deflection and bending moment.

For wind instability, vortex shedding is the only instability that is of concern. The risk telhogh considered to be low as the building used for preliminary design has a high eigenfrequency and a low roof height compared with reference structures that is considered safe against dynamic excitation.

Support stiffness had biggest impact on the displacements and the bending moment, especially for the symmetric load case. When the sag of the structure was varied it could be seen that all studied internal forces (N,M,disp and natrual frequency) was affected . Lower sag meant increasing normal forces and natural frequencies for the structure while the opposite was true for displacements and bending moments. In both parameter studies of support stiffness and sag, more bending stiffness corresponds to an increased bending moment. In the test with increased slenderness the opposite relation between displacement and bending moment was true, as a slender cross-section meant an increase of bending stiffness.

The structure was designed against static loads and optimized so the normal force- and bending moment capacity is utilized effectively. The resulting cross-section for a 70 m span was a 250 x 300 mm^2 glulam beam cc 800 mm with a double layer of plywood. This was possible by increasing the self weight of the roof with the use of a green roof which improved conditions for wind uplift forces and also resulted in a higher natural frequency.

Suggestions for further studies

In the scale experiment a lot of factors were assumed in order to get a feeling of the potential snow drift on a catenary roof. Factors such as roof slope, surface roughness, surrounding topography that all have an influence on the snow drift were assumed (CEN, 2003). Those parameters would require their own study in order to determine their individual importance and to determine susceptible values for a perfectly realistic scale model.

A lot of details such as design of connections, horizontal stabilization and time dependency for force distribution has still not been studied. In combination with building cost these are only a few of the parts that would be necessary to solve before the structure could be built.

Chapter 8

Appendix

8.1 Determining modeling material for snow

8.1.1 Particle transport

As another material was used for simulation of snowdrift it is important to have a similarity in partical transport between the materials. The transport of particles can be divided into three different ways: creep, saltation and suspension (Elorza and Benito, 2005). The transport method depends mainly on the grain size of the available particles and the transport is illustrated in fig. 8.1.

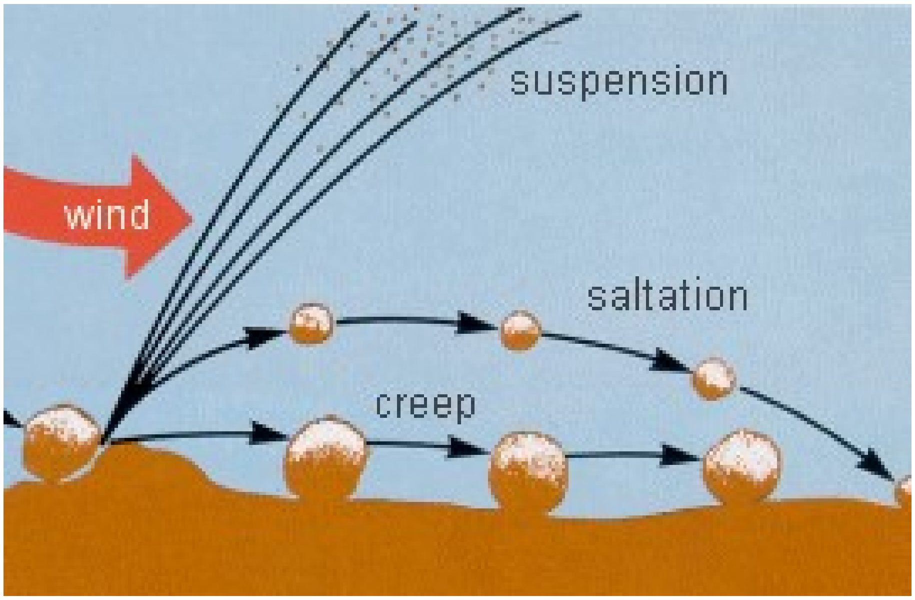

Figure 8.1: Description of the different particle transport
Source: Wikipedia, (2017)

For snow drift it is saltation that is the most influential in the partial transport (Zhou et al., 2014). Saltation involves a bigger uplift of particles that travel downwind in a ballistic trajectory. Smaller particles obtain a higher velocity and can therefore have a longer saltation distance. When the particles hit the surface, the impact energy can lift or transport other particles as mentioned before.

8.1.2 Similarity between different materials

To determine what material has the best similarity with snow, three different materials were studied by ibid., and can be seen tables 8.1 and 8.2.

Table 8.1: Physical properties of snow and simulated particles (Zhou et al., 2014)

	Snow	Silica sand	Polyfoam	Sawn wood ash
Diameter d_p(mm)	0.15	0.2	0.4	0.5
Density ρ_p (kgm^{-3})	50 - 700	2784	1223	297
Threshhold velocity at 1.0 m u_t (ms$^-$1)	3.25 - 7.81	7.16	4.77	3.25
Threshhold friction velocity at 1.0 m u_{*t} (ms$^-$1)	0.15 - 0.36	0.33	0.22	0.15
Angle of repose θ (°)	50	34	21	43
Setting velocity ω_f (ms$^-$1)	0.2 - 0.5	0.6	0.5	0.2

Where parameters follow:

g	Acceleration of gravity [m/s^2]
H	Characteristic height [m]
ρ	Air density [kg/m^3]

Table 8.2: Similarity parameters of snow and simulated particles (see table 8.3 for more info)(Zhou et al., 2014)

Eq. no.	Similarity parameter	Snow	Silica sand	Polyfoam	Saw wood ash
Eq. (1)	$u_{*t}^3/2g\nu > 30$	-	126.5	37.5	11.9
Eq. (4)	$\frac{\rho u_*^2}{\rho_p H g}$	0.37 - 5-16e-5	9.62e-5	8.88e-5	18.7e-5
Eq. (7)	$\frac{\rho}{(\rho_p - \rho)} \frac{u_*^2}{g d_p}$	0.020 - 2.214	0.024	0.012	0.020
Eq. (10)	$\frac{u(H)}{u_{*t}}$	8.4 - 20.2	25.2	24.1	25.2
Eq. (11)	$\rho_p/\rho \geq 600$	-	2272.7	998.4	242.5
Eq. (12)	$\frac{\rho_p}{\rho_p - \rho} \frac{u^2(H)}{gH}$	1.04 - 1.06	58.8	23.8	12.2
Eq. (13)	$\frac{\omega_f}{u(H)}$	0.07 - 0.17	0.07	0.09	0.05
Eq. (16)	$\frac{\rho}{\rho_p} \frac{u(H)T}{H}$	-	21.9	23.8	23.4

Where parameters follow table 8.1 and:

g	Acceleration of gravity [m/s^2]
H	Characteristic height [m]
ρ	Air density [kg/m^3]

The Similarity equations describe:

Table 8.3: Description of equations in table 8.2

Eq. no.	Description
Eq. (1)	Reynolds number of aerodynamic roughness height
Eq. (4)	Aerodynamic roughness height caused by salting particles
Eq. (7)	Ejection process of particles (Densimetic Froude number)
Eq. (10)	Relationship between wind velocity and the physical threshold property
Eq. (11)	Density ratio between particle and air
Eq. (12)	Particle trajectory (another form of densimetric Froude number)
Eq. (13)	Equation for maintaining ratio of drag force to inertial force
Eq. (16)	Dimensionless time coefficient in order to get the same accumulation volume of particles

From tables 8.2 and 8.3 it can be seen that similarity Eq. (1), which maintains the fully rough flow of the snow particles, was sufficient for silica sand and polyfoam but not for saw wood ash. But as the simulating uses a model with distinct flow separation, no strict similarity in Eq. (1) is required according to (Zhou et al., 2014).

Another similarity condition that can be relaxed is the densimetric Froude number Eq. (12), this condition is actually not fulfilled by any of the three materials. But according to Zhou et al., (ibid.) studies have shown that desimetric Froude number of 20 times the reference particle, still displayed same snowdrifting patterns as field result, meaning that similarity condition Eq. (12) can also be relaxed.

To summarize the similarity study of Zhou et al., (ibid.) and tables 8.1 and 8.3, the silica sand achieved the closest result in both field observation as well as satisfying all similarity parameters except for Eq. (12). This indicates that high-density silica sand can accurately reflect the wind-induced redistribution of snow on a roof surface which is also in agreement with Kind, (1986).

8.2 MATLAB CODE

The implantation of analytical equations in to MATLAB

8.2.1 Analytical calculations

```
format compact
close all
clear all
clc

global g EA EI f l q H x
%Globala varden
g=1e-6; %N/m
EA=1.66E+09; % N
EI=5.07E+07; %Nm^2
f=6;%5; %m
l=70;%50; %m
q=1.6e3; %kN/m
H=g*l^2/(8*f); %kN
n=1e3;
x=linspace(-l/2,l/2,n);
x2=linspace(0,l,n);

%Symmetric load ...
    case-----------------------------------------------------------------
fun_S=@(dH)((q-g*dH/H)/(2*(H+dH))*16*f*EA*[1/12-
1/(sqrt((H+dH)/EI)*l)^2+2*tanh(sqrt((H+dH)/EI)*l/2)
/(sqrt((H+dH)/EI)*l)^3]-dH);
```

```

%Solvning Symmetric load case
dH_S=fzero(fun_S,250e3);
%Displacement
w_S=(q-g*dH_S/H)/(2*(H+dH_S))*[l^2/4-
2/(sqrt((H+dH_S)/EI))^2+2*cosh(sqrt((H+dH_S)/EI)*x)/((H+dH_S)/EI*
cosh(sqrt((H+dH_S)/EI)*l/2))-x.^2];
Lambda_S=sqrt((H+dH_S)/EI);
% Moment
M_S=-EI*(q-g*dH_S/H)/(H+dH_S)*[sech(Lambda_S*l/2)*cosh(Lambda_S*x)-1];
Max_nyS=max(M_S)
% Normal force
dH_Stest=q*l^2/(8*f);
%dz_dxS2=(q+g)/(2*(H+dH_S))*(l-2*x2);
dz_dxS2=q/(2*dH_Stest)*(l-2*x2);
N_S=(H+dH_S)*sqrt(1+dz_dxS2.^2);
%Calculate max point
%Displacement
figure(1)
indexmax_S = find(max(w_S) == w_S);
w_Smax = w_S(max(abs(indexmax_S)));
xmax_S = x(max(abs(indexmax_S)));
strmax_S = ['Max(a) = ',num2str(round(w_Smax*1e3,1))];

%Approximativ solution of the Symmetric load case
%Displacement
dH_S2=(q/g)*H;
w_S2max=3*dH_S2*l^2/(16*f*EA);
w_S2=(-w_S2max/(l/2)^2)*x.^2+w_S2max;

strmax_S2 = ['Max(b) = ',num2str(round(w_S2max*1e3,1))];
%Moment
R_S=(l/4)^2/(2*w_S2max);
M_S2max=EI/R_S;
M_S2(1:n,1)=M_S2max;

%Printing of result
disp(' ')
disp('Symmetric loading give:')
disp(['dH = ' num2str(round(dH_S/1e3,1)) ' kN'])
disp(['H tot = ' num2str(round((dH_S+H)/1e3)) ' kN'])
disp(['Lambda  = ' num2str(round(Lambda_S,6)) ' m^-1'])
disp('Max displacement: ')
disp([strmax_S, ' mm'])
disp([strmax_S2, ' mm'])

%Displacement w
%axis ij %rever y-axis
%axis ji revers back
plot(x,w_S*1e3)
hold on
grid on
plot(x,w_S2*1e3)
title('Displacement w for Symmetric load case')
```

```
xlabel('length l [m]')
ylabel('Displacement [mm]')
legend('Exact solution (a)','Approximate solution (b)')

text(xmax_S,w_Smax*1e3,strmax_S,'HorizontalAlignment','right');
text(xmax_S,w_S2max*1e3,strmax_S2,'HorizontalAlignment','right');

figure(2)
plot(x,M_S*1e-3)
hold on
grid on
plot(x,M_S2*1e-3)

title('Moment for symmetric load')
xlabel('length l [m]')
ylabel('Moment [kNm]')
legend('Exact solution (a)','Approximate solution (b)')

figure(3)
plot(x2-l/2,N_S*1e-3)
grid on
title('Normal force for symmetric load')
xlabel('length l [m]')
ylabel('Normalforce [kN]')
legend('Cable type response')

%Antisymmetric load case ... ------------------------------------------------------------
fun_AS=@(dH)((q-2*g*dH/H)*f*EA/(H+dH)*[1/3
4/(sqrt((H+dH)/EI)*l)^2+8*tanh(sqrt((H+dH)/EI)*l/2)
/(sqrt((H+dH)/EI)*l)^3]-dH);

%Solvning Antisymmetric load case
dH_AS=fzero(fun_AS,125e3);
Lambda_AS=sqrt((H+dH_AS)/EI);

c1=((q-g*dH_AS/H)*(l^2/8-2/Lambda_AS^2)-l^2/8*g*dH_AS/H)/(2*(H+dH_AS));
c2=-q*l/(8*(H+dH_AS)); c6=c2;
c3=(q*[cosh(Lambda_AS*l/2)+1]-2*g*dH_AS/H)/(2*
(H+dH_AS)*Lambda_AS^2*cosh(Lambda_AS*l/2));
c4=q*[cosh(Lambda_AS*l/2)-1]/(2*(H+dH_AS)*Lambda_AS^2*sinh(Lambda_AS*l/2));
c8=c4;
c5=((q-2*g*dH_AS/H)*l^2/8+2/Lambda_AS^2*g*dH_AS/H)/(2*(H+dH_AS));
c7=(-q*[cosh(Lambda_AS*l/2)-1]-2*g*dH_AS/H)/(2*
(H+dH_AS)*Lambda_AS^2*cosh(Lambda_AS*l/2));

c3m=(1/Lambda_AS^2)*((q-g*dH_AS/H)/(H+dH_AS));
c4m=(1/(Lambda_AS^2*sinh(Lambda_AS*(-l/2))))*((q-g*dH_AS/H)/(H+dH_AS)-
c3m*Lambda_AS^2*cosh(Lambda_AS*(-l/2)));

c7m=(1/Lambda_AS^2)*((-g*dH_AS/H)/(H+dH_AS));
c8m=(1/(Lambda_AS^2*sinh(Lambda_AS*(l/2))))*((-g*dH_AS/H)/(H+dH_AS)-
c7m*Lambda_AS^2*cosh(Lambda_AS*(l/2)));
%z_pl=(1/dH_AS)*(q/2)*(2*x(i)-3*l/4)+(1/H)*(g/2)*(2*x(i)-l);
```

```

w_AS=zeros(1,n);
M_AS=zeros(1,n);
N_AS=zeros(1,n);

for i=1:n
    if x(i)<=0
        w_AS(i)=c1+c2*x(i)+c3*cosh(Lambda_AS*x(i))+
        c4*sinh(Lambda_AS*x(i))-
        (q-g*dH_AS/H)/(2*(H+dH_AS))*x(i)^2; % -l/2<x<=0
        M_AS(i)=-EI*(c3m*Lambda_AS^2*cosh(Lambda_AS*x(i))+
        c4m*Lambda_AS^2*sinh(Lambda_AS*x(i))-(q-g*dH_AS/H)/(H+dH_AS));
        N_AS(i)=dH_AS*sqrt(1+((1/dH_AS)*(q/2)*(2*x2(i)-3*l/4))^2);%+
        H*sqrt(1+((1/H)*(g/2)*(2*x2(i)-l))^2);
    else
        w_AS(i)=c5+c6*x(i)+c7*cosh(Lambda_AS*x(i))+c8*sinh(Lambda_AS*x(i))+
        g*dH_AS/H/(2*(H+dH_AS))*x(i)^2; %0<x<l/2
        M_AS(i)=-EI*(c7m*Lambda_AS^2*cosh(Lambda_AS*x(i))+c8m*Lambda_AS^2*
        sinh(Lambda_AS*x(i))+(g*dH_AS/H)/(H+dH_AS));
        N_AS(i)=dH_AS*sqrt(1+((1/dH_AS)*(q*l)/8)^2);%+
        H*sqrt(1+((1/H)*(g/2)*(2*x2(i)-l))^2);
    end
end
Max_nyAS=max(M_AS)
%Calculate max and min points
indexmin_AS = find(min(w_AS) == w_AS);
w_ASmin = w_AS(indexmin_AS);
xmin_AS = x(indexmin_AS);
strmin_ASw = ['Min(a) = ',num2str(round(w_ASmin*1e3,1))];

indexmax_AS = find(max(w_AS) == w_AS);
w_ASmax = w_AS(indexmax_AS);
xmax_AS = x(indexmax_AS);
strmax_ASw = ['Max(a) = ',num2str(round(w_ASmax*1e3,1))];

%Approximativ solution for Antisymmetric load case
dH_AS2=(q/g)*H/2;
w_AS2max=q*l^2/(64*(H+dH_AS2));
w_AS2=zeros(1,n);

%Moment
R_AS=(l/4)^2/(2*w_AS2max);
M_AS2max=EI/R_AS;
M_AS2=zeros(1,n);

strmin_AS2w = ['Min(b) = ',num2str(round(-w_AS2max*1e3,1))];
strmax_AS2w = ['Max(b) = ',num2str(round(w_AS2max*1e3,1))];
for i=1:n
    if x(i)<0
        w_AS2(i)=(-w_AS2max/(l/4)^2)*(x(i)+l/4)^2+w_AS2max;
        M_AS2(i)=M_AS2max;
    elseif x(i)>0
        w_AS2(i)=(w_AS2max/(l/4)^2)*(x(i)-l/4)^2-w_AS2max;
        M_AS2(i)=-M_AS2max;
```

```
    end
end

%Printing of result
disp('Antisymmetric loading give:')
disp(['dH = ' num2str(round(dH_AS/1e3,1)) ' kN'])
disp(['H tot = ' num2str(round((dH_AS+H)/1e3)) ' kN'])
disp(['Lambda  = ' num2str(round(Lambda_AS,6)) ' m^-1'])
disp('Max displacement: ')
disp([strmax_ASw, ' mm'])
disp([strmax_AS2w, ' mm'])
disp('Min displacement: ')
disp([strmin_ASw, ' mm'])
disp([strmin_AS2w, ' mm'])
%Displacement w
figure(4)
axis ij %rever y-axis
%axis ji revers back
plot(x,w_AS*1e3)
hold on
grid on
plot(x,w_AS2*1e3)
title('Displacement w for Antisymmetric load case')
xlabel('length l [m]')
ylabel('Displacement [mm]')
legend('Exact solution (a)','Approximate solution (b)')
%Min and max points

text(xmin_AS,w_ASmin*1e3,strmin_ASw,'HorizontalAlignment','left');
text(xmax_AS,w_ASmax*1e3,strmax_ASw,'HorizontalAlignment','right');
text(xmin_AS,-w_AS2max*1e3,strmin_AS2w,'HorizontalAlignment','left');
text(xmax_AS,w_AS2max*1e3,strmax_AS2w,'HorizontalAlignment','right');

figure(5)
plot(x,M_AS*1e-3)
hold on
grid on
plot(x,M_AS2*1e-3)
title('Moment for antisymmetrical load')
xlabel('length l [m]')
ylabel('Moment [kNm]')
legend('Exact solution (a)','Approximate solution (b)')


figure(6)
plot(x2-l/2,N_AS*1e-3)
grid on
title('Normal force for antisymmetrical load')
xlabel('length l [m]')
ylabel('Normalforce [kN]')
legend('Cable type response')
%-----------------------------------------------------------------------
```

Bibliography

AWC (2007). *Beam design formulas with shear and moment diagrams. Design aid No. 6.* American Forest & Paper Association, Inc.

Ban, Shigeru, Shohei Motohashi, Arata Yoshida, and Haruji Tsubota (1998). “Nagano Olympic Memorial Arena: Design and Construction”. In: *IABSE REPORTS*, pp. 737–742.

CCE (2016). “Grandview Heights Aquatic Centre”. In: *Canadian Consulting Engineer*, pp. 22–23.

CEN (2003). *SS-EN 1991-1-3. Eurocode 1: Actions on structures – Part 1-3: General actions – Snow loads.* SIS Förlag AB. Stockholm.

– (2004). *SS-EN 1995-1-1. Eurocode 5: Design of timber structures – Part 1-1: General – Common rules and rules for buildings.* SIS Förlag AB. Stockholm.

– (2005). *SS-EN 1991-1-4. Eurocode 1: Actions on structures – Part 1-4: General actions – Wind actions.* SIS Förlag AB. Stockholm.

Chen, Wai-Fah and Eric M Lui (2005). *Handbook of structural engineering.* Crc Press. Chap. 26, p. 3.

Chopra, Anil K et al. (1995). *Dynamics of structures.* Vol. 3. Prentice Hall New Jersey. Chap. 2, p. 40.

Crawley, Stanley W and Robert M Dillon (1993). *Steel buildings: analysis and design.* John Wiley & Sons.

Crocetti, Roberto (2016a). “Cables”. Lecture on cables.

– (2016b). “Composite structures”. Theoretical lecture on concrete and steel composites.

– (2016c). “Large-Span Timber Structures”. In: *key-note paper, Proceedings of the World Congress on Civil, Structural, and Environmental Engineering (CSEE’16) Prague, Czech Republic.*

Elorza, Mateo Gutiérrez and Gerardo Benito (2005). *Climatic geomorphology.* Vol. 8. Elsevier.

Ghiocel, Dan and Dan Lungu (1972). *Wind, snow and temperature effects on structures based on probality.* Abracus press, p. 330.

Gonchar, Joann (2014). “Teaching an old material new tricks: three projects under construction in North America demonstrate that timber can be used as an alternative to concrete, steel, and even masonry.” In: *Architectural record* 202.7, p. 132. ISSN: 0003-858X. URL: `http://ludwig.lub.lu.se/login?url=http://search.ebscohost.com/login.aspx?direct=true&db=bvh&AN=716095&site=eds-live&scope=site`.

Han, Ki-Jang, Nam-Hyoung Lim, Man-Gi Ko, and Kee-Dong Kim (2016). “Efficient assumption of design variables for stress ribbon footbridges”. In: *KSCE Journal of Civil Engineering* 20.1, pp. 250–260.

Hermansson, Viktor and Jonas Holma (2015). “Analysis of suspended bridges for isolated communities”. Division of structural engineering. MA thesis. Faculty of Engineering LTH.

Hofverberg, Samuel (2016). “Long-span tensile timber roof structures”. MA thesis. Chalmers University of Technology.

Holmes, John D (2015). *Wind loading of structures.* 2nd ed. 3. CRC press, pp. 96–127, 210–221, 222–240.

Ivoryresearch.com (2017). *VORTEX INDUCED VIBRATION.* Image is not under copyright. URL: `http://www.ivoryresearch.com/writers/dave-oneil-ivory-research-writer/`.

Johansson, Marie and Helena Lidelöw (2015). *Dimensionering av träkonstruktioner. Projektering av träkonstruktioner.* Svenskt trä. Chap. 2-4, pp. 57–146.

Kalafatic, Ivan, Radic Jure, and Matko Medak (2006). “Preliminary design procedure for one span post-tensioned stress-ribbon bridge”. In: *DAAAM International Scientific Book*, pp. 313–329.

Kind, R.J. (1986). “Snowdrifting: A review of modelling methods”. In: *Cold Regions Science and Technology* 12.3, pp. 217–228. ISSN: 0165-232X. DOI: `http://dx.doi.org/10.1016/0165-232X(86)90036-4`. URL: `http://www.sciencedirect.com/science/article/pii/0165232X86900364`.

Ludescher, Guido, Frank Braun, and Uwe Bachmann (2007). “Stress-Ribbon Roof Structures of the New Stuttgart Trade Fair Exhibition Halls”. In: *Structural engineering international* 17.1, pp. 22–27.

Maclourin (2017). *M-WAVE.* File is licensed under the Creative Commons Attribution-Share Alike 3.0 Unported license. URL: `https://commons.wikimedia.org/wiki/File:M-wave_rink.JPG`.

Marti, Peter (2013). *Theory of structures: fundamentals, framed structures, plates and shells.* John Wiley & Sons.

McCutcheon, William J (1977). *Method for Predicting the Stiffness of Wood-Joist Floor Systems with Partial Composite Action.* Tech. rep. DTIC Document.

Mercier, Hugo et al. (2012). *Vibration problems in structures: practical guidelines.* Birkhäuser.

Norberg, Christoffer (2017). unpublished. Oral discussion.

Rizzo, Fabio, Piero D’asdia, and Massimiliano Lazzari (2009a). “Aerodynamic behaviour of hyperbolic paraboloid shaped roofs: wind tunnel tests”. In: EUROPEAN & AFRICAN CONFERENCES ON WIND ENGINEERING (EACWE).

Rizzo, Fabio, Piero D’Asdia, Francesco Ricciardelli, and Gianni Bartoli (2012a). “Characterisation of pressure coefficients on hyperbolic paraboloid roofs”. In: *Journal of Wind Engineering and Industrial Aerodynamics* 102, pp. 61–71. ISSN: 0167-6105. DOI: `http://dx.doi.org/10.1016/j.jweia.2012.01.003`. URL: `http://www.sciencedirect.com/science/article/pii/S0167610512000049`.

Rizzo, Fabio, Piero D’asdia, and Federica Speziale (2012b). “Aerodynamic behaviour of hyperbolic paraboloid roofs: comparison between piv tests and cfd simulations”. In: *The 2012 World Congress on Advances in Civil, Enviromental and Material Research (ACEM’ 12).* ACEM’ 12, pp. 3324–3454.

Rizzo, Fabio, D’Asdia, Piero, Lazzari, Massimiliano, and Giuseppe Olivato (2009b). “Aerodynamic behaviour of hyperbolic paraboloid shaped roofs: Pod and cfd analysis”. In: *5th*

European & African conference on wind engineering: Florence Italy, July 19th-23rd 2009: conference proceedings. Firenze University Press, pp. 1000–1004.

Runesson, Kenneth, Alf Samuelsson, and Nils-Erik Wiberg (1992). *Byggnadsmeknik - Knäckning.* 205. Studentlitteratur.

Schuler, Timothy A. (2017). *Grandview Heights Aquatic Centre's Timber Cables.* URL: `http://www.architectmagazine.com/technology/detail/grandview-heights-aquatic-centres-timber-cables_o`.

Simiu, Emil (2011). *Design of buildings for wind: A guide for ASCE 7-10 standard users and designers of special structures.* 2nd ed. John Wiley & Sons. Chap. 13,15.

Soulis, Konstantinos X., Nikolaos Ntoulas, Panayiotis A. Nektarios, and George Kargas (2017). "Runoff reduction from extensive green roofs having different substrate depth and plant cover". In: *Ecological Engineering* 102, pp. 80–89. ISSN: 0925-8574. DOI: `http://dx.doi.org/10.1016/j.ecoleng.2017.01.031`. URL: `http://www.sciencedirect.com/science/article/pii/S092585741730040X`.

Stathopoulos, Ted and D Surry (1983). "Scale effects in wind tunnel testing of low buildings". In: *Journal of Wind Engineering and Industrial Aerodynamics* 13.1-3, pp. 313–326.

Strasky, Jiri (2005). *Stress ribbon and cable-supported pedestrian bridges.* 2nd ed. Thomas Telford.

Suzuki, M., S. Sanada, Y. Hayami, and S. Ban (1997). "Prediction of wind-induced response of a semi-rigid hanging roof". In: *Journal of Wind Engineering and Industrial Aerodynamics* 72, pp. 357–366. ISSN: 0167-6105. DOI: `http://dx.doi.org/10.1016/S0167-6105(97)00255-9`. URL: `http://www.sciencedirect.com/science/article/pii/S0167610597002559`.

Svenska Naturtak (2017). Teknisk Broschyr. Optigreen.

Wikipedia (2009). *Tacoma Narrows Bridge (1940).* This image can be used if its used to illustrate the subject in question. URL: `https://en.wikipedia.org/wiki/File:Image-Tacoma_Narrows_Bridge1.gif`.

– (2017). *Saltation (geology).* This material was created by NASA. NASA copyright policy states that material is not protected by copyright unless noted. URL: `https://en.wikipedia.org/wiki/Saltation_(geology)#/media/File:Saltation-mechanics.gif`.

Xu, You-Lin (2013). *Wind effects on cable-supported bridges.* John Wiley & Sons.

Zhou, Xuanyi, Jinhai Hu, and Ming Gu (2014). "Wind tunnel test of snow loads on a stepped flat roof using different granular materials". In: *Natural Hazards* 74.3, pp. 1629–1648. ISSN: 1573-0840. DOI: `10.1007/s11069-014-1296-z`. URL: `http://dx.doi.org/10.1007/s11069-014-1296-z`.

Zhou, Xuanyi, Luyang Kang, Ming Gu, Liwei Qiu, and Jinhai Hu (2016). "Numerical simulation and wind tunnel test for redistribution of snow on a flat roof". In: *Journal of Wind Engineering and Industrial Aerodynamics* 153, pp. 92–105. ISSN: 0167-6105. DOI: `http://dx.doi.org/10.1016/j.jweia.2016.03.008`. URL: `http://www.sciencedirect.com/science/article/pii/S0167610516301465`.